EXPERIMENTAL INVESTIGATION OF A PRINTED CIRCUIT HEAT EXCHANGER USING SUPERCRITICAL CARBON DIOXIDE AND WATER AS HEAT TRANSFER MEDIA

by

JOSH VAN METER

B.S., Kansas State University, 2006

A THESIS

submitted in partial fulfillment of the requirements for the degree

MASTER OF SCIENCE

Department of Mechanical and Nuclear Engineering
College of Engineering

KANSAS STATE UNIVERSITY
Manhattan, Kansas

2008

Approved by:

Major Professor
Dr. Akira T. Tokuhiro

Abstract

The Secure Transportable Autonomous Reactor – Liquid Metal system combines a Generation IV nuclear reactor with an advanced Supercritical Carbon Dioxide (S-CO_2) Brayton power conversion cycle. The Brayton cycle was selected as the power conversion cycle due to its high efficiency, small turbomachinery size, and competitive cost due to reduced complexity as compared to a traditional Rankine cycle. Overall system thermal efficiency is closely tied to the performance of the precooler and recuperators. The Printed Circuit Heat Exchanger (PCHE) manufactured by Heatric is being considered for use as both the precooler and recuperator in the STAR-LM system due to its high effectiveness, wide temperature and pressure operating range, small size, and low cost. PCHEs have been used primarily in the hydrocarbon processing industry to date, and are relatively new in being considered for nuclear applications.

In this study, a PCHE is investigated using S-CO_2 and water as the heat transfer media in conditions relevant to the precooler in the STAR-LM system. Experiments conducted with small temperature differences across the PCHE revealed that the heat transfer coefficient is strongly correlated with the temperature-dependent specific heat near the pseudocritical point. The STAR-LM precooler outlet temperature is near the pseudocritical point, making this region of interest to this work. Testing was conducted to determine the effect of property variation near the precooler outlet in conditions with large temperature differences in the PCHE. These tests revealed that maintaining the precooler outlet temperature near the pseudocritical point does not have a significant effect on heat transfer coefficients in the PCHE under large temperature difference test conditions.

Computational Fluid Dynamics (CFD) models were developed to simulate fluid flow and heat transfer in the PCHE. A 2D, 4-channel, zig-zag model was found to reproduce the outlet temperatures to within approximately 15% relative error. The 3D straight channel model reproduced the experimental data to within 3% relative error for the cases simulated. Both of these models predicted the water side outlet temperatures to within 20% relative error.

Table of Contents

Table of Contents iii
List of Figures v
List of Tables ix
Acknowledgements xi
CHAPTER 1 – Introduction 1
1.1 Research Background 1
1.2 Literature Review 10
1.2.1 Printed Circuit Heat Exchanger 10
1.2.2 Influence of Channel Shape on Heat Transfer and Fluid Flow 11
1.2.3 Supercritical Fluids 15
1.3 Objectives 18
CHAPTER 2 - Experimental Setup 20
2.1 Printed Circuit Heat Exchanger (PCHE) 21
3.2 Power Supply 24
2.3 Cooling System 25
2.4 Pressurizer 27
2.5 Pump 28
2.6 Instrumentation 31
CHAPTER 3 – PCHE Internal Configuration Estimation 34
3.1 Channel Configuration 34
3.2 Plate Configuration 43
CHAPTER 4 – Experimental Results 47
4.1 Supercritical Heat Transfer 47
4.2 Data Analysis Method 50
4.3 Small Temperature Difference Testing 51
4.4 Large Temperature Difference Testing Based on STAR-LM Precooler Conditions 54

CHAPTER 5 – FLUENT Simulations 66
5.1 FLUENT Theoretical Background 66
5.1.1 Conservation of Mass 66
5.1.2 Conservation of Momentum 67
5.1.3 Energy Equation – Fluid Region 67
5.1.4 Energy Equation – Solid Region 68
5.1.5 Renormalization-Group (RNG) k-ε Turbulence Model 69
5.2 2-Dimensional PCHE Model 72
5.3 3-Dimensional PCHE Model 77
CHAPTER 6 – Conclusions 82
References 86
Appendix A – Experimental Data 92
Appendix B – Error Analysis 96
Appendix C – Experimental Procedure 103
Appendix D - Thermophysical properties of CO_2 107
Appendix E – 2D FLUENT Model Results 132

List of Figures

Figure 1.1: Comparison of Electricity Costs [2] 2
Figure 1.2: CO_2 Emissions from Electrical Production Sources [3] 2
Figure 1.3: Comparison of Turbine Size [5] 3
Figure 1.4: STAR-LM and Power Conversion Cycle [7] 5
Figure 1.5(a): Specific Heat versus Temperature at 7.4 MPa 6
Figure 1.5(b): Density versus Temperature at 7.4 MPa 6
Figure 1.6: Density Variation with STAR-LM Precooler Temperatures 7
Figure 1.7: Precooler Outlet Temperature versus Cycle Efficiency [7] 8
Figure 1.8: Phase Diagram for CO_2 [33] 16
Figure 2.1: Experimental Loop Schematic 20
Figure 2.2: Size Comparison of PCHE and Shell and Tube Heat Exchanger [11] 22
Figure 2.3: PCHE Plates and Diffusion Bond [11] 23
Figure 2.4: PCHE Inlets and Outlets 24
Figure 2.5: Power Supply and Buss Bars 25
Figure 2.6: Tube-in-Tube Heat Exchanger 26
Figure 2.7: GCI Icewagon Chiller 27
Figure 2.8: Pressurizer 28
Figure 2.9: Micropump 5K Pump and Motor 29
Figure 2.10: Micropump 5K Gears 29
Figure 2.11: Rosemount Model 2088 and 3051 Pressure Transducers 31
Figure 2.12: PROmass 80M Flowmeter 32
Figure 2.15: Data Acquisition System and Power Supply Control 33
Figure 3.1: Simplified PCHE Channel Shape [33] 36
Figure 3.2: Hot Side Pressure Drop Data [33] 39
Figure 3.3: Cold Side Pressure Drop Data [33] 40
Figure 3.4: Simplified Channel Geometry 41
Figure 3.5: TiTech Channel Configuration [15] 43

Figure 4.1(a): Specific Heat and Density of CO_2 at 7.5 MPa [47] 48
Figure 4.1(b): Viscosity and Thermal Conductivity of CO_2 at 7.5 MPa [47] 48
Figure 4.2(a): Specific Heat and Density of Water at 22.5 MPa [47] 49
Figure 4.2(b): Viscosity and Thermal Conductivity of Water at 22.5 MPa [47] 49
Figure 4.3: Relation Between Outlet Temperature and Specific Heat to Pseudocritical Values at 8.0 MPa 53
Figure 4.4: Heat Transfer Coefficient and Specific Heat for Small Temperature Difference Testing at 8.0 MPa 53
Figure 4.5: Design Conditions for STAR-LM Reactor System [7] 55
Figure 4.6: Precooler Operating Range [7] 56
Figure 4.7: CO_2 Specific Heat and Testing Temperatures at 8.0 and 9.0 MPa 57
Figure 4.8: Relation Between Temperature and Specific Heat at PCHE Outlet to Pseudocritical Values at 8.0 MPa 58
Figure 4.9: Heat Transfer Coefficient versus Reynolds Number at 8.0 MPa 59
Figure 4.10: Heat Transfer Coefficient versus Reynolds Number at 9.0 MPa 59
Figure 4.11: S-CO_2 Heat Transfer Coefficient at 8.0 MPa 60
Figure 4.12: S-CO_2 Heat Transfer Coefficient at 9.0 MPa 61
Figure 4.13: Comparison of Heat Transfer Coefficients at 8.0 and 9.0 MPa 62
Figure 4.14: Heat Transfer Coefficients at 7.5, 8.0, 8.5, and 9.0 MPa 63
Figure 4.14: Specific Heat versus Temperature 64
Figure 4.15: Density versus Temperature [47] 65
Figure 5.1: 2D PCHE Model Section 73
Figure 5.2: Simulated Temperature Distribution for Test B13 75
Figure 5.3: 3D Model Geometry 78
Figure D.1: Specific heat at 74bar 109
Figure D.2: Density at 74bar 109
Figure D.3: Thermal Conductivity at 74bar 110
Figure D.4: Enthalpy at 74bar 110
Figure D.5: Viscosity at 74bar 111
Figure D.6: Thermal diffusivity at 74bar 111
Figure D.7: Specific heat at 75bar 114

Figure D.8: Density at 75bar 114
Figure D.9: Enthalpy at 75bar 115
Figure D.10: Thermal conductivity at 75bar 115
Figure D.11: Viscosity at 75bar 116
Figure D.12: Thermal diffusivity at 75bar 116
Figure D.13: Specific heat at 80bar 119
Figure D.14: Density at 80bar 119
Figure D.15: Thermal conductivity at 80bar 120
Figure D.16: Viscosity at 80bar 120
Figure D.17: Enthalpy at 80bar 121
Figure D.18: Thermal diffusivity at 80bar 121
Figure D.19: Specific heat at 85bar 124
Figure D.20: Density at 85bar 124
Figure D.21: Thermal conductivity at 85bar 125
Figure D.22: Enthalpy at 85bar 125
Figure D.23: Viscosity at 85bar 126
Figure D.24: Thermal diffusivity at 85bar 126
Figure D.25: Specific heat at 90bar 129
Figure D.26: Density at 90bar 129
Figure D.27: Enthalpy at 90bar 130
Figure D.28: Thermal conductivity at 90bar 130
Figure D.29: Viscosity at 90bar 131
Figure D.30: Thermal diffusivity at 90bar 131
Figure E.1: Temperature Distribution of Test B6 132
Figure E.2: Temperature Distribution of Test B7 132
Figure E.3: Temperature Distribution of Test B8 133
Figure E.4: Temperature Distribution of Test B9 133
Figure E.5: Temperature Distribution for Test B10 134
Figure E.6: Temperature Distribution for Test B11 134
Figure E.7: Temperature Distribution for Test B12 135
Figure E.8: Temperature Distribution for Test B13 135

Figure E.9: Temperature Distribution for Test B14..... 136
Figure E.10: Temperature Distribution for Test B15..... 136
Figure E.11: Temperature Distribution for Test C5..... 137
Figure E.12: Temperature Distribution for Test C6..... 137
Figure E.13: Temperature Distribution for Test C7..... 138
Figure E.14: Temperature Distribution for Test C8..... 138
Figure E.15: Temperature Distribution for Test C9..... 139
Figure E.16: Temperature Distribution for Test C10..... 139
Figure E.17: Temperature Distribution for Test C11..... 140
Figure E.18: Temperature Distribution for Test C12..... 140
Figure E.19: Temperature Distribution for Test C13..... 141
Figure E.20: Temperature Distribution for Test C14..... 141

List of Tables

Table 1.1: Effect of Precooler Outlet Temperature on STAR-LM System [7] 9
Table 1.2: Ishizuka et al. Experimental Conditions [15] 11
Table 1.3: Small Channel Heat Transfer Correlations 13
Table 1.4: Small Channel Friction Factor Correlations 14
Table 1.5: Supercritical Fluid Heat Transfer Correlations – Horizontal Flow 17
Table 2.1: PCHE Specifications from Heatric 24
Table 2.2: PEEK Gear Measurements 30
Table 2.3: Rosemount Pressure Transducer Specifications 32
Table 3.1: PCHE Design Specifications 34
Table 3.2: TiTech PCHE Specifications 35
Table 3.3: Hot Side Pressure Drop Data – Water 39
Table 3.4: Cold Side Pressure Drop Data – Water 39
Table 3.5: Possible Channel Geometries 42
Table 3.6: Possible ANL PCHE Plate Configurations 44
Table 3.7: ANL Plate Configuration Evaluation 46
Table 3.8: Estimated ANL PCHE Dimensions 46
Table 4.1: Small Temperature Difference Experimental Conditions 52
Table 4.2: Testing Parameters for 8.0 and 9.0 MPa 57
Table 5.1: Simulated Experimental Conditions 74
Table 5.2: 2D Model Comparison of Experimental and Simulated Data 76
Table 5.3: 3D Model Comparison of Experimental and Simulated Data 79
Table 5.4: 3D Model Comparison with TiTech Data 80
Table 6.1: Estimated ANL PCHE Dimensions 82
Table A.1: Hot Side Pressure Drop Data – Water [33] 92
Table A.2: Cold Side Pressure Drop Data – Water [33] 92
Table A.3: Experimental Conditions for Small Temperature Difference Testing at 8.0 MPa 93
Table A.4: Experimental Conditions for Test Set B 94

Table A.5: Experimental Conditions for Test Set C 95
Table B.1: Error Analysis Rules 96
Table B.2: Experimental Data for Test C4 98
Table B.3: Enthalpy for the hot side 98
Table B.4 Density and viscosity for CO_2 101
Table D.1: Thermal properties at 74bar 107
Table D.2: Thermophysical properties of CO2 at 75bar 112
Table D.3: Thermophysical properties at 80bar 117
Table D.4: Thermophysical properties at 85bar. 122
Table D.5: Thermophysical properties at 90bar 127

Acknowledgements

I would sincerely like to thank my family and friends for their encouragement and support. I would also like to thank my advisory committee for their time and effort in helping me complete this work. I gratefully acknowledge financial support for this work provided by the Advanced Fuel Cycle Initiative of the Global Nuclear Energy Partnership.

CHAPTER 1 – Introduction

1.1 Research Background

The United Nations Department of Economic and Social Affairs/Population Division predicts that the world population will increase to approximately 9 billion by the year 2050. This increase in world population will be accompanied by an increase in energy consumption. The International Energy Agency projects that the demand for electricity worldwide will double from nearly 3,500 gigawatts electric (GWe) in 2000 to 7,157 GWe in 2030. The World Nuclear Association predicts that between 524 and 740 GWe will be generated through nuclear power in 2030, as compared to 367 GWe in 2005 [1]. This will require 200 to 400 new nuclear plants to be constructed and operational by 2030. Many countries are considering nuclear power as an economic and environmentally acceptable means for meeting some of the growing demand for electricity. Figure 1.1 shows a comparison of average electricity production costs in the U.S. from nuclear, coal, gas, and petroleum sources [2]. It can be seen from Figure 1.1 that nuclear power is the most cost effective source of energy based on operational and maintenance costs. For the year 2007, the cost of producing one kilowatt-hour (kWh) using petroleum was over five times greater than the cost of producing the same amount of energy using nuclear power.

Nuclear energy is attractive from an environmental standpoint because of lower life cycle emissions as compared to other electricity generation methods. Figure 1.2 shows the CO_2 emissions of major power sources per kWh. It can be seen from Figure 1.2 that nuclear power has the lowest life cycle CO_2 emissions of any of the major power generation methods, including hydroelectric and wind power.

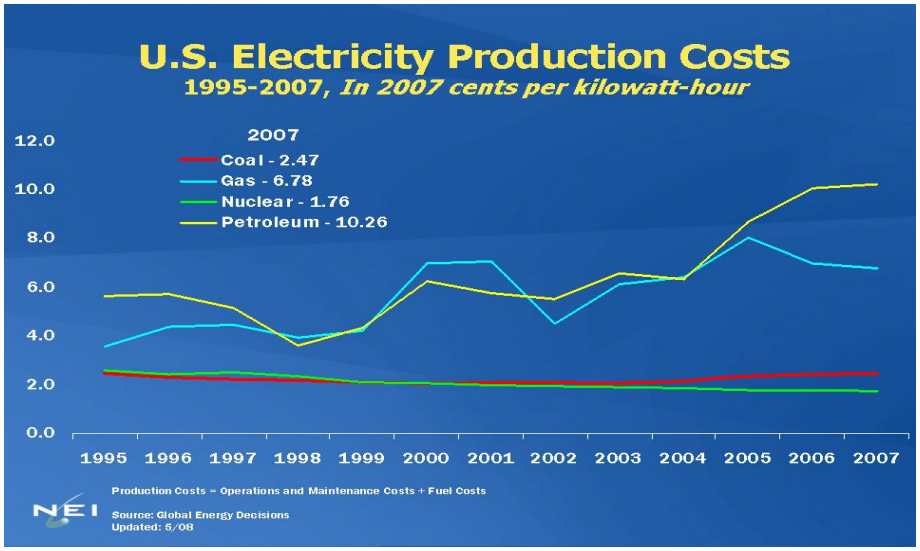

Figure 1.1: Comparison of Electricity Costs [2]

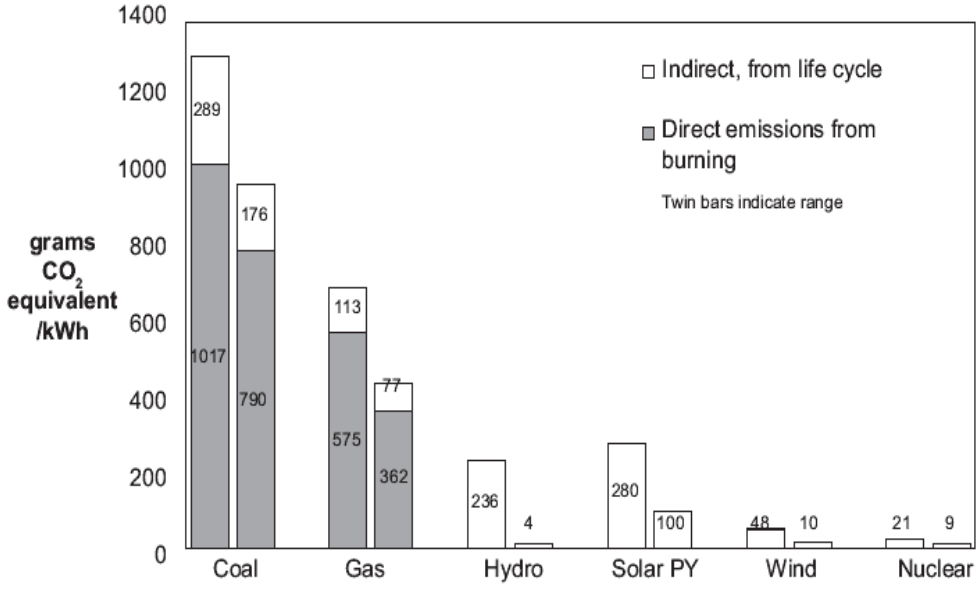

Figure 1.2: CO_2 Emissions from Electrical Production Sources [3]

Nuclear power is desirable from both an economic and environmental viewpoint once in operation. However, there are considerable capital costs required before a plant can begin producing electricity. The Secure Transportable Autonomous Reactor (STAR) was designed by Argonne National Laboratory (ANL) to meet economic goals by taking

advantage of modular construction, up-to-date manufacturing processes, design simplifications, and advanced technologies as compared to Generation II and III reactors currently in use worldwide. The STAR system allows for significant reductions in plant costs, size, and complexity, combined with a significant increase in plant efficiency through the use of an advanced Brayton power conversion cycle using supercritical carbon dioxide (S-CO_2) as the working fluid.

As compared to a Rankine power conversion cycle, the turbomachinery required by the S-CO_2 Brayton power conversion cycle is more compact [4], is less expensive, and has shorter construction periods. These effects reduce the capital cost of a new reactor. The S-CO_2 turbomachinery reduces the power plant cost by about 18% as compared to a traditional Rankine steam cycle [5]. A comparison of turbine sizes for steam, helium, and S-CO_2 is shown in Figure 1.3. It can be seen from Figure 1.3 that the S-CO_2 turbines (and compressors) are very compact, thus requiring a smaller plant footprint.

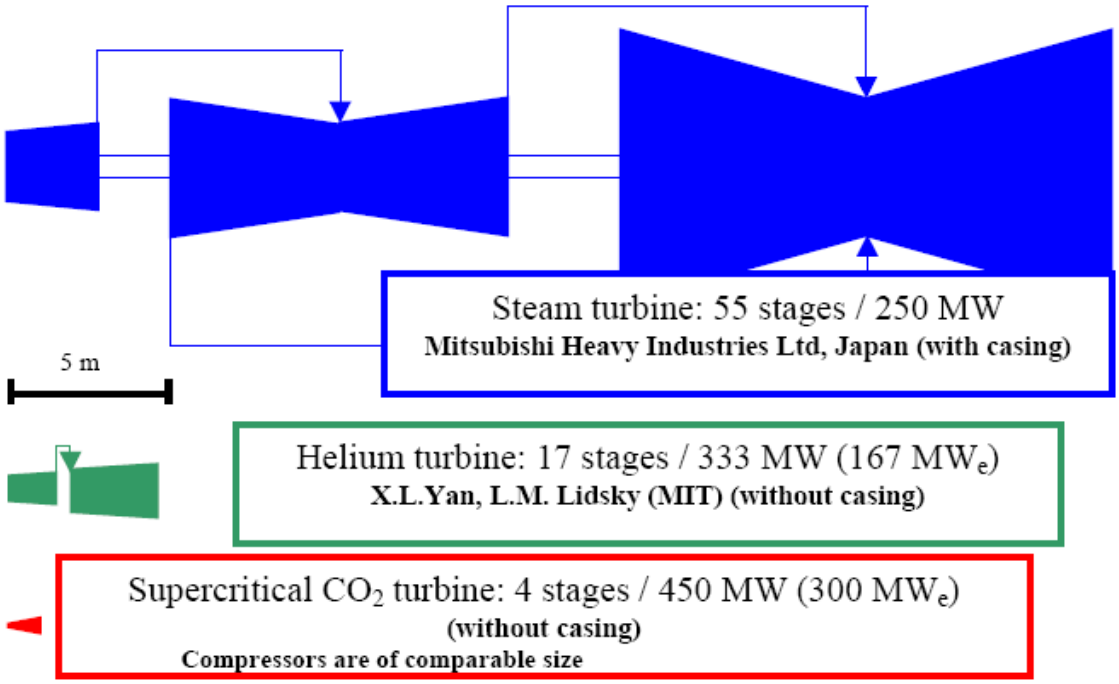

Figure 1.3: Comparison of Turbine Size [5]

The STAR reactor plant operating with a turbine inlet temperature of 550 ºC is anticipated to have a maximum overall plant efficiency of nearly 45%. This offers a significant improvement over using the same reactor with a Rankine steam cycle, which has a maximum efficiency of about 39%, while also eliminating costly Rankine cycle components [6]. It has been shown that each 1% increase in cycle efficiency translates to a savings of approximately $800,000 per year, or $31.5 million over the plant lifetime (40 years) [7].

The STAR-LM (Liquid Metal) reactor is also attractive for reasons of safety, proliferation resistance, sustainability, and the ability to operate for 15-20 years without refueling [7]. The STAR-LM is a 400 megawatt thermal (MWt), high-temperature fast reactor using natural circulation liquid lead, or lead-bismuth eutectic, as the primary coolant. The STAR-LM system is designed to be a nearly autonomous, load-following reactor. Active reactor control rods are not necessary because strong reactivity feedback of the fast neutron spectrum with lead coolant match heat removal from the Balance of Plant (BOP), regulating reactor power without operator intervention. The lack of required control rods, as well as the high boiling temperature of liquid lead (T_{boil} = 1740 ºC), eliminate entire classes of accidents that are possible in other liquid metal cooled reactors. The STAR-LM plant design is robust, with plant dynamics codes confirming passive safety of the core in all unprotected (unscrammed) events [8].

Figure 1.4 shows envisioned STAR-LM reactor temperatures and pressures, along with temperatures and pressures for the S-CO_2 Brayton cycle power conversion cycle. As can be seen from Figure 1.4, the power conversion cycle consists of a turbine, high and low temperature recuperators (HTR and LTR, respectively), a precooler, and two compressors. In Figure 1.4, the operating temperatures and pressures determined by Moissytsev are shown for each component in the power conversion cycle. Also shown are the average and peak temperatures for the fuel, cladding, and coolant in the reactor core. For the core temperatures shown in Figure 1.4, Tcl is the fuel centerline temperature, Tfo is the outside fuel temperature, Tci is the interior cladding temperature, Tco is the outside cladding temperature, and Tc is the coolant temperature.

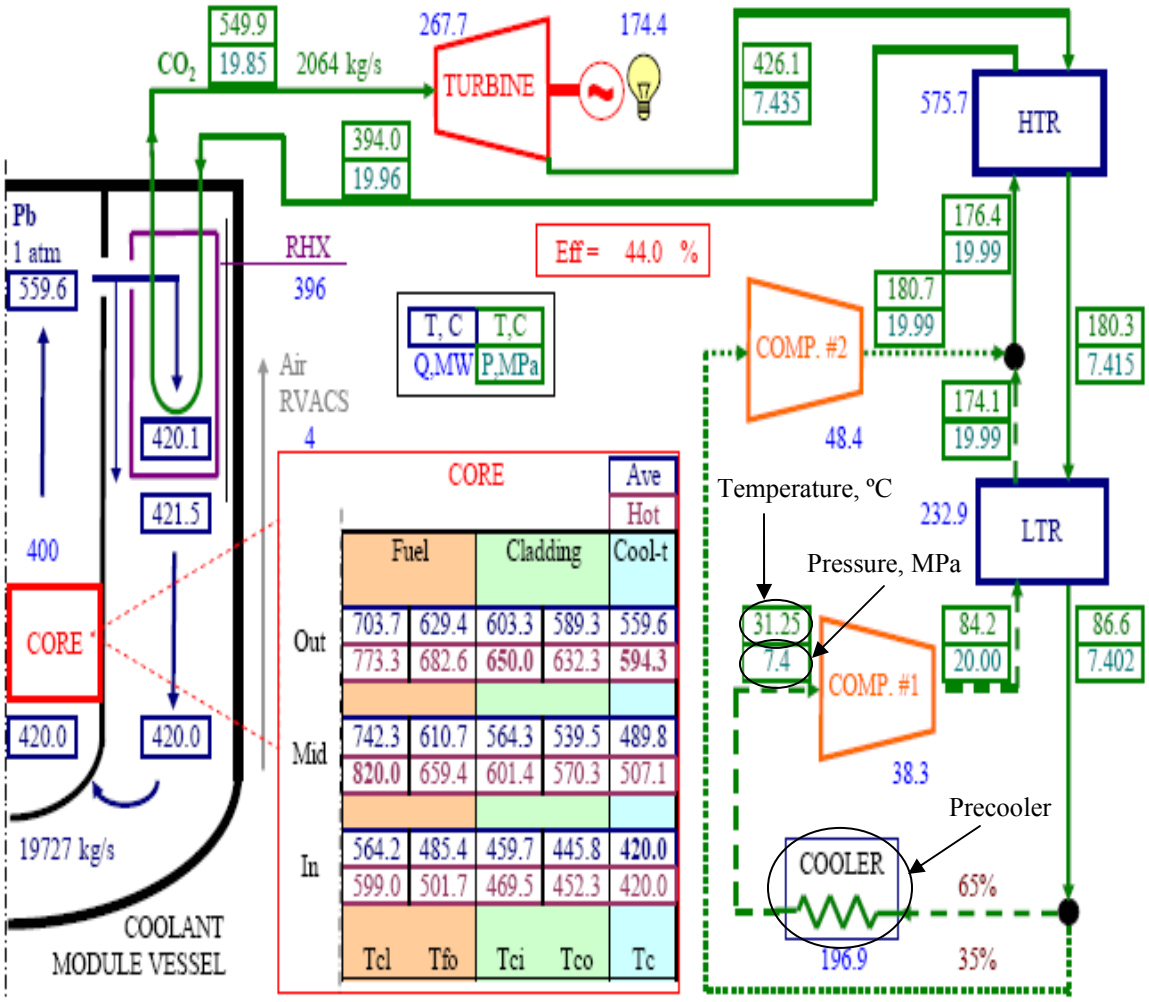

Figure 1.4: STAR-LM and Power Conversion Cycle [7]

Supercritical fluids, such as CO_2, exhibit unique characteristics near the pseudocritical point, where the specific heat of the fluid reaches a maximum for a given pressure. Figures 1.5(a) and (b) show the temperature dependent specific heat and density variation, along with the pseudocritical temperature of CO_2 as well as the precooler outlet temperature at a pressure of 7.4 MPa.

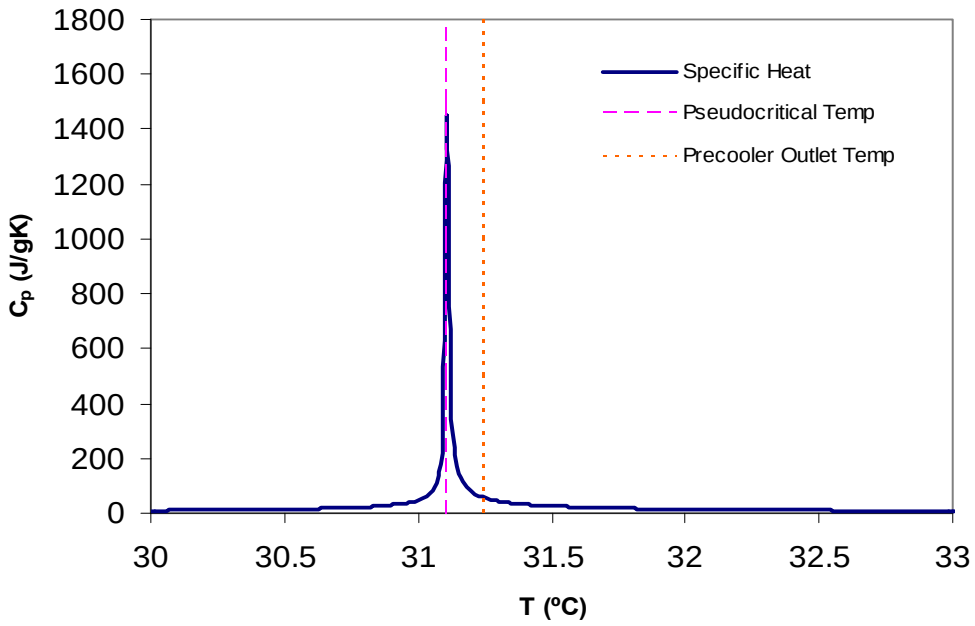

Figure 1.5(a): Specific Heat versus Temperature at 7.4 MPa

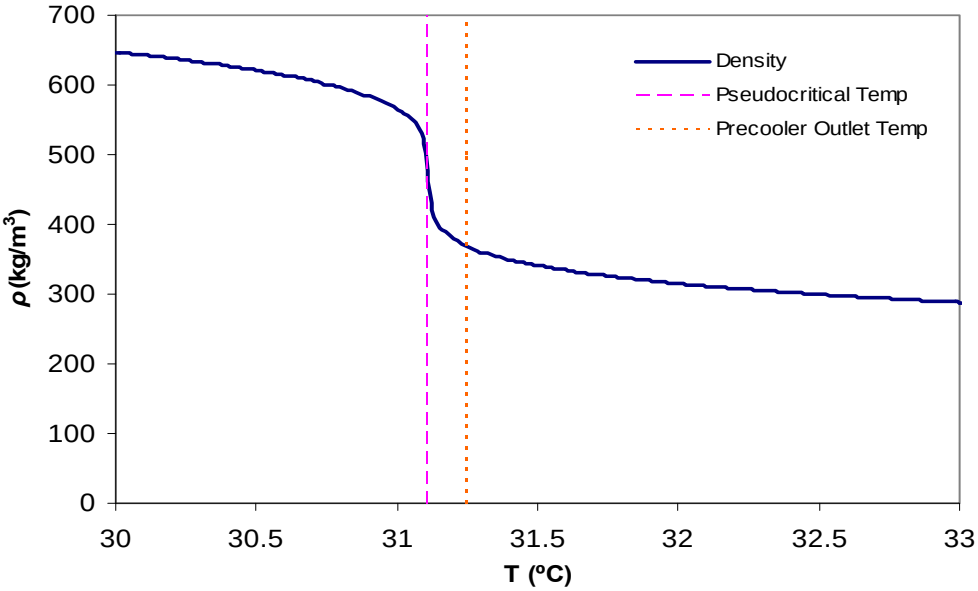

Figure 1.5(b): Density versus Temperature at 7.4 MPa

As can be seen from Figures 1.5(a) and (b), the specific heat and density of CO_2 change rapidly near the pseudocritical point. The STAR-LM system is designed to take

advantage of this thermophysical variation by placing the precooler outlet temperature near the pseudocritical point at a pressure of 7.4 MPa. The dramatic increase in density near the pseudocritical point leads to greatly reduced compression work, increasing overall plant efficiency. Figure 1.6 shows the variation of CO_2 density versus temperature over the envisioned precooler operating range at a pressure of 7.4 MPa. Figure 1.6 also identifies the precooler inlet and outlet temperatures.

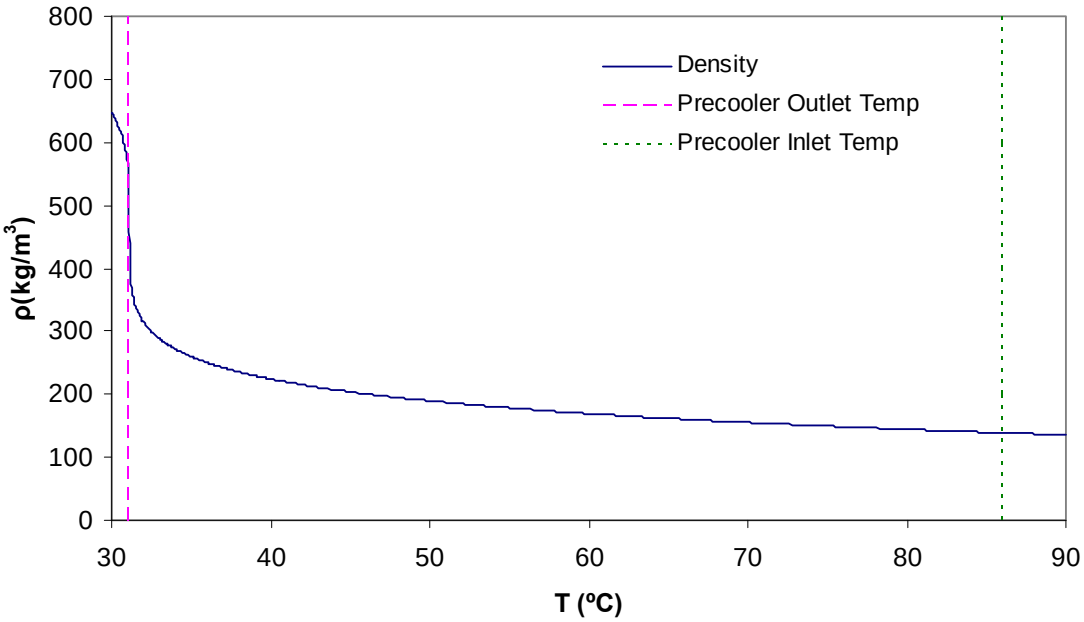

Figure 1.6: Density Variation with STAR-LM Precooler Temperatures

The overall cycle efficiency is closely related to the minimum temperature of the cycle (precooler outlet temperature). The variation of overall cycle efficiency with precooler outlet temperature is shown in Figure 1.7.

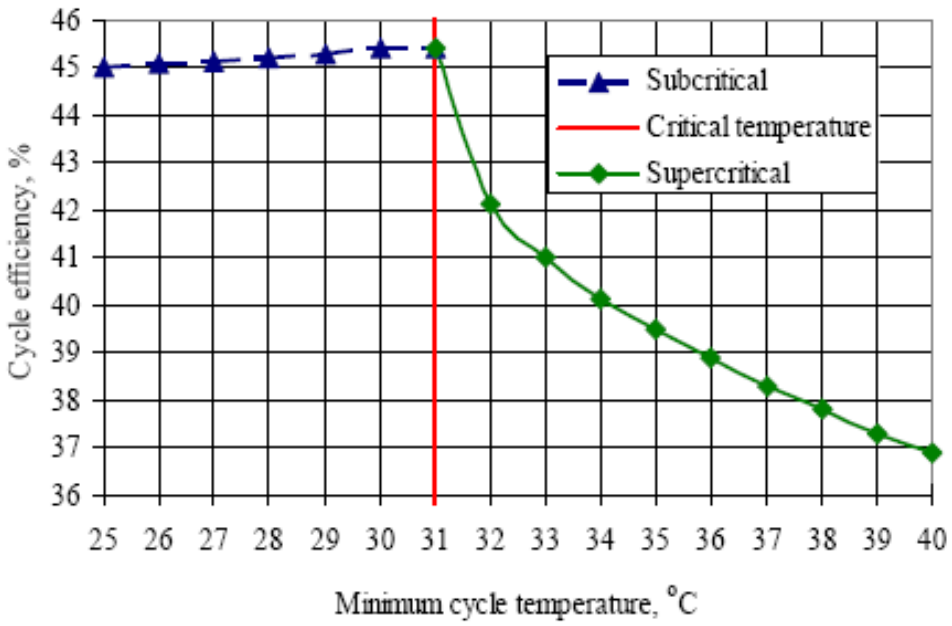

Figure 1.7: Precooler Outlet Temperature versus Cycle Efficiency [7]

As can be seen from Figure 1.7, the cycle efficiency increases, reaches a peak at the critical temperature, then decreases with further increases in temperature. From this optimization, the precooler outlet temperature should be 31.0 ºC to achieve the highest possible cycle efficiency. However, there are two reasons to set the precooler outlet temperature at a slightly higher value of 31.25 ºC. The first reason is compressor durability. An outlet temperature of 31.0 ºC is very close to the critical temperature of 30.98 ºC. It is too close to maintain the CO_2 in a supercritical state at all times with any active control scheme. With this proximity, a small temperature disturbance could drop the temperature below the critical temperature and cause two-phase flow inside the compressor, dramatically shortening compressor lifetime. The 31.25 ºC outlet temperature provides a safety margin to ensure the CO_2 stays in a supercritical state as a large amount of heat must be removed to decrease the CO_2 temperature by a small amount due to the peak in specific heat seen in Figure 1.5(a). The CO_2 pressure in the precooler is also increased slightly above the critical pressure of 7.377 MPa, to a pressure of 7.4 MPa, to provide a safety margin so that pressure fluctuations do not drop the system below the critical pressure. The temperature and pressure margins above the

critical point were determined by Moisseytsev [7] to provide a sufficient safety margin to avoid two-phase flow inside the compressor for the STAR-LM operating conditions.

The second reason for using an outlet temperature of 31.25 ºC is the required precooler size. Since a large amount of heat must be removed from the CO_2 to decrease its temperature near the critical point, a precooler length of 12.1 m is estimated for an outlet temperature of 31.25 ºC compared to a precooler length of 26.5 m with an outlet temperature of 31.0 ºC. Thus, the increase in outlet temperature results in a smaller precooler, although it increases the compressive work required between the precooler outlet and LTR inlet. Table 1.1 summarizes the heat exchanger length, required compressive work, and overall cycle efficiency for precooler outlet temperatures of 31.0 ºC and 31.25 ºC.

Table 1.1: Effect of Precooler Outlet Temperature on STAR-LM System [7]

Precooler outlet temp.	31.00°C	31.25°C
Heat exchanger length	26.5m	12.1m
Compressor #1 work	27.6MW	40.0MW
Cycle efficiency	45.8%	43.8%

This study is a continuation of the work conducted by M.S. student Hoseok Song [33]. It focuses on the precooler in the STAR-LM system where heat is exchanged between S-CO_2 and water as is seen in Figure 1.4. Experiments are conducted to examine the effect of varied temperatures and pressures on heat transfer inside the precooler, using the temperatures and pressures shown in Figure 1.4 as a baseline.

1.2 Literature Review

1.2.1 Printed Circuit Heat Exchanger

In order for the STAR-LM system to achieve high overall efficiencies while maintaining a small plant footprint, highly efficient and compact heat exchangers are required. The compact size is especially important for the Reactor Heat Exchanger (RHX), shown in Figure 1.4, as this heat exchanger is placed inside the primary reactor vessel containment. These heat exchangers must also be able to withstand high temperatures and large differential pressures. The Printed Circuit Heat Exchanger (PCHE) manufactured by Heatric is being considered for use as the RHX, HTR, LTR, and Cooler seen in Figure 1.4.

The PCHE core is made up of plates with chemically etched flow paths. These plates are stacked and diffusion bonded into a monolithic body, achieving parent metal strength [9]. Pressure differences of 20 MPa are considered routine, with values in the range of 30 to 40 MPa possible. These heat exchangers can also reach effectiveness values of 98% or greater, with the PCHE core being 5-10 times smaller than tube bundles of similar performance [10]. Possible working temperatures for these heat exchangers range from cryogenic to 900 ºC [11].

Heatric heat exchangers have been selected for use in the STAR-LM reactor [12], the Gas Cooled Fast Reactor [13], and the Sodium Cooled Fast Reactor / Advanced Burner Reactor [14]. However, basic heat transfer and pressure drop data under reactor-relevant conditions are lacking in the open literature.

The only available publication examining fluid flow and heat transfer of CO_2 in a Heatric PCHE is by Ishizuka et al. [15]. Their experiments used a PCHE rated at 3 kW with CO_2 on both the hot and cold sides of the heat exchanger. Experimental conditions for the Ishizuka et al. tests are shown in Table 1.2.

Table 1.2: Ishizuka et al. Experimental Conditions [15]

	Hot Side	Cold Side	Units
Pressure	2.2 – 3.5	6.5 – 10.7	MPa
Inlet Temperature	150 – 280	60 – 120	ºC
Flow Rate	35 – 90	35 – 90	kg / hr

While CO_2 on the cold side was in a supercritical state for many of the tests, the hot side pressure was well below the critical pressure (7.377 MPa) for all cases. Further, all tests with S-CO_2 on the cold side were carried out far from the pseudocritical region, where the fluid properties change dramatically with small temperature changes. The effectiveness of the heat exchanger was in the range of 98% to 99% for all test conditions. Pressure loss and heat transfer coefficients were empirically found to vary linearly with Reynolds number. No significant differences were noted between subcritical and supercritical conditions.

Heatric PCHEs use small semi-circular flow channels, ranging from 0.5 to 5.0 mm in depth. These small channels have the benefit of creating a large heat transfer area for a given heat exchanger volume. However, fluid flow and heat transfer characteristics inside small channels often depart from those of conventional sized-channels [16, 17, 18]. The PCHE channels are shaped into a herringbone, or zig-zag, pattern. Higher tortuosity from the zig-zag pattern has been shown to enhance heat transfer coefficients considerably [19], though validated correlations for prediction of heat transfer performance of wavy channels are not available [5]. Also, the use of a supercritical fluid as a heat transfer medium introduces difficulties in analysis due to steep property variations near the pseudocritical point [20]. These effects combine to make analytical evaluation of a PCHE using S-CO_2 as the working fluid difficult.

1.2.2 Influence of Channel Shape on Heat Transfer and Fluid Flow

It has been noted by many researchers that the heat transfer and fluid flow characteristics of small channels are significantly different than those of conventional

sized channels. This is a relatively new research area in that active research into the thermal hydraulic performance of fluids in microchannels began around 1998 [21]. The definition of "conventional" sized channels is still somewhat arbitrary, with researchers defining the lower limit as 2 cm [22, 23], 6 mm [24], or 3 mm [21]. However, there is no reliable experimental evidence to support the smallest channel size for which traditional Nusselt number correlations can be applied without significant error [23].

Two of the most commonly used traditional correlations for heat transfer in channels are the Gnielinski correlation and the Dittus-Boelter correlation. The Gnielinski correlation [25], using the Filenko friction factor correlation, is valid for Re > 2300 and is given by:

$$Nu_G = \frac{\left(\frac{f}{8}\right)(\mathrm{Re}-1000)\mathrm{Pr}}{1+12.7\left(\frac{f}{8}\right)^{1/2}\left(\mathrm{Pr}^{2/3}-1\right)}, \tag{1.1}$$

where Pr is the Prandtl number and f is the friction factor given by

$$f = \left[1.82\log(\mathrm{Re})-1.64\right]^{-2}. \tag{1.2}$$

The Dittus-Boelter correlation, valid for 10,000 < Re < 120,000 and 0.7 < Pr < 120, is given by

$$Nu_{DB} = 0.023\,\mathrm{Re}^{4/5}\,\mathrm{Pr}^{1/3}. \tag{1.3}$$

Table 1.3 shows various heat transfer correlations that were developed for fluid flow in microchannels, along with their valid ranges and errors from measured values, where presented. Many of these are variations of the Gnielinski and Dittus-Boelter correlations shown in Equations 1.1 and 1.3, respectively. Due to the complicated nature of fluid flow, especially turbulent flow, in microchannels, there is not a good theoretical heat transfer correlation or a theoretically valid method for applying bounds to empirically developed correlations. Thus, the correlations presented tend to use the range of experimentation used to develop individual correlations as bounding conditions. Caution should be used in applying these correlations beyond the stated bounds.

Table 1.3: Small Channel Heat Transfer Correlations

Author	Channel Shape	Correlation	Valid Ranges	Error	Eqn
Adams et al. [23]	Circular	$Nu = Nu_G(1+F)$ $F = 7.6*10^{-5}\,\mathrm{Re}\left[1-\left(\frac{D}{1.164mm}\right)^2\right]$	$2600 \le \mathrm{Re} \le 23{,}000$ $1.53 \le \mathrm{Pr} \le 6.43$ $0.102 \le D \le 1.09mm$	±18.6%	1.4
Choi et al. [18]	Circular	$Nu = 0.000972\,\mathrm{Re}^{1.17}\,\mathrm{Pr}^{1/3}$ $Nu = 3.82*10^{-6}\,\mathrm{Re}^{1.96}\,\mathrm{Pr}^{1/3}$	Laminar Flow Turbulent Flow	±30% ±25%	1.5
Peng et al. [26]	Rectangular	$Nu = C_{H,l}\,\mathrm{Re}^{0.62}\,\mathrm{Pr}^{1/3}$ $Nu = C_{H,t}\,\mathrm{Re}^{4/5}\,\mathrm{Pr}^{1/3}$	Laminar Flow Turbulent Flow	±20% ±25%	1.6[1]
Peng and Peterson [27]	Rectangular	$Nu = 0.1165\left(\frac{D_h}{W_c}\right)^{0.81}\left(\frac{H}{W}\right)^{-0.79}\mathrm{Re}^{0.62}\,\mathrm{Pr}^{1/3}$ $Nu = 0.0.72\left(\frac{D_h}{W_c}\right)^{1.15}\left[1-2.421(Z-0.5)^2\right]\mathrm{Re}^{4/5}\,\mathrm{Pr}^{1/3}$	Laminar Flow Turbulent Flow	±30% ±25%	1.7[2]
Wu and Little [16]	Rectangular	$Nu = 0.00222\,\mathrm{Re}^{1.09}\,\mathrm{Pr}^{0.4}$	Re > 3000		1.8
Wang and Peng [28]	Rectangular	$Nu = 0.00805\,\mathrm{Re}^{4/5}\,\mathrm{Pr}^{1/3}$	Turbulent Flow		1.9

[1] $C_{H,l}$ and $C_{H,t}$ are channel geometry dependent empirical coefficients for laminar and turbulent flow, respectively.

[2] D_h is the channel hydraulic diameter, W_c is the channel center-to-center distance, H is the channel height, W is the channel width, and $Z = \frac{\min(H,W)}{\max(H,W)}$

Researchers have also noted that friction factor behavior in small channels differs from that of conventional channels. For conventional channels in turbulent flow ($4000 \le \mathrm{Re} \le 10^5$), a simple relation is the Blasius equation, given by:

$$f = \frac{0.316}{\mathrm{Re}^{0.25}} \ . \tag{1.10}$$

For laminar flow in conventional channels, the friction factor is given by:

$$f = \frac{C_f}{\mathrm{Re}}, \tag{1.11}$$

where the constant C_f is 64 for circular tubes and is a function of the height to width ratio $\left(\frac{H}{W}\right)$ for rectangular channels. Table 1.4 shows various friction factor correlations for small channels along with their valid ranges.

Table 1.4: Small Channel Friction Factor Correlations

Author	Fluid	Correlation	Valid Ranges	Eqn.
Peng et al. [29]	Water	$f = \frac{C_{f,l}}{\mathrm{Re}^{1.98}}$	Laminar	1.12
		$f = \frac{C_{f,t}}{\mathrm{Re}^{1.72}}$	Turbulent	1.13
Choi et al. [18]	N_2 Gas	$f = \frac{0.140}{\mathrm{Re}^{0.182}}$	$4000 \le \mathrm{Re} \le 18{,}000$	1.14
Wu and Little [16]	N_2, H_2, Air	$f = \frac{110}{8}$	$\mathrm{Re} \le 900$	.1.15
		$f = 0.165(3.48 - \log \mathrm{Re})^{2.4} + 0.081$	$900 < \mathrm{Re} < 3000$	1.16
		$f = \frac{0.195}{\mathrm{Re}^{0.11}}$	$3000 < \mathrm{Re} < 15{,}000$	1.17

Small channels also exhibit different laminar to turbulent behavior than is encountered in larger channels. Transition away from fully laminar flow has been noted at Reynolds numbers as low as 200-400 for straight rectangular channels, with fully turbulent flow at Reynolds numbers of 400-1500 depending on channel dimensions [26,

27]. This is significantly lower than the traditional transition Reynolds number of 2300 for large tubes.

Published literature detailing heat transfer and fluid flow characteristics in wavy and zig-zag configurations, as is encountered in the Heatric PCHE channels, is limited. Experimental results indicate that transition away from laminar flow in non-straight channels occurs at Reynolds numbers as low as 100-150 [30]. Heat transfer enhancements have been observed in corrugated ducts. One study noted a heat transfer enhancement of 2.5 times that associated with parallel-plate channels [31]. Some correlations for heat transfer in corrugated ducts have been proposed. However, these are highly dependent on the experimental geometry used to generate the correlation, and should not be used for different geometries without more extensive experimentation [31].

1.2.3 Supercritical Fluids

The critical point of a fluid is defined as the point at which a distinction between liquid and gaseous phases disappears [32]. Beyond the critical point, thermophysical properties of the fluid vary continuously with temperature, as can be seen in Figure 1.5. Figure 1.8 shows the phase diagram for CO_2 [33]. While a supercritical fluid cannot correctly be defined as either a liquid or a gas, at points above the pseudocritical line the fluid behaves more like a liquid and at points below the pseudocritical line the fluid behavior more closely resembles a gas.

The thermophysical properties of supercritical fluids change rapidly near the pseudocritical point. This introduces difficulty in predicting heat transfer and fluid flow performance. To this end, many experiments have been conducted to develop correlations for predicting fluid behavior. A majority of these experiments were conducted with supercritical fluids flowing vertically upward or downward. It was found that free convection has a noticeable effect in vertical flow, enhancing or deteriorating the heat transfer of a system. These effects have been noted in flows with Reynolds numbers as high as 10^5 [34]. Heat transfer enhancement has been observed when $T_w < T_{pc} < T_b$, where the subscripts w, pc, and b stand for wall, pseudocritical, and bulk. This leads to the formation of a thin liquid-like layer near the wall, with higher thermal conductivity

than the bulk fluid. This enhances heat transfer. A similar analogy applies for deteriorated heat transfer when $T_b < T_{pc} < T_w$ [35]. Equations have been developed to attempt to determine the conditions under which free convection will have a significant effect on heat transfer. However, no one correlation can accurately predict the onset or magnitude of heat transfer deterioration [36].

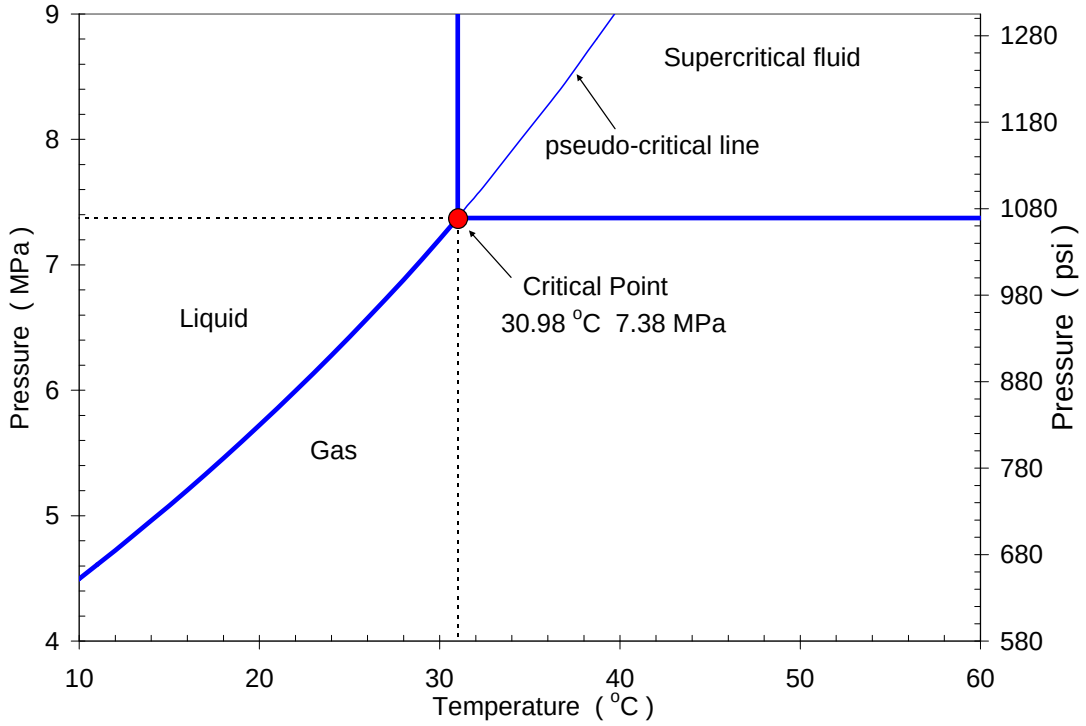

Figure 1.8: Phase Diagram for CO_2 [33]

Heat transfer correlations for horizontal flow of supercritical fluids are presented in Table 1.5. Correlations for vertical flows can be found in a literature review by Pioro et al. [36]. Many of these correlations are modifications to the Gnielinski and Dittus-Boelter correlations, shown in Equations 1.1 and 1.3, using ratios of bulk to wall fluid properties to account for the temperature dependence of supercritical fluids. In the correlations shown in Table 1.5, μ is the fluid viscosity, k is the fluid thermal conductivity, c_p is the fluid specific heat, and *Gr* is the Grashof number. The subscripts *w* and *b* represent properties evaluated at the wall and bulk temperature, respectively.

Table 1.5: Supercritical Fluid Heat Transfer Correlations – Horizontal Flow

Author	Fluid	Correlation	Valid Ranges	Error	Eqn
Bringer and Smith [37]	Water, CO_2	$Nu_x = C\,\mathrm{Re}_x^{0.77}\,\mathrm{Pr}_w^{0.55}$ $C = 0.0266$ for water $C = 0.0375$ for CO_2	$22.6 < P < 34.5 MPa$		1.18
Krasnoschekov and Protopopov [38]	Water, CO_2	$Nu = Nu_G \left(\frac{\mu_b}{\mu_w}\right)^{0.11} \left(\frac{k_b}{k_w}\right)^{-0.33} \left(\frac{\overline{c_p}}{c_{pb}}\right)^{0.35}$ Pr and c_p averaged over temperature range	$20{,}000 < \mathrm{Re}_b < 860{,}000$ $0.85 < \overline{\mathrm{Pr}_b} < 65$	±15%	1.19[3]
Krasnoschekov et al. [39]	Water, CO_2	$Nu = Nu_G \left(\frac{\rho_w}{\rho_b}\right)^{0.3} \left(\frac{\overline{c_p}}{c_{pb}}\right)^{n}$	$80{,}000 < \mathrm{Re}_b < 500{,}000$ $0.85 < \overline{\mathrm{Pr}} < 65$	± 20%	1.20[3]
Jackson [40]	Water, CO_2	$Nu = 0.0183\,\mathrm{Re}_b^{0.82}\,\mathrm{Pr}_b^{0.5} \left(\frac{\rho_w}{\rho_b}\right)^{0.3} \left(\frac{\overline{c_p}}{c_{pb}}\right)^{n}$		± 25%	1.21[3]
Liao and Zhao [41]	CO_2	$Nu_w = 0.128\,\mathrm{Re}_w^{0.8}\,\mathrm{Pr}_w^{0.3} \left(\frac{Gr}{\mathrm{Re}_b^2}\right)^{0.203} \left(\frac{\rho_b}{\rho_w}\right)^{0.437} \left(\frac{\overline{c_p}}{c_{pw}}\right)^{0.384}$	$7.4 < P < 12.0 MPa$ $0.5 \le d \le 2.16 mm$ $20 \le T_b \le 110^\circ C$	±18.9%	1.22[3]
Liao and Zhao [42]	CO_2	$Nu_b = 0.124\,\mathrm{Re}_b^{0.8}\,\mathrm{Pr}_b^{0.3} \left(\frac{Gr}{\mathrm{Re}_b^2}\right)^{0.203} \left(\frac{\rho_w}{\rho_b}\right)^{0.842} \left(\frac{\overline{c_p}}{c_{pb}}\right)^{0.384}$	$7.4 < P < 12.0 MPa$ $0.7 \le d \le 2.16 mm$ $20 \le T_b \le 110^\circ C$	± 21.8%	1.23[3]
Huai et al. [43]	CO_2	$Nu = 0.022186\,\mathrm{Re}^{0.8}\,\mathrm{Pr}^{0.3} \left(\frac{\rho_b}{\rho_w}\right)^{-1.4652} \left(\frac{\overline{c_p}}{c_{pw}}\right)^{0.0832}$	$7.4 < P < 8.5 MPa$ $22 \le T_b \le 53^\circ C$	± 30%	1.24[3]

[3] $\overline{c_p}$ is the mean specific heat, defined as $\overline{c_p} = (i_b - i_w)/(T_b - T_w)$, where i is the fluid enthalpy.

Caution should be used when applying supercritical heat transfer correlations to new experimental configurations, as heat transfer behavior is dependent on physical configuration as well as fluid temperatures and pressures. One example of this is Equation 1.23 developed by Liao and Zhao [42] for S-CO_2 flow in a single, horizontal, circular channel. Huai et al. [43] examined S-CO_2 heat transfer in a test section with 10 parallel circular channels in horizontal flow. Their experimental conditions were within the stated ranges of validity for Equation 1.23, but they noted that their experimental results differed significantly from Equation 1.23. While a majority of their data fell within +60%, -20% of Equation 1.23, some of their data points showed heat transfer over 100% greater than predicted. This prompted development of a new correlation (Equation 1.24) for their specific geometry and flow conditions.

1.3 Objectives

This work reports on the heat transfer performance of a Printed Circuit Heat Exchanger (PCHE) as a key component in the power conversion system of the Secure Transportable Autonomous Reactor – Liquid Metal (STAR-LM). The STAR-LM is a Generation IV nuclear reactor developed at Argonne National Laboratory (ANL). The PCHE is being considered for use as the precooler as well as the high and low temperature recuperators in the STAR-LM system.

The PCHE was designed and manufactured by Heatric and was performance tested at ANL using water and Supercritical Carbon Dioxide (S-CO_2) as the working fluids. The overall objective of this research was to characterize the heat transfer performance of a PCHE in conditions relevant to the STAR-LM precooler. The following approach was employed, based on the scope-of-work agreed upon with support from the United States Department of Energy.

First, the internal configuration of the PCHE was estimated. These estimates were based on the limited specifications supplied by Heatric as well as data reported by the Tokyo Institute of Technology (TiTech).

Second, the heat transfer characteristics of the PCHE with S-CO_2 and water under STAR-LM precooler relevant conditions were examined experimentally. Operational experience with S-CO_2 in near pseudocritical conditions was also gained.

Third, Computational Fluid Dynamics models were developed to simulate fluid flow and heat transfer in the PCHE. These simulation results were then compared to experimental data to determine the accuracy of the CFD models.

CHAPTER 2 - Experimental Setup

An experimental apparatus was constructed at Argonne National Laboratory (ANL) to examine heat transfer and fluid flow characteristics through the Printed Circuit Heat Exchanger (PCHE) manufactured by Heatric. Hot Supercritical Carbon Dioxide (S-CO_2) flowed in a closed loop on one side of the heat exchanger with building water in an open loop on the other side. The two fluids were in a counter-flow arrangement through the bulk of the heat exchanger, with cross-flow sections at the water inlet and outlet. A schematic of the experimental setup is shown in Figure 2.1.

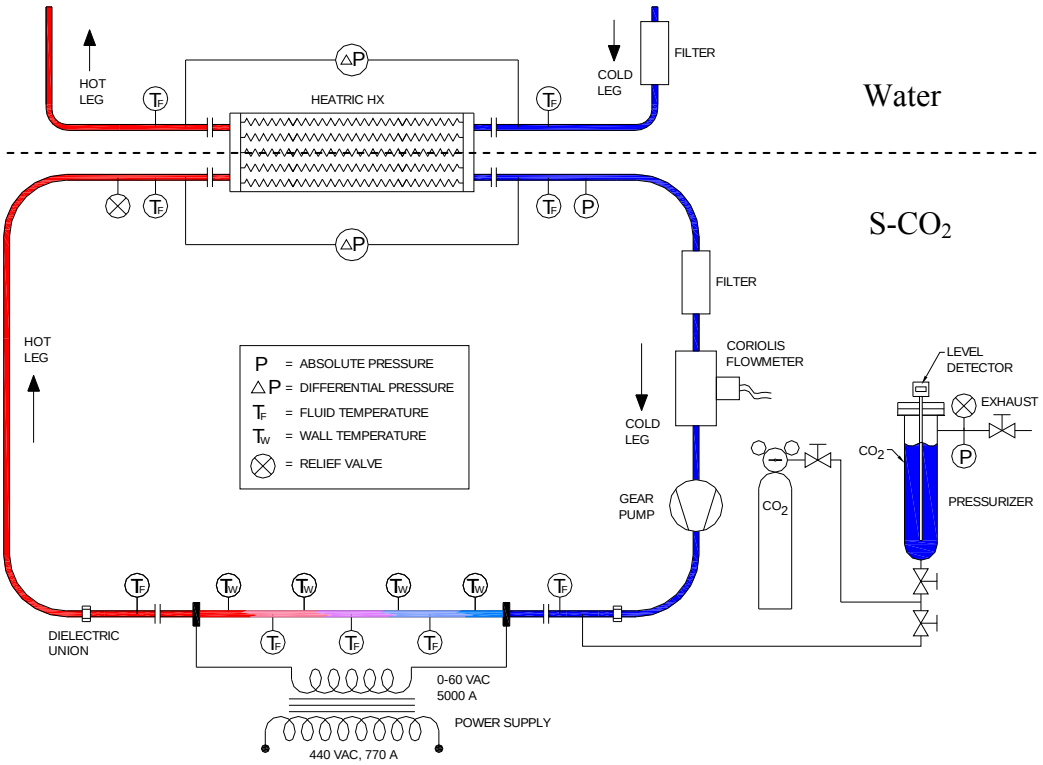

Figure 2.1: Experimental Loop Schematic

The S-CO_2 side of the heat exchange loop was composed of 316 stainless steel 21.3 mm O.D. schedule 80 (14 mm I.D.) pipe. The S-CO_2 was heated by passing a low

voltage, AC current through a 1 m section of the pipe. Temperature measurements along the wall of the heated section were obtained by 9 K-type thermocouples. Two platinum Resistance Thermal Detectors (RTDs) were used to measure the S-CO_2 temperature at the inlet and outlet of the heat exchanger. An absolute pressure transducer was located at the outlet of the heat exchanger. Differential pressure transducers were located at the S-CO_2 inlet and outlet of the heat exchanger. An in-line filter was placed before a mass flowmeter, followed by a gear pump used to circulate the S-CO_2. Additionally, a pressurizer, a CO_2 reservoir tank, and a helium reservoir tank were also attached to the S-CO_2 side of the heat exchanger apparatus. The helium tank was used to check for system leaks, and was not used during experimentation due to concerns of helium mixing with S-CO_2 in the experimental loop. A rupture disk, located before the S-CO_2 heat exchanger inlet, was used to provide over-pressure protection.

Building water in a once-through flow configuration was used as a heat sink on the other side of the heat exchanger. An in-line filter was installed before the water inlet. Inlet and outlet temperatures were measured with platinum RTDs. A differential pressure transducer was used to measure the pressure drop across the heat exchanger. A mass flow meter was used to measure the water flow rate.

2.1 Printed Circuit Heat Exchanger (PCHE)

The PCHE examined in this work is a compact heat exchanger manufactured by Heatric, a subsidiary of Meggitt (U.K.) Ltd. This type of heat exchanger has been used primarily in the upstream hydrocarbon processing, petrochemical and refining industries to this point [11]. However, there is little experience in using this type of heat exchanger with S-CO_2 under reactor-relevant conditions. It is being considered for use because of its small size and its ability to withstand temperatures up to 900 ºC (1650 ºF) and pressures up to 60.0 MPa (9000 psi). For the same thermal duty and pressure drop, a PCHE is up to 85% smaller than an equivalent shell and tube heat exchanger. A relative size comparison is shown in Figure 2.2 [11].

Figure 2.2: Size Comparison of PCHE and Shell and Tube Heat Exchanger [11]

Flow paths through the PCHE are created by chemically etching steel plates, as is shown in Figure 2.3(a). These plates are then stacked together, as shown in Figure 2.3(b), to achieve the required heat exchange surface area. The individual plates are joined through the diffusion bonding process, which encourages grain growth across the initial plate boundaries. A micrograph of two diffusion bonded plates, illustrating the grain structure, is shown in Figure 2.3(c). The final result is a monolithic steel block heat exchanger body containing embedded flow channels. The diffusion bonding process allows the entire heat exchanger body to achieve parent metal strength, which allows for high operating temperatures and pressures.

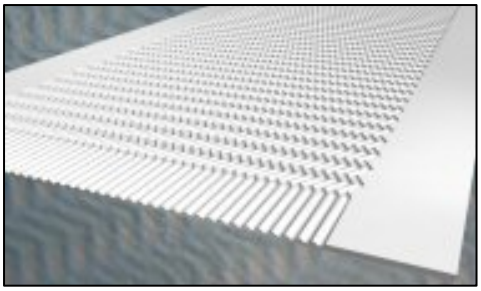

(a) Etched Plate

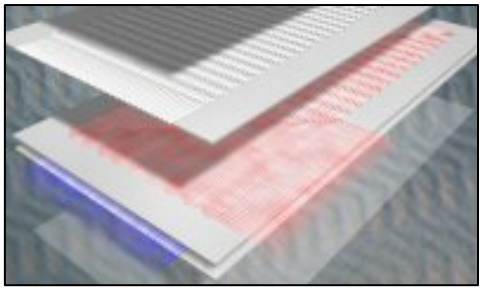

(b) Stacked Plates

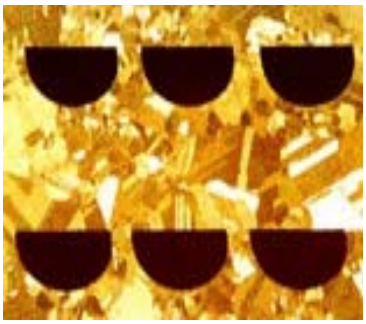

(c) Micrograph of Bonded PCHE Plates

Figure 2.3: PCHE Plates and Diffusion Bond [11]

The PCHE purchased by ANL for this study is rated for a maximum pressure of 21.6 MPa on the hot side and 8.3 MPa for the cold side. The overall dimensions of the heat exchanger are 120×200×1200 mm. The unit weighs 203 kg and has a rated heat exchange capacity of 17.5 kW. Figure 2.4 shows a top-down view of the PCHE with S-CO_2 and water inlets and outlets identified. It can be observed that the bulk of the heat exchanger length is in a counter-flow arrangement. Details of the PCHE provided by Heatric are shown in Table 2.1. From Table 2.1, it can be seen that the hydraulic diameter (0.92 mm), volumetric capacity (2 liters), and heat transfer area (5.6 m^2) are the same for both the hot and cold loops of the heat exchanger.

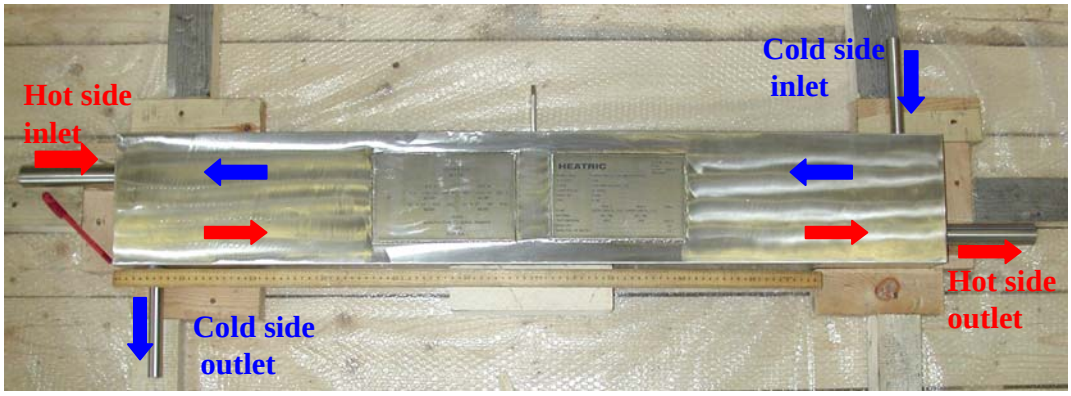

Figure 2.4: PCHE Inlets and Outlets

Table 2.1: PCHE Specifications from Heatric

	Hot side	Cold side
Design pressure (MPa)	8.3	21.6
Design temperature (^{o}C)	200	200
Flow area (mm^2)	1047	930
Number of channels	1176	1050
Hydraulic diameter (mm)	0.92	0.92
Capacity (liters)	2	2
Heat transfer area (m^2)	5.6	
Total mass (kg)	203	
Dimensions (mm)	120 × 200 × 1200	

3.2 Power Supply

The low voltage, AC current used to heat the S-CO_2 flowing through the primary side is supplied by a 300 kW power supply. Two 6" by ½" copper buss bars are used to deliver power from the power supply to the heated pipe section. Figure 2.5 shows the

power supply and buss bars. Two dielectric unions are used to electrically isolate the heated section from the rest of the primary loop. Nine K-type thermocouples are used to measure wall temperature along the 1 m heated length. A safety trip opens the breaker to the power supply if the wall temperature reaches 538°C. This value is set by ASME code B16.5.

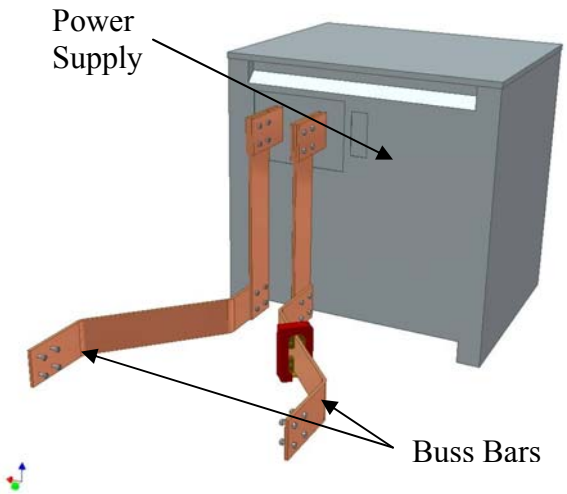

Figure 2.5: Power Supply and Buss Bars

2.3 Cooling System

During experimentation, building water in a secondary loop was used as a heat sink to remove heat from the primary loop. Water flows from a tank in the basement of the building through a 25 kW heater, helical tube-in-tube heat exchanger, and then to a drain. The annular region of the tube-in-tube heat exchanger is filled with a 10% ethylene glycol solution in water, and serves to provide cooling capability. The tube-in-tube heat exchanger, as installed, is shown in Figure 2.6. The heater and cooling coils allowed for adjustment of the water inlet temperature to the heat exchanger. The

maximum mass flow rate of water through the heat exchanger was approximately 1100 kg/hr. Water is also routed to the power supply to offer cooling during operation.

Figure 2.6: Tube-in-Tube Heat Exchanger

Before experiments were conducted, the primary loop was filled with CO_2. The reservoir supply pressure of approximately 6.0 MPa is well below the supercritical pressure of 7.4 MPa. In order to achieve the higher pressure, the helical tube-in-tube heat exchanger shown in Figure 2.6 was used to lower the water inlet temperature, lowering the temperature and pressure of the CO_2 flowing on the primary side and allowing the reservoir to input more fluid. Heating either the CO_2 or the incoming water allowed the CO_2 pressure to increase to a level above the 7.4 MPa critical pressure. The 10% ethylene glycol solution flowed in a loop through a model DE8AC GCI Icewagon chiller. The chiller has a cooling capacity of 25 kW with this percentage of ethylene glycol, and was able to adjust the solution temperature by 0.1°C. The chiller is shown in Figure 2.7.

Figure 2.7: GCI Icewagon Chiller

2.4 Pressurizer

In trial runs, it was observed that S-CO_2 is very sensitive to small changes in temperature and pressure. A pressurizer was used to increase the total loop volume and accommodate thermal expansion of the S-CO_2 as it is heated from the liquid state at room temperature to a supercritical state. The extra volume provided by the pressurizer helps to dampen pressure fluctuations that might occur. The pressurizer increases the overall volume of the primary side from 3.0 L to 4.9 L. It is constructed from 88.9 mm O.D. schedule 40 pipe (78 mm I.D.). The S-CO_2 level in the pressurizer is measured by a Mercap capacitance sensor manufactured by Milltronics Process Inc. The level sensor has a measurement range of 0-500 mm HG with an accuracy of 0.1% of the measured value and is rated for temperatures as high as 200^{o}C. The pressurizer is shown in Figure 2.8.

Figure 2.8: Pressurizer

2.5 Pump

A Micropump model 5K magnetic drive gear pump was used to circulate S-CO_2 through the primary loop. This pump uses two thermoplastic gears to compress S-CO_2 against the outer pump housing and create forced fluid flow. Magnets are used to couple the pump drive gear to the motor. This construction method has an advantage in that it eliminates the possibility of fluid leaking in the motor, so that only the pump body itself need be sealed. The pump is made from 316 stainless steel with carbon bearings and PTFE (PolyTetraFluoroEthylene) O-rings, and is coupled to a ½ horsepower TEFC (Totally Enclosed, Fan Cooled) motor. The motor speed is controlled by a variable frequency drive. Figure 2.9 shows the pump and motor as installed. Figure 2.10 shows the pump gears with the outer pump housing removed.

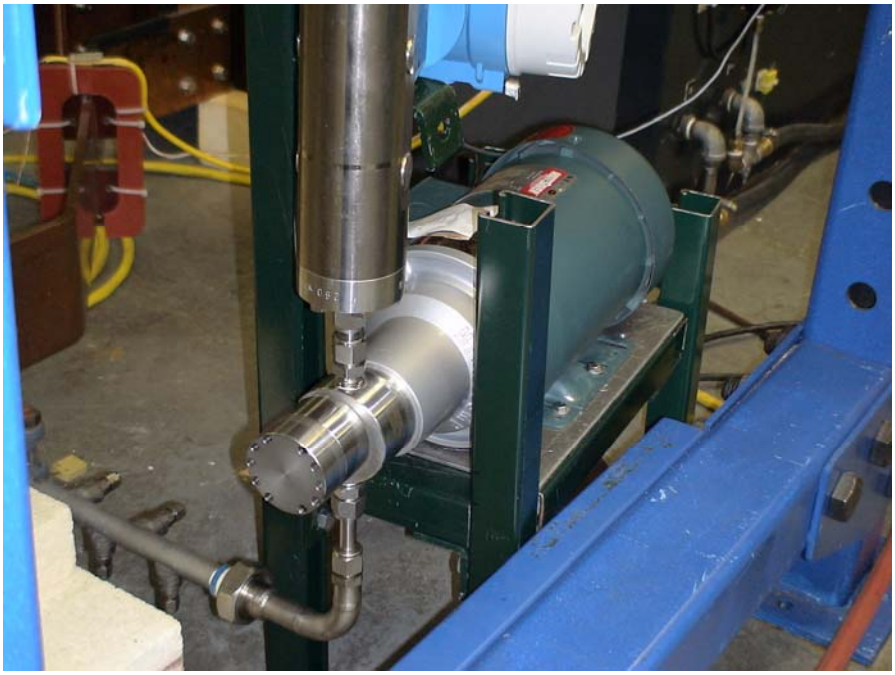

Figure 2.9: Micropump 5K Pump and Motor

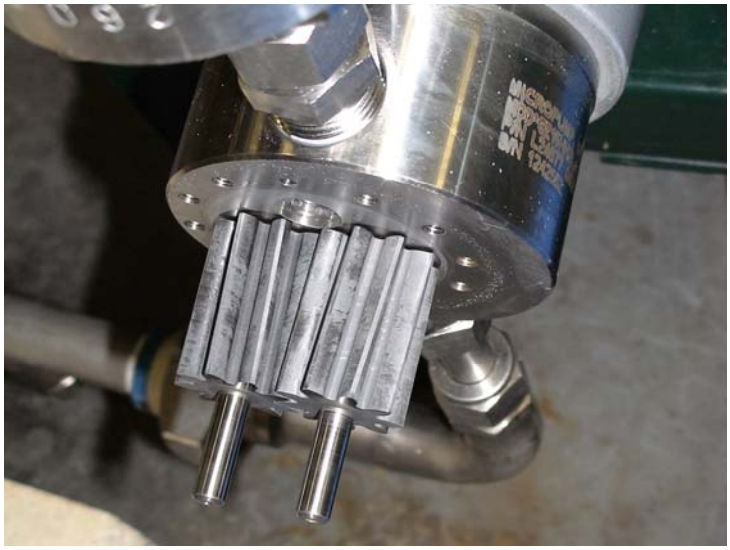

Figure 2.10: Micropump 5K Gears

The pump encountered significant operational issues when placed in a S-CO_2 environment, operating normally for approximately 3-4 hours and then seizing. After the CO_2 was removed from the primary loop, and the pump exposed to atmospheric air for 24

hours, it would again operate normally. All materials used in the pump were checked for material compatibility with CO_2. The gears used in the pump were initially manufactured from the material PEEK (Polyetheretherketone), an injection molded thermoplastic. While this material is inert with CO_2 in the liquid or gaseous states, it swells in the presence of supercritical CO_2. Measurements were taken of the driven gear immediately after removal from the S-CO_2 environment, 3.25 hours later, and 23.75 hours later. Gear length was measured in 3 different locations and outside diameter (O.D.) was measured in 9 different locations. These measurements are shown in Table 2.2. The difference values shown are the initial measurements minus the values at 23.75 hours after removal.

Table 2.2: PEEK Gear Measurements

Initial measurements	3.25 hours	23.75 hours	Difference
Length (in)	**Length (in)**	**Length (in)**	**Length (in)**
1.2520	1.2508	1.2500	0.0020
1.2520	1.2514	1.2510	0.0010
1.2530	1.2511	1.2505	0.0025
OD (inches)	**OD (inches)**	**OD (inches)**	**OD (inches)**
0.9390	0.9387	0.9384	0.0006
0.9390	0.9385	0.9378	0.0012
0.9390	0.9383	0.9379	0.0011
0.9392	0.9387	0.9380	0.0012
0.9390	0.9383	0.9379	0.0011
0.9380	0.9375	0.9370	0.0010
0.9400	0.9393	0.9391	0.0009
0.9393	0.9384	0.9380	0.0013
0.9388	0.9379	0.9375	0.0013

It can be seen from Table 2.2 that the overall change in length and O.D. is small (less than 0.003"). However, the pump tolerances are very tight, and this change was enough to cause the pump to mechanically bind. This problem was eliminated by remanufacturing the gears from PPS (PolyPhenylene Sulfide).

2.6 Instrumentation

Absolute and differential pressures were measured for the primary CO_2 side of the heat exchanger during experimentation. Absolute pressure was measured after the heat exchanger outlet and before the pump, using a Rosemount model 2088 pressure transducer. For this study, steady state conditions were based on the reading of this pressure transducer. Steady state was defined as a pressure fluctuation of less than or equal to 0.005 MPa over a period of 2 minutes. Pressurizer pressure was also measured using a Rosemount model 2088 pressure transducer. Differential CO_2 and water pressure across the heat exchanger were measured using a Rosemount model 3051 differential pressure transducer. Rosemount 2088 and 3051 pressure transducers are shown in Figure 2.11 [44]. Accuracy and physical dimensions of the pressure transducers are listed in Table 2.3 [44].

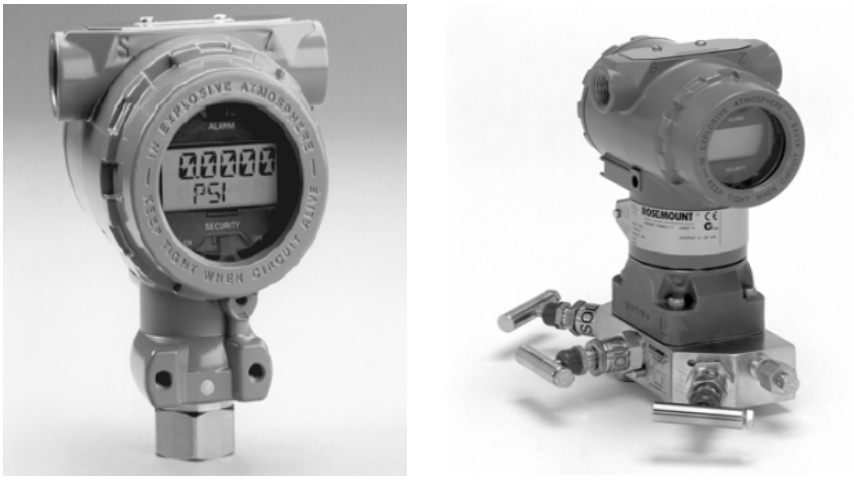

Figure 2.11: Rosemount Model 2088 and 3051 Pressure Transducers

Table 2.3: Rosemount Pressure Transducer Specifications

Model	2088	3051
Accuracy	± 0.020 MPa	± 0.03 kPa
Weight	2.44 lb (1.11 kg)	6.0 lb (2.72 kg)
Dimension	3.9 x 5.0 x 5.4 in (99 x 127 x 137 mm)	6.4 x 3.2 x 7.8 in. (163 x 81 x 198 mm)

PROline Promass 80M Coriolis flow meters, manufactured by Endress-Hauser, were used to measure mass flow rate for both the S-CO_2 primary and water secondary loops. These flow meters have a temperature limit of 350°C and a pressure limit of 35.0 MPa. They automatically take into account varying fluid properties such as density and viscosity to measure mass flow rate with no correction required, and have an accuracy of ±0.5%. The primary side flow meter was installed at the outlet of the heat exchanger, after an in-line filter, and before the circulating pump. The water flow meter was installed at the outlet of the heat exchanger. Figure 2.12 shows the S-CO_2 side flow meter connected to the Micropump model 5K pump.

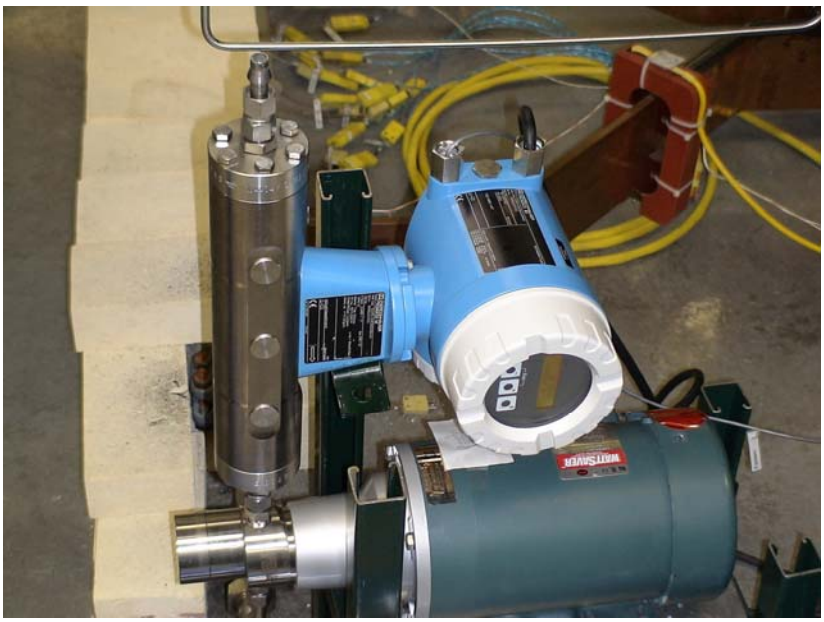

Figure 2.12: PROmass 80M Flowmeter

Temperature was measured at the inlets and outlets of both the primary and secondary side using platinum RTDs (Resistance Temperature Detectors) manufactured by Ari Industries. These RTDs have an accuracy of ±0.1°C.

Data acquisition and monitoring tasks were managed by a PC running LabVIEW 6.i on a Window 2000 operating system. Temperature, pressure, and mass flow sensors were connected to a HP model E1345A 16-channel multiplexer and were converted to digital signals by a HP model E1326B 5 ½ digit multimeter. The power supply was controlled and monitored through a panel located next to the computer monitors showing experimental parameters under examination. The data acquisition system and power supply control panel are shown in Figure 2.15.

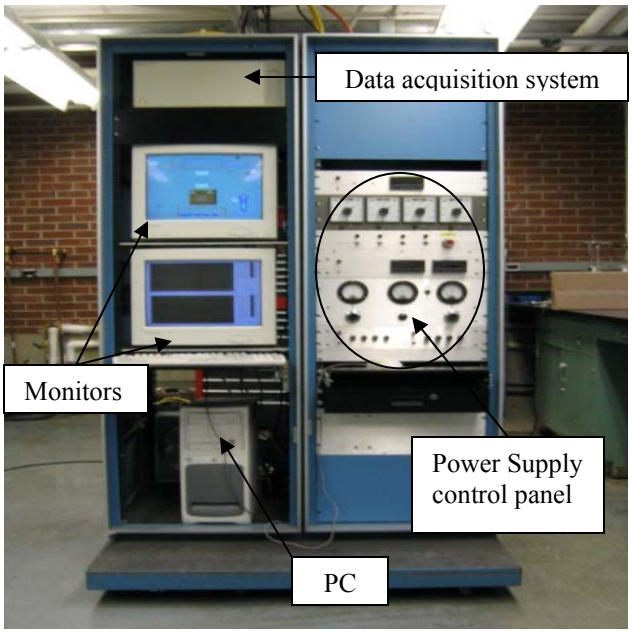

Figure 2.15: Data Acquisition System and Power Supply Control

CHAPTER 3 – PCHE Internal Configuration Estimation

3.1 Channel Configuration

The heat exchanger examined in the present work is a Printed Circuit Heat Exchanger (PCHE) manufactured by Heatric. Under the ANL contract with Heatric, detailed design information of the PCHE is proprietary and thus was not supplied. However, a partial listing of specifications was provided. These are shown in Table 3.1.

Table 3.1: PCHE Design Specifications

	Hot Side	**Cold Side**
Design Pressure, MPa	8.3	21.6
Design Temperature, ºC	200	200
Flow Area, mm^2	1047	930
Number of Channels	1176	1050
Hydraulic Diameter, mm	0.92	0.92
Flow Channel Configuration	Semi-circle	Semi-circle
Volumetric Capacity, Liters	2	2
Heat Transfer Area, m^2	5.6	5.6
Total Mass, kg	203	
Outer Dimensions (H x W x L), mm	120 × 200 × 1200	
Design Heat Load, kW	17.5	

Heatric did not supply information about the interior geometry of the ANL PCHE. The only published literature showing detailed design information of a PCHE is provided by Ishizuka et al. [15] of the Tokyo Institute of Technology (TiTech). TiTech tested a PCHE with CO_2 on both the hot and cold sides of their heat exchanger. When they concluded testing, they mechanically disassembled their PCHE and measured the interior geometry. Table 3.2 shows measured quantities as well as specifications provided by Heatric for the TiTech PCHE. Since there are no other published works describing the interior geometry of a PCHE, and information about the interior geometry of the ANL

PCHE was not provided, it is assumed that the TiTech and ANL PCHE units have similar interior geometry. This allows the interior geometry of the ANL PCHE to be estimated.

Table 3.2: TiTech PCHE Specifications

	Hot Channel	**Cold Channel**
Plate Material	SS316L	SS316L
Plate Thickness, mm	1.63	1.63
Number of Plates	12	6
Number of Channels	144	66
Flow Channel Bend Angle, degrees	115	100
Vertical Pitch, mm	4.50	3.62
Horizontal Pitch, mm	2.97	3.25
Flow Channel Configuration	Semi-circle	Semi-circle
Wall Width, mm	0.60	0.70
Channel Diameter, mm	1.88	1.88
Channel Hydraulic Diameter, mm	1.15	1.15
Heat Transfer Area, m^2	0.697	0.356
Channel Cross-Sectional Area, m^2	0.00020	0.000092
Channel Active Length, mm	1000	1100
Inlet and Outlet Header Length, mm	49.0	46.5
Outer Dimensions (H x W x L), mm	71 × 76 × 896	
Design Heat Load, kW	3	

Based on the information supplied by Heatric for the ANL PCHE, an approach was developed to calculate an estimate of the interior channel geometry. This approach will first be applied to the TiTech PCHE to verify its validity.

Based on the given channel hydraulic diameter of 1.15 mm for the TiTech PCHE, the semi-circular channel diameter can be calculated through the geometric relation

$$D_h = 1.15\,\text{mm} = \frac{4A_c}{P} = \frac{4 \cdot \frac{1}{2} \cdot \frac{\pi D^2}{4}}{D + \frac{\pi D}{2}} = \frac{\pi D}{\pi + 2}, \tag{3.1}$$

from which,

$$D = \frac{(\pi + 2) \cdot D_h}{\pi} = \frac{(\pi + 2) \cdot 1.15\,\text{mm}}{\pi} = 1.88\,\text{mm} \tag{3.2}$$

where A_c and P are the channel cross-sectional area and wetted perimeter, respectively, and D is the channel diameter. From Equation 3.2, the channel diameter is calculated to be 1.88 mm.

The channel flow length can be calculated from the given heat transfer area and the channel cross-sectional area.

$$Travel\ Length_{TiTech,Hot} = \frac{Heat\ Transfer\ Area}{Cross\ Section\ Perimeter \times No.\ of\ Channels}$$
$$= \frac{6.97\times10^{5}\ \text{mm}^2}{\left(1.88\,\text{mm} + \frac{1.88\,\text{mm}\times\pi}{2}\right)\times144} = 1001\,\text{mm} \qquad (3.3)$$

A similar calculation for the cold side of the TiTech PCHE yields a travel length of 1115 mm. These are in close agreement with the stated values of 1000 mm and 1100 mm for the hot and cold sides, respectively.

The channel bending angles are related to the PCHE core length and the channel travel length. The core length is calculated by subtracting the lengths of the inlet and outlet headers from the PCHE outside dimensions. For the TiTech PCHE, the hot and cold header lengths are 49.0 mm and 46.5 mm. With the overall length of 896 mm, the PCHE core lengths are 847 mm and 849.5 mm for the hot and cold side, respectively. The relation between the channel bending angle, travel length, and PCHE core length is shown schematically in Figure 3.1.

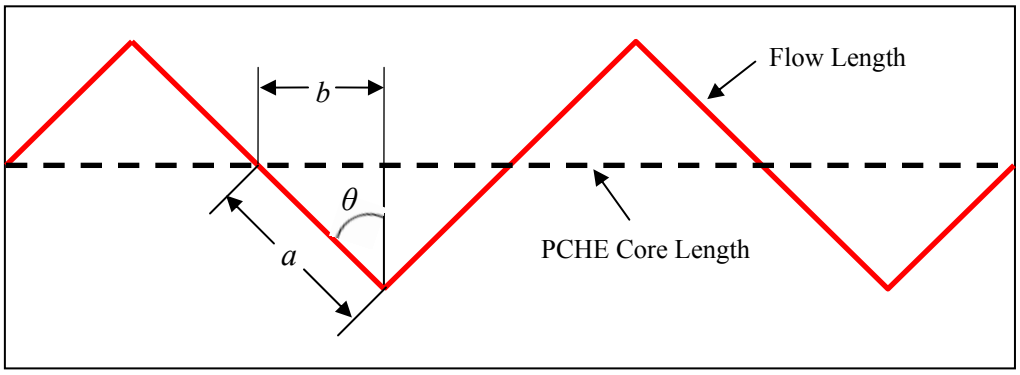

Figure 3.1: Simplified PCHE Channel Shape [33]

The half bending angle θ can be calculated through a geometric relationship by

$$\theta = \sin^{-1}\left(\frac{b}{a}\right). \tag{3.4}$$

For the TiTech PCHE, the half bending angles are

$$\theta_{TiTech,h} = \sin^{-1}\left(\frac{847}{1000}\right) = 57.9^{\circ} \tag{3.5}$$

and

$$\theta_{TiTech,c} = \sin^{-1}\left(\frac{849.5}{1100}\right) = 50.6^{\circ}. \tag{3.6}$$

Doubling the half bending angle values in Equations 3.4 and 3.5 yields full channel bending angles of 115.8º and 101.2º for the hot and cold channels. These are in close agreement with the stated values of 115º and 100º. Therefore, it is reasonable to use this approach to calculate the bending angles inside the ANL PCHE using the values given in Table 3.1.

The diameter of the semi-circular ANL PCHE channels are calculated to be 1.506 mm through the equation

$$D_{ANL} = \frac{(\pi + 2)\cdot D_h}{\pi} = \frac{(\pi + 2)\cdot 0.92\,\text{mm}}{\pi} = 1.506\,\text{mm}. \tag{3.7}$$

Given the channel diameter, the bending angles can be calculated by relating the channel travel length to the PCHE core length. However, Heatric did not provide information about the inlet and outlet header lengths or the channel travel lengths in the ANL PCHE. In the TiTech PCHE, the headers account for approximately 5% of the overall heat exchanger length for both the hot and cold sides. Assuming the same proportions in the ANL PCHE, the header length is 60 mm and the ANL PCHE core length is approximately 1140 mm.

The channel flow lengths can be calculated by relating the specified heat transfer area to the channel cross-sectional perimeter as shown in Equation 3.3 above.

$$\begin{aligned} Travel\ Length_{ANL,Hot} &= \frac{Heat\ Transfer\ Area}{Cross\ Section\ Perimeter \times No.\ of\ Channels} \\ &= \frac{5.6\times10^{6}\ \text{mm}^2}{\left(1.506\,\text{mm} + \frac{1.506\,\text{mm}\times\pi}{2}\right)\times 1176} = 1230\,\text{mm} \end{aligned} \tag{3.8}$$

and

$$Travel\ Length_{ANL,Cold} = \frac{Heat\ Transfer\ Area}{Cross\ Section\ Perimeter \times No.of\ Channels}$$
$$= \frac{5.6\times10^{6}\ \text{mm}^2}{\left(1.506\,\text{mm} + \frac{1.506\,\text{mm}\times\pi}{2}\right)\times1050} = 1378\,\text{mm} \quad . \tag{3.9}$$

Using the channel travel lengths calculated in Equations 3.8 and 3.9 along with the estimated PCHE core length of 1140 mm, the half bending angles inside the ANL PCHE can be estimated as

$$\theta_{ANL,h} = \sin^{-1}\left(\frac{1140}{1230}\right) = 67.9^{\circ} \tag{3.10}$$

and

$$\theta_{ANL,c} = \sin^{-1}\left(\frac{1140}{1378}\right) = 55.8^{\circ}\,. \tag{3.11}$$

Thus, the full bending angles for the ANL PCHE are 135.8º and 111.6º for the hot and cold side channels, respectively. With the full bending angles, the interior channel geometry of the ANL PCHE can be fully described by the channel vertical pitch, channel horizontal pitch, or the total number of bends in the channel. However, with the information supplied by Heatric and TiTech, it is not possible to directly calculate the horizontal or vertical pitch of the channels inside the ANL PCHE. To this end, a commercially available Computational Fluid Dynamics (CFD) program was used to simulate fluid flow inside the PCHE channels. Results from the CFD simulations were compared to pressure drop data taken by Song [33] with constant temperature water on both the hot and cold sides of the heat exchanger. Tables 3.3 and 3.4 show the experimental data used for comparison with the CFD results for the hot and cold sides of the heat exchanger, respectively. For compact heat exchangers, such as the PCHE, approximately 90% of the total pressure drop is due to friction in the heat exchanger core [3]. These 90% values of the measured pressure drop will be used for comparison as only channels through the PCHE core are modeled. The 90% value of pressure drop data from Tables 3.3 and 3.4 are plotted versus mass flow rate in Figures 3.2 and 3.3 along with a power function curve fit.

Table 3.3: Hot Side Pressure Drop Data – Water

Test	m_h (kg/hr)	Re	T_h (ºC)	ΔP_h (kPa)	90% ΔP_h (kPa)
Hot PD 1	190.12	84.88	50.0	1.40	1.26
Hot PD 2	310.53	138.98	50.2	2.55	2.30
Hot PD 3	400.73	179.25	50.1	3.71	3.34
Hot PD 4	600.28	268.28	50.1	6.61	5.95
Hot PD 5	805.05	359.57	50.0	10.57	9.51
Hot PD 6	999.34	445.46	49.9	15.06	13.55
Hot PD 7	1199.13	535.31	50.0	20.20	18.18

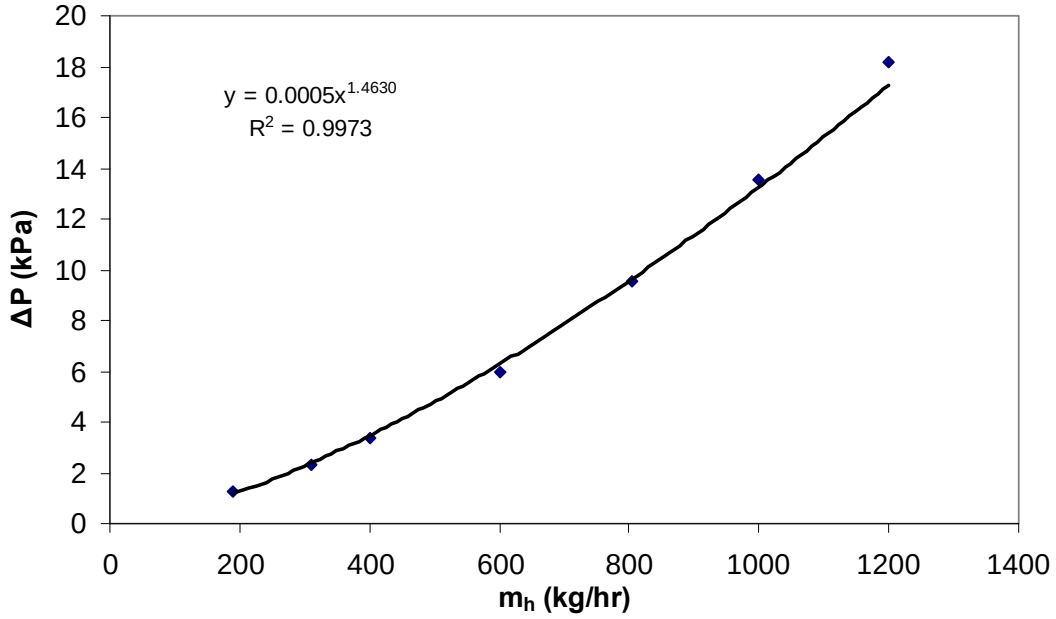

Figure 3.2: Hot Side Pressure Drop Data [33]

Table 3.4: Cold Side Pressure Drop Data – Water

Test	m_c (kg/hr)	Re	T_c (ºC)	ΔP_c (kPa)	90% ΔP_c (kPa)
Cold PD 1	153.27	77.30	50.2	1.66	1.49
Cold PD 2	309.32	155.81	50.1	4.62	4.16
Cold PD 3	517.01	260.58	50.2	10.11	9.10
Cold PD 4	703.00	355.57	50.4	17.17	15.45
Cold PD 5	981.15	494.81	50.2	29.94	26.95
Cold PD 6	1199.21	605.13	50.3	42.11	37.90

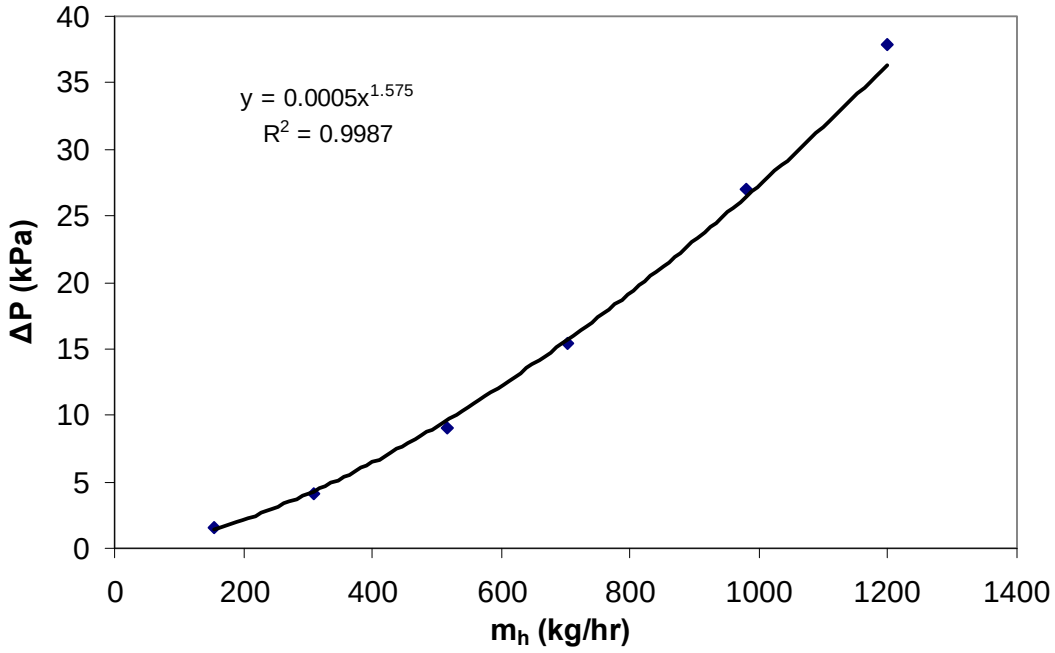

Figure 3.3: Cold Side Pressure Drop Data [33]

The angles of the ANL PCHE are fixed through Equations 3.10 and 3.11 shown above. Thus, one additional variable is needed to fully define the interior geometry if the channels have sharp bends. However, it is known that Heatric manufacturing methods produce bends with a radius. This fillet radius introduces yet another variable needed to describe the interior geometry. Figure 3.4 shows a simplified version of the ANL PCHE channels. The symbols P_v, P_h, and θ represent the vertical pitch, horizontal pitch, and half bending angle, respectively.

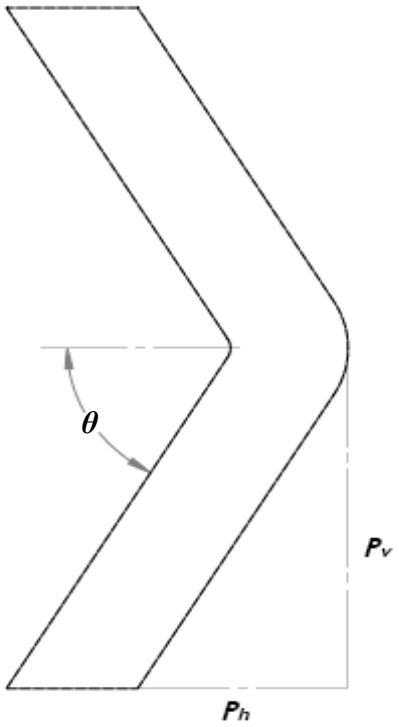

Figure 3.4: Simplified Channel Geometry

Ishizuka et al. [15] measured the vertical pitch for the TiTech PCHE. These values were 4.50 mm and 3.62 mm for the hot and cold sides, respectively. Based on this, it was assumed that the vertical pitch of the ANL PCHE channels was in the range of 2-10 mm. Information on the channel fillet radius was not supplied by either Heatric or TiTech. Fillet radius values of 0.75, 1.0, 1.25, 1.5, 1.75, and 2.0 mm were examined with varying vertical pitch lengths. With a fillet radius of less than 0.75 mm, the inside of the channel bend is sharp. Thus, fillet radius values less than 0.75 mm were not examined. For the cold side, fillet radius values greater than 1.0 mm led to a vertical pitch length less than 2.0 mm and fillet values larger than 1.0 mm were not examined for the cold side. For the hot side, fillet radius values greater than 2.0 mm led to a vertical pitch length less than 2.0 mm, so hot side fillet values greater than 2.0 mm were not examined.

The water flow rate used for these simulations was 700 kg/hr. This flow rate was selected for simulation because a majority of the S-CO_2 – water heat transfer experiments were conducted with a flow rate of 700 kg/hr on the cold side. It is also an intermediate

value for the building water supply capabilities, which ranged from approximately 100 kg/hr to 1400 kg/hr. For the cold side of the PCHE, pressure drop test Cold PD 4 used a mass flow rate 703 kg/hr. The 90% pressure drop value for this test was 15.45 kPa. For the hot side, testing was not conducted near 700 kg/hr and the power function best fit correlation shown in Figure 3.2 is used to calculate the 90% pressure drop value for a flow rate of 700 kg/hr on the hot side.

$$90\%\,\Delta P_h = 0.000514 \times \left(\dot{m}_h \right)^{1..575} = 0.000514 \times 700^{1.575} = 15.56\,\text{kPa}\,. \tag{3.12}$$

Table 3.5 shows the vertical pitch length which most closely matches the 90% pressure drop data for a given fillet radius, along with the corresponding horizontal pitch, experimental and simulated pressure drop, and the error between these values. The error value presented in Table 3.5 is calculated by

$$Error = \frac{\left(\Delta P_{CFD} - \Delta P_{\text{exp}}\right)}{\Delta P_{\text{exp}}} \times 100\,. \tag{3.13}$$

Table 3.5: Possible Channel Geometries

PCHE Side	Fillet Radius	P_v	P_h	Exp. ΔP	CFD ΔP	Error
	mm	mm	mm	kPa	kPa	%
Hot	0.75	7.0	2.83	7.86	7.88	0.24
	1.00	6.0	2.42	7.86	7.90	0.49
	1.25	5.5	2.22	7.86	7.856	-0.08
	1.50	4.5	1.82	7.86	7.83	-0.37
	1.75	3.75	1.52	7.86	7.88	0.24
	2.00	2.5	1.03	7.86	7.82	-0.51
Cold	0.75	3.5	2.36	15.45	15.54	0.56
	1.00	3.0	2.02	15.45	15.53	0.49

The channel geometries presented in Table 3.5 are possible configurations only. Use of different fillet radius values in the CFD simulations will result in different vertical and horizontal pitch lengths. Table 3.5 is not intended to provide the definitive interior geometry of the ANL PCHE; instead, it is meant to show that there is a method available to make a reasonable estimate of the geometry based on experimental data. The information provided by Heatric and TiTech is not sufficient to select the most probable

channel geometry from the range of possible configurations. However, this method narrows the range of possibilities to a reasonable number that can be used in heat transfer simulations to further refine the geometry until a model is able to reproduce both the pressure drop and heat transfer characteristics of the ANL PCHE.

3.2 Plate Configuration

The TiTech PCHE uses a double-banking plate configuration, with one plate of 11 cold channels between two plates of 12 hot channels. Figure 3.5 shows the configuration of the hot and cold channels inside the TiTech PCHE.

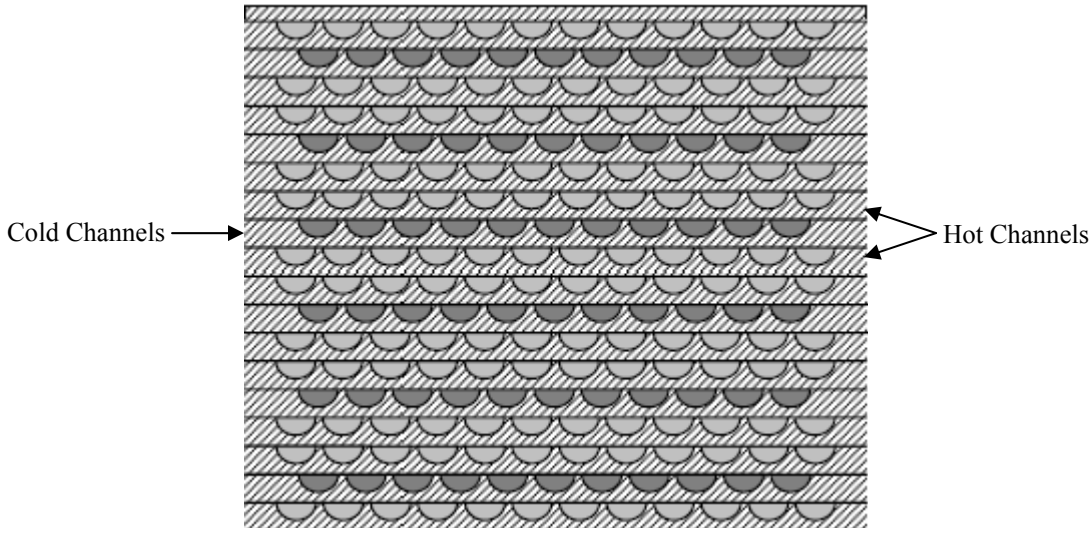

Figure 3.5: TiTech Channel Configuration [15]

The ANL PCHE has a similar number of channels on both the hot and cold sides (1176 versus 1050). This is different from the TiTech PCHE, where the number of hot channels is more than double the number of cold channels (144 versus 66). This implies that the ANL PCHE does not use a double-banking configuration, and therefore has one hot plate per cold plate. Table 3.6 shows the number of hot and cold channels per plate

for the possible ANL PCHE plate configurations, assuming an equal number of hot and cold side plates.

Table 3.6: Possible ANL PCHE Plate Configurations

Configuration	Number of Plates per Side	Hot Channels	Cold Channels
ANL 1	14	84	75
ANL 2	21	56	50
ANL 3	42	28	25

In order to select one of the possible configurations in Table 3.6 as the most probable, more information is needed about the vertical and horizontal dimensions of the PCHE core. With the information provided by Heatric, it is not possible to calculate the plate thickness, the metal thickness between individual channels, or the thickness of the outside walls at the top, bottom, and sides of the heat exchanger. In order to estimate these, proportions from the TiTech PCHE will be applied to the ANL PCHE.

The side wall thickness (Th_{SW}) of the TiTech PCHE can be calculated using the hot side number of channels (N_{hc}), channel diameter (D), wall thickness between channels (T_w), channel horizontal pitch (P_{hor}), and the outer width of the heat exchanger (W_{PCHE}). These values are listed in Table 3.2 for the TiTech PCHE. The side wall thickness can be calculated through the equation

$$\begin{aligned}\left(Th_{SW}\right)_{TiTech} &= \frac{W_{PCHE} - N_{hc} \times D - \left(N_{hc} - 1\right) \times T_w - P_{hor}}{2} \\ &= \frac{76\,\text{mm} - 12 \cdot 1.88\,\text{mm} - \left(12 - 1\right) \cdot 0.6\,\text{mm} - 2.97\,\text{mm}}{2} = 21.9\,\text{mm}\end{aligned} \quad (3.14)$$

A similar calculation using values for the TiTech cold side yields a side wall thickness of 22.5 mm.

The thickness of the top and bottom walls (Th_{TB}) can be calculated using the outside height TiTech PCHE (H_{PCHE}), the total number of plates (N_P), and the plate thickness (Th_P). These values are listed in Table 3.2. The top and bottom wall thickness can be calculated through the equation

$$\left(Th_{TB}\right)_{TiTech} = \frac{H_{PCHE} - \left(N_P \times Th_P\right)}{2} = \frac{71\,\text{mm} - \left(18 \cdot 1.63\,\text{mm}\right)}{2} = 20.8\,\text{mm}\,. \qquad (3.15)$$

In order to calculate the wall thicknesses for the ANL PCHE, the wall thickness between channels and the plate thickness must first be estimated. It is assumed that the ratio of these dimensions to the semi-circular diameter, D, are the same as in the TiTech PCHE. Due to the larger number of hot channels relative to cold channels in the possible ANL PCHE configurations listed in Table 3.6, the TiTech hot side wall thickness will be used in ratio calculations. For the TiTech PCHE, these ratios are

$$\left(\frac{T_w}{D}\right)_{TiTech} = \frac{0.60\,\text{mm}}{1.88\,\text{mm}} = 0.319\,, \qquad (3.16)$$

and

$$\left(\frac{Th_P}{D}\right)_{TiTech} = \frac{1.63\,\text{mm}}{1.88\,\text{mm}} = 0.867\,. \qquad (3.17)$$

Using the ratios in Equations 3.15 and 3.16 with the ANL PCHE channel diameter of 1.506 mm yields the following values:

$$\left(T_w\right)_{ANL} = 0.48\,\text{mm} \qquad (3.18)$$

$$\left(Th_P\right)_{ANL} = 1.31\,\text{mm}\,. \qquad (3.19)$$

These values will be used with the possible configurations listed in Table 3.6 to select the most probable plate configuration inside the ANL PCHE. Sidewall thickness (Th_{SW}) for the ANL PCHE is calculated using Equation 3.14. Based on information available, it is not possible to precisely calculate the horizontal pitch for the ANL PCHE. Thus, this term is left out of the Th_{SW} calculation for the ANL PCHE seen in Equation 3.14. Top and bottom wall thickness (Th_{TB}) for the ANL PCHE is calculated using Equation 3.15. Table 3.7 shows the side wall thickness, top and bottom wall thickness, ratio of side wall thickness to outer thickness, and ratio of the top and bottom wall thickness to the outer height for the TiTech PCHE as well as possible configurations ANL 1, ANL 2, and ANL 3.

Table 3.7: ANL Plate Configuration Evaluation

	Th_{SW} (mm)	Th_{TB} (mm)	$\frac{Th_{SW}}{W_{PCHE}}$	$\frac{Th_{TB}}{H_{PCHE}}$
TiTech	22	20.8	0.29	0.29
ANL 1	16.8	41.7	0.08	0.35
ANL 2	44.6	32.5	0.22	0.27
ANL 3	72.4	5.0	0.36	0.04

Based on the ratios shown in Table 3.7, ANL 2 is the most probable plate configuration. ANL 2 consists of 42 alternating hot and cold plates, with 56 channels per hot plate and 50 channels per cold plate. Table 3.8 shows the estimated ANL PCHE dimensions calculated previously. Channel vertical and horizontal pitches are not presented as there is not a reasonable method, given the information available, to determine the most probable configuration from the possible geometries shown in Table 3.5.

Table 3.8: Estimated ANL PCHE Dimensions

	Hot	**Cold**
Channel Diameter, mm	1.506	1.506
Channel Travel Length, mm	1230	1378
Full Bend Angle, degrees	135.8	111.6
Number of Plates	21	21
Channels per Plate	56	50
Thickness between channels, mm	0.48	0.48
Plate Thickness, mm	1.31	1.31
Sidewall Thickness	44.6	
Top and Bottom Wall Thickness, mm	32.5	

CHAPTER 4 – Experimental Results

4.1 Supercritical Heat Transfer

Supercritical fluids are of interest in power conversion cycles because of their dramatic changes in thermophysical properties near the pseudocritical temperature at a given pressure. The pseudocritical temperature is defined as the temperature at which the specific heat of a fluid reaches a maximum point at a pressure above the critical pressure [46]. Up to this point, the most highly studied supercritical fluids are water and CO_2. Both fluids exhibit similar thermophysical property changes near their respective pseudocritical points. However, the critical temperature and pressure of CO_2 ($T_c = 30.98^{\circ}C$, $P_c = 7.377MPa$) are considerably lower than that of water ($T_c = 373.95^{\circ}C$, $P_c = 22.06MPa$). Figure 4.1(a) shows the temperature dependent variation of specific heat at constant pressure (C_p) and density (ρ) of CO_2 at a pressure of 7.5 MPa. Figure 4.1(b) shows the temperature dependence of viscosity (μ) and thermal conductivity (k) of CO_2 at a pressure of 7.5 MPa. Figures 4.2(a) and (b) show the same temperature dependent properties of water at a pressure of 22.5 MPa.

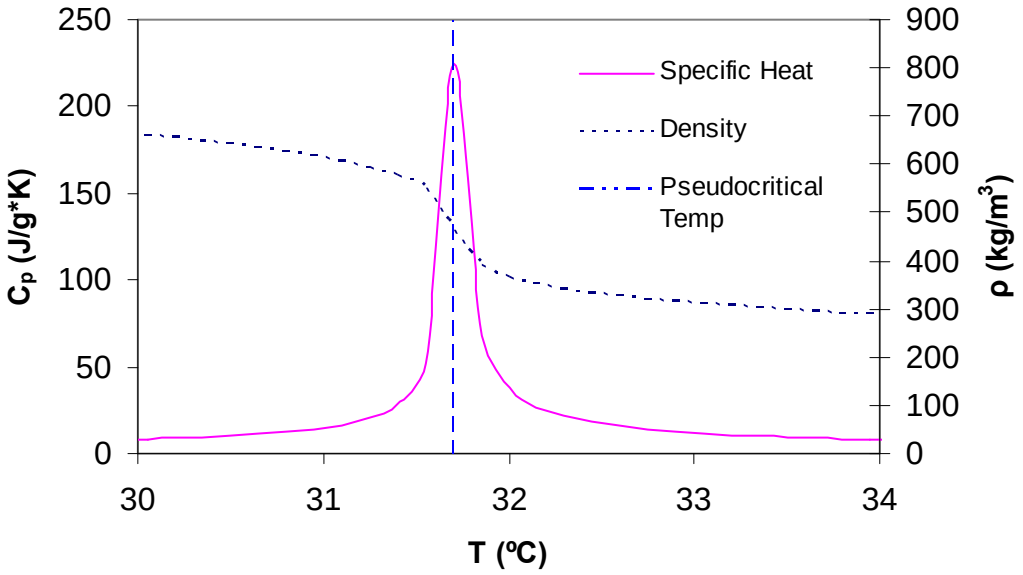

Figure 4.1(a): Specific Heat and Density of CO_2 at 7.5 MPa [47]

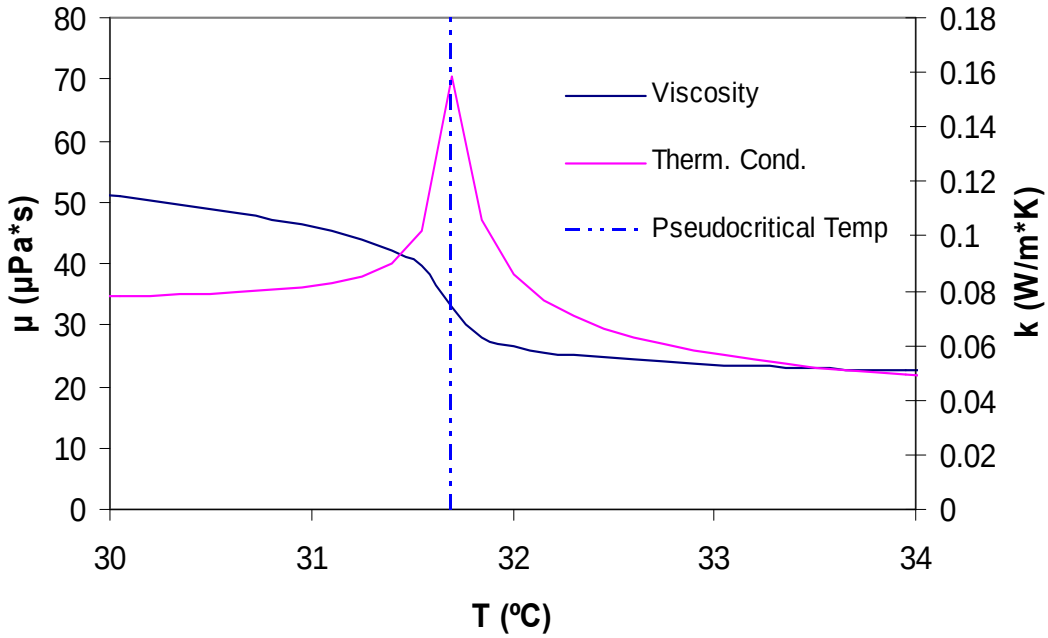

Figure 4.1(b): Viscosity and Thermal Conductivity of CO_2 at 7.5 MPa [47]

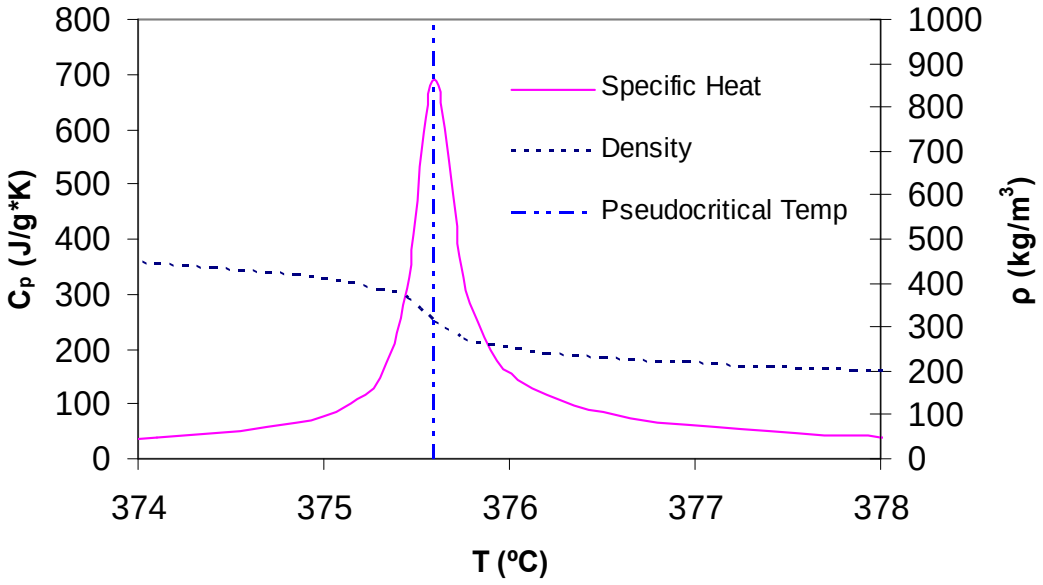

Figure 4.2(a): Specific Heat and Density of Water at 22.5 MPa [47]

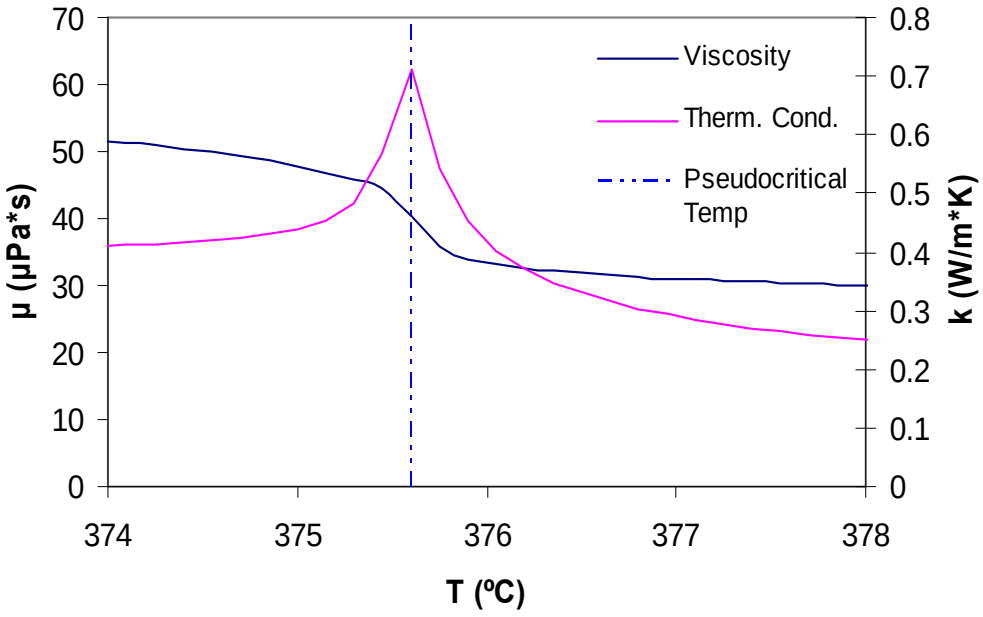

Figure 4.2(b): Viscosity and Thermal Conductivity of Water at 22.5 MPa [47]

While these fluids exhibit similar trends in thermophysical properties, S-CO_2 is being preferentially examined for a Brayton cycle power conversion system for advanced nuclear reactors due to its lower temperature and pressure, as well as its relative inertness with sodium in the case of a liquid sodium-cooled fast reactor. The thermophysical properties of CO_2 at supercritical pressures of interest: 7.4, 7.5, 8.0, 8.5, and 9.0 MPa are shown in Appendix D. The thermophysical properties of CO_2 near the pseudocritical point at the pressures listed previously show the same general trends as those in Figures 4.1(a) and 1.4(b). However, these variations become less pronounced at pseudocritical pressures further away from the critical pressure of 7.377 MPa for CO_2.

4.2 Data Analysis Method

The equation describing heat transfer between two fluids separated by a metal wall is given by

$$\frac{1}{UA} = \frac{1}{h_h A} + \frac{L}{kA} + \frac{1}{h_c A}, \tag{4.1}$$

where U is the overall heat transfer coefficient, A is the heat transfer area, k is the metal thermal conductivity, L is the metal thickness between hot and cold channels, and h_h and h_c are the hot and cold side heat transfer coefficients, respectively.

Analysis by Song [33] showed that thermal resistance to heat transfer of the metal wall separating hot and cold channels is negligible in the ANL PCHE. With this, and the knowledge that the heat transfer areas on the hot and cold sides are equal, Equation 4.1 reduces to

$$\frac{1}{U} = \frac{1}{h_h} + \frac{1}{h_c}. \tag{4.2}$$

Song tested the ANL PCHE with water on both the hot and cold sides and found that the cold side heat transfer coefficient could be described through a linear correlation with Reynolds number. This is given by

$$h_c = 11.04 \times \mathrm{Re}_{H_2O} + 570.36 . \quad (4.3)$$

The overall heat transfer coefficient, U, is defined by the equation

$$\dot{q} = UA\Delta T_{lm} , \quad (4.4)$$

where $\dot{q}$ is the heat transfer rate and ΔT_{lm} is the log mean temperature difference. For counter-flow heat exchangers, ΔT_{lm} is defined as

$$\Delta T_{lm} = \frac{\left(T_{h,out} - T_{c,in}\right) - \left(T_{h,in} - T_{c,out}\right)}{\ln\left[\left(T_{h,out} - T_{c,in}\right)/\left(T_{h,in} - T_{c,out}\right)\right]} . \quad (4.5)$$

The heat transfer rate, $\dot{q}$, is calculated using the measured S-CO_2 inlet and outlet temperatures. The NIST database [47] is used to calculated the S-CO_2 enthalpy based on these temperatures. The heat transfer rate is given by

$$\dot{q} = \dot{m}_h (i_{h,in} - i_{h,out}) . \quad (4.6)$$

With the calculated values for U and h_c, the heat transfer coefficient can be calculated through the equation

$$h_h = \left(\frac{1}{U} - \frac{1}{h_c}\right)^{-1} . \quad (4.7)$$

4.3 Small Temperature Difference Testing

Changes in thermophysical properties, especially specific heat, can have a dramatic effect on the heat transfer characteristics of a fluid near the pseudocritical point. Previous studies have shown heat transfer augmentation near the pseudocritical region for both S-CO_2 and supercritical water. The majority of these studies were conducted in straight circular tubes, with very few studies conducted using different channel geometries. Thus, the first objective of this work is to whether similar behavior is observed in the ANL PCHE.

For the small temperature difference tests, the difference between the S-CO_2 inlet and outlet was kept at a minimum (less than 1.5 ^oC) to more accurately observe the effect of varying thermophysical properties near the pseudocritical point. These tests were conducted with a S-CO_2 mass flow rate of 250 kg/hr, a water flow rate of 700 kg/hr, and a S-CO_2 pressure of 8.0 MPa. S-CO_2 outlet temperatures below, near, and above the pseudocritical temperature of 34.65 ^oC were examined. Table 4.1 shows the conditions tested, along with the pseudocritical temperature calculated through an equation proposed by Liao et al. [41], where the input pressure is in bar

$$T_{pc} = -122.6 + 6.126P - 0.1657P^2 + 0.01773P^{2.5} - 0.0005608P^3 . \quad (4.8)$$

Table 4.1: Small Temperature Difference Experimental Conditions

Test No.	p_h	T_{pseudo}	C_{p_pseudo}	$\dot{m}_h$	T_{h_in}	T_{h_out}	$T_{h\_in} - T_{h\_out}$
	MPa	^oC	J/g·K	kg/hr	^oC	^oC	^oC
SD1	7.988	34.57	11.26	248.53	33.87	33.00	0.875
SD2	7.987	34.56	24.79	248.27	35.05	34.01	1.043
SD3	8.011	34.70	27.56	252.01	35.31	34.25	1.059
SD4	8.005	34.67	34.93	248.62	35.56	34.68	0.876
SD5	7.996	34.61	27.46	248.20	35.94	35.06	0.874
SD6	8.013	34.71	19.51	249.73	36.83	35.54	1.287
SD7	8.007	34.67	15.24	247.68	37.30	35.87	1.436
SD8	8.005	34.66	9.12	250.49	38.48	37.03	1.454
SD9	8.005	34.66	6.88	250.39	39.43	38.01	1.336

Figure 4.3 shows the relation between the outlet temperature and specific heat to the pseudocritical values given in Table 4.1. Figure 4.4 shows the calculated heat transfer coefficients along with the specific heat values calculated by NIST [47].

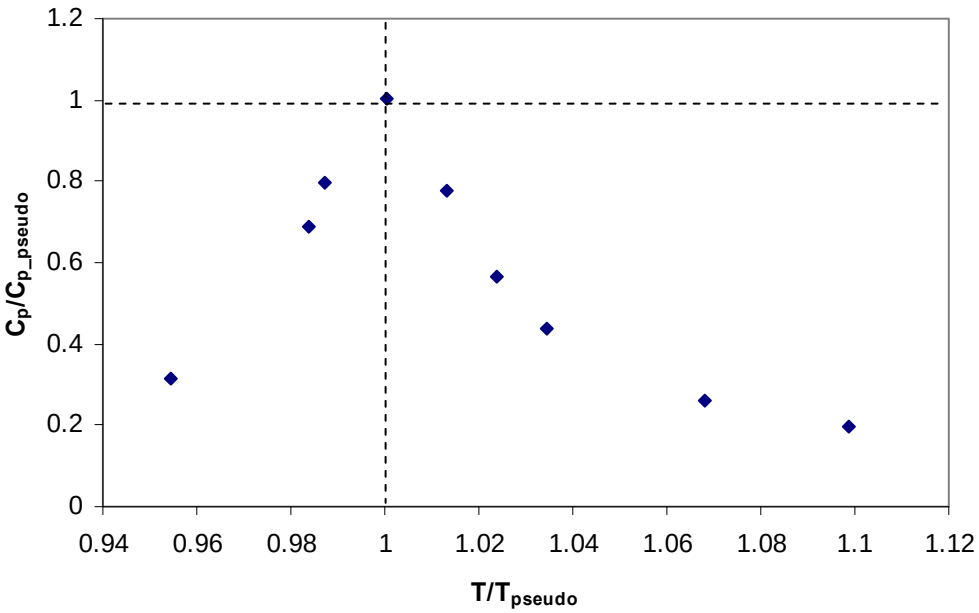

Figure 4.3: Relation Between Outlet Temperature and Specific Heat to Pseudocritical Values at 8.0 MPa

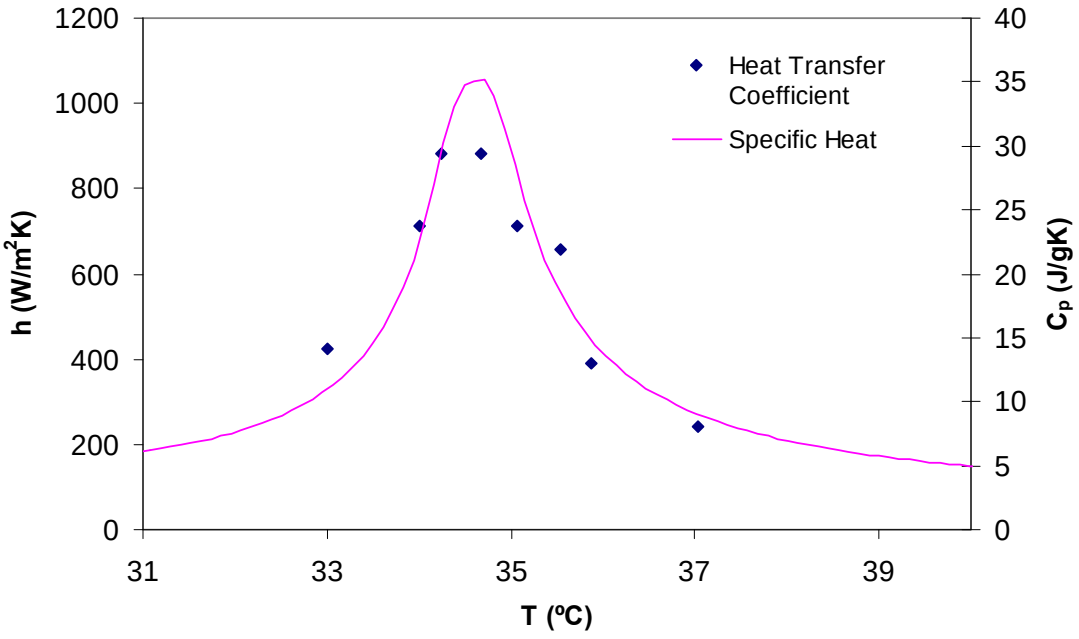

Figure 4.4: Heat Transfer Coefficient and Specific Heat for Small Temperature Difference Testing at 8.0 MPa

Figure 4.4 shows that the small temperature testing heat transfer coefficients are strongly correlated with specific heat. The heat transfer coefficient reaches a peak near the pseudocritical temperature and decreases at temperatures further from the pseudocritical point. This is in agreement with the results of Song [33] in the ANL PCHE at pressures of 7.5 and 8.5 MPa. This also agrees with trends in open literature from Liao et al. [34] and Huai et al. [43]. Similar trends have also been observed in supercritical water [48]. These results indicate that a power conversion cycle operated near the pseudocritical region of a fluid should have the ability to transfer a large amount of heat with a small temperature difference.

4.4 Large Temperature Difference Testing Based on STAR-LM Precooler Conditions

The Secure Transportable Autonomous Reactor – Liquid Metal (STAR-LM) was designed by ANL to use a S-CO_2 Brayton power conversion cycle to increase overall plant efficiency. The envisioned S-CO_2 Brayton power conversion cycle is designed to take advantage of the increase in heat transfer coefficient near the pseudocritical region noted in the Section 4.3. The system is also designed to take advantage of the decreased compression work required to circulate a higher density fluid, taking advantage of the rapid increase in density with decreasing temperature near the pseudocritical point. Both the increase in heat transfer coefficient and the decrease in required compression work are anticipated to increase the overall operating efficiency of the reactor plant. One of the primary components in this cycle is the precooler, where heat is exchanged between S-CO_2 and water. The overall cycle efficiency of the STAR-LM system is closely tied to the operating efficiency of the precooler. Figure 4.5 shows the optimum temperatures and pressures of the S-CO_2 Brayton cycle as determined by Moisseytsev [7]. The precooler as well as its outlet temperature and pressure are indicated.

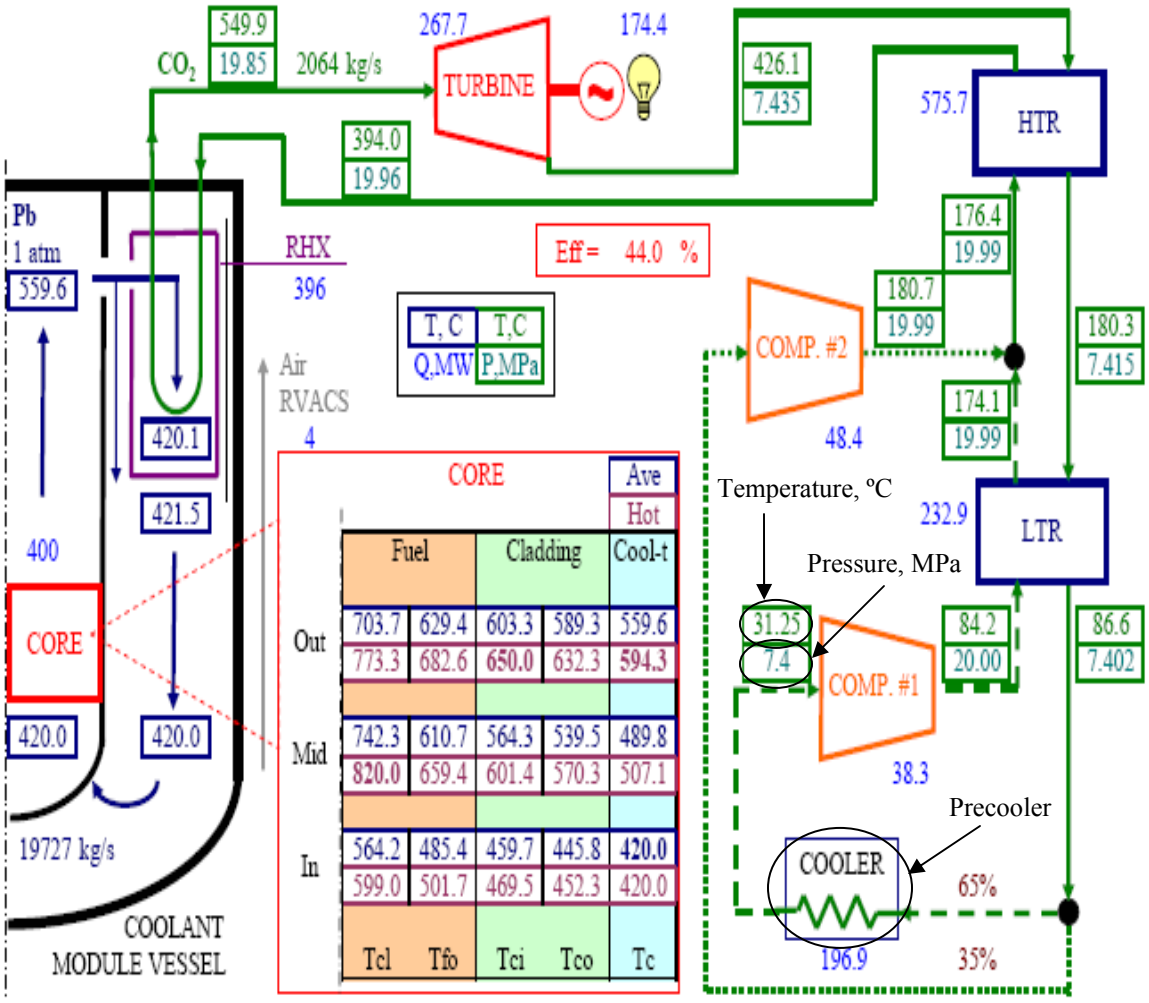

Figure 4.5: Design Conditions for STAR-LM Reactor System [7]

Moisseytsev examined nine different types of heat exchangers:

1. Stacked U-Tubes
2. U-Tubes
3. Concentric Tubes
4. Straight Tubes
5. Straight Annuli
6. Helical Coil
7. Plate-Type
8. Counter-Flow
9. PCHE

He concluded that the Heatric PCHE offers the best alternative for the precooler, Low Temperature Recuperator (LTR), and High Temperature Recuperator (HTR) based on plant economics, size, and complexity. His work identified the optimum S-CO_2 operating pressure for the precooler to be 7.4 MPa, with S-CO_2 inlet and outlet temperatures of 85.7 ºC and 31.25 ºC. Figure 4.6 shows the precooler operating range along with the density and specific heat of S-CO_2 for this temperature range at a pressure of 7.4 MPa. Figure 4.6 uses a discontinuous scale to show greater detail near the pseudocritical temperature.

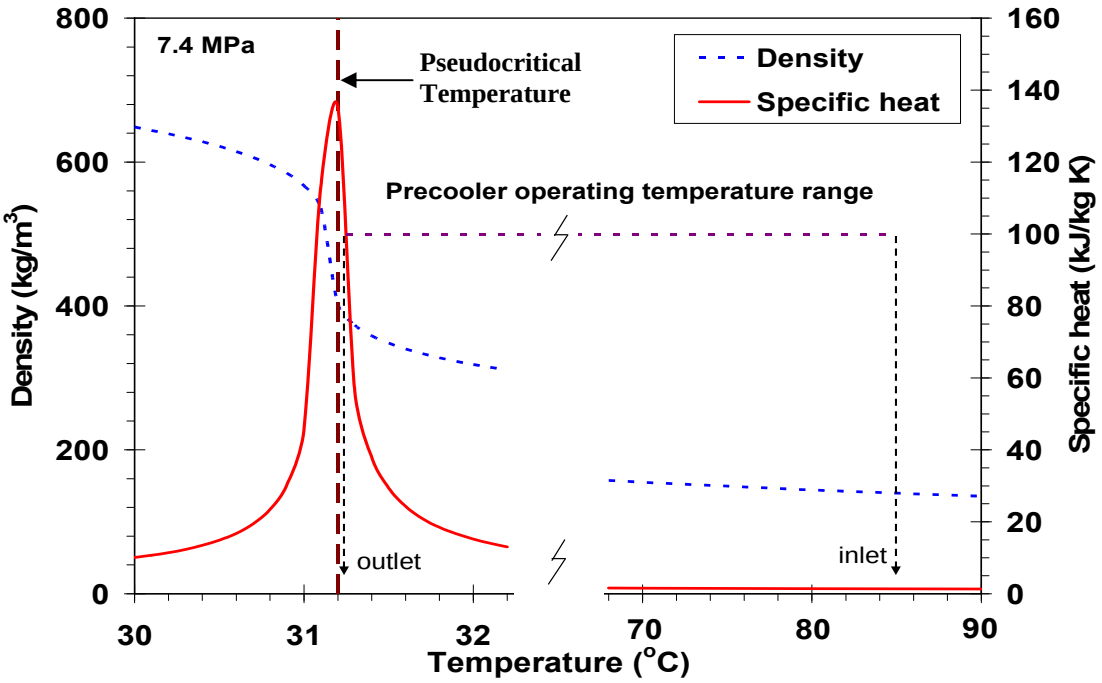

Figure 4.6: Precooler Operating Range [7]

Large temperature difference testing in the ANL PCHE at pressures of 8.0 and 9.0 MPa was conducted based on the conditions shown in Figure 4.6. The S-CO_2 outlet temperature was set near the pseudocritical temperature at 8.0 and 9.0 MPa with the inlet temperature held constant at 88 ºC. Two other temperatures slightly above the pseudocritical temperature were selected for testing at 8.0 and 9.0 MPa. The goal of these tests was to examine the effect of the peak in specific heat near the pseudocritical point on overall heat transfer in the ANL PCHE. Table 4.2 shows the nominal outlet

temperatures tested at 8.0 and 9.0 MPa. Figure 4.7 shows the specific heat of CO_2 versus temperature at 8.0 and 9.0 MPa along with the temperatures selected for testing.

Table 4.2: Testing Parameters for 8.0 and 9.0 MPa

Test Set	Pressure (MPa)	Outlet Temperature (ºC)		
B	8.0	34.7	36.0	38.0
C	9.0	40.0	43.0	46.0

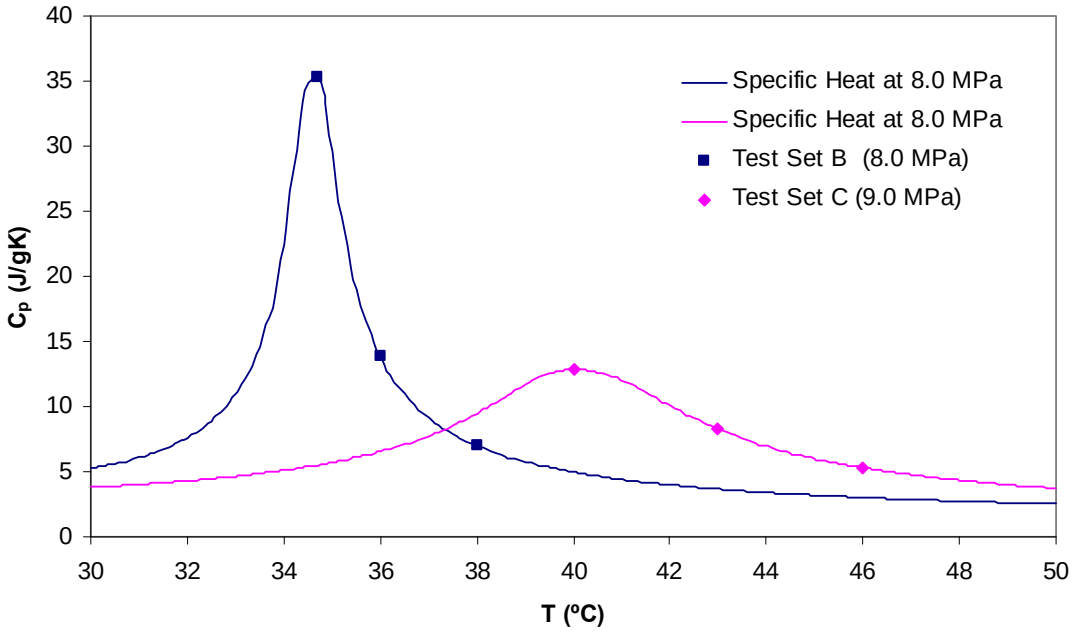

Figure 4.7: CO_2 Specific Heat and Testing Temperatures at 8.0 and 9.0 MPa

For these tests, the S-CO_2 inlet temperature was held constant at 88 ºC with flow rates of 100, 200, 300, 400, and 500 kg/hr. The water flow rate was set to 700 kg/hr with water inlet temperatures varied to achieve the desired S-CO_2 outlet temperature. At 9.0 MPa, one data set was taken with a S-CO_2 outlet temperature of 40 ºC with a water flow rate of 700 kg/hr to allow comparison between heat transfer coefficients at different pressures. Data sets were also taken at temperatures of 43 and 46 ºC with the water flow rate lowered to 600 kg/hr. This was done because the water heater was not able to reach

a high enough water inlet temperature to allow the desired S-CO_2 outlet temperature to be achieved with a flow rate of 700 kg/hr. These sets of tests were called Tests B and C for pressures of 8.0 and 9.0 MPa, respectively. Experimental conditions for Tests B and C are shown in Appendix A. Figure 4.8 shows the relation between the outlet temperature and specific heat to the pseudocritical values for Test Set B. As can be seen from Figure 4.8, a small change in temperature away from the pseudocritical temperature leads to a dramatic drop in the specific heat value compared to the pseudocritical value. This implies that system temperatures must be tightly controlled in order to keep the S-CO_2 outlet temperature in a region of significantly increased specific heat.

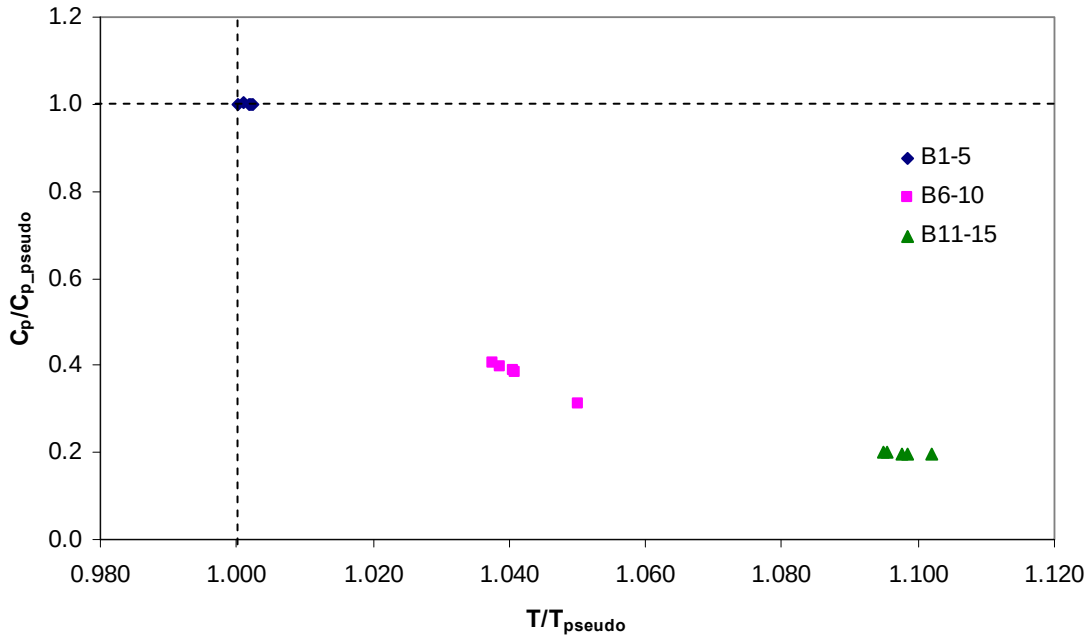

Figure 4.8: Relation Between Temperature and Specific Heat at PCHE Outlet to Pseudocritical Values at 8.0 MPa

The goal of these tests was to determine the effect of S-CO_2 outlet temperature variation on overall heat transfer in the STAR-LM precooler temperature range. Figure 4.9 shows the S-CO_2 side heat transfer coefficient versus Reynolds number for a pressure of 8.0 MPa. Figure 4.10 shows the S-CO_2 side heat transfer coefficient versus Reynolds number for a pressure of 9.0 MPa with outlet temperatures of 43 and 46 ºC. The

experimental uncertainty in the heat transfer coefficients at 8.0 and 9.0 MPa is calculated to be ±3%. These error bars are shown in Figures 4.9 and 4.10.

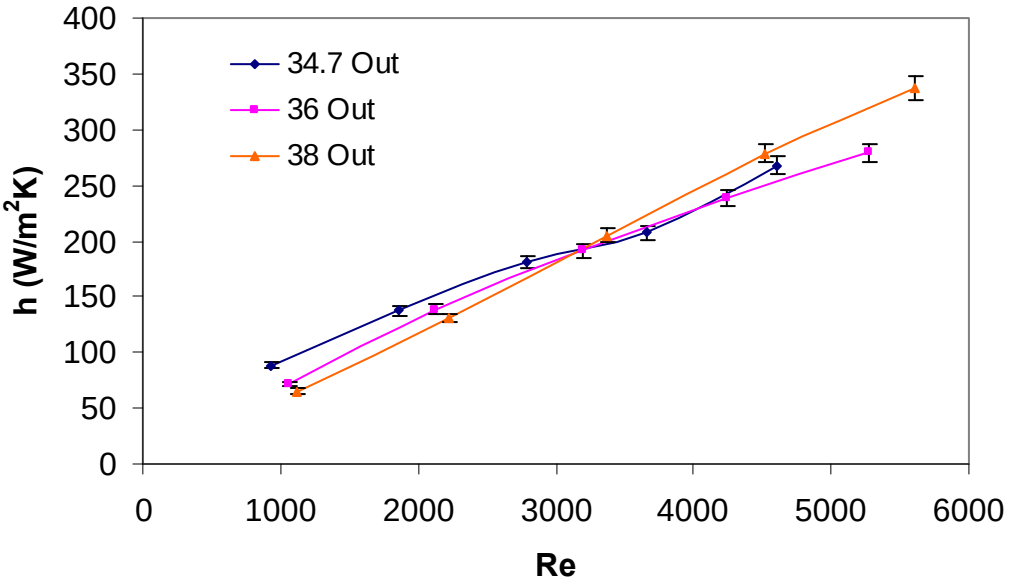

Figure 4.9: Heat Transfer Coefficient versus Reynolds Number at 8.0 MPa

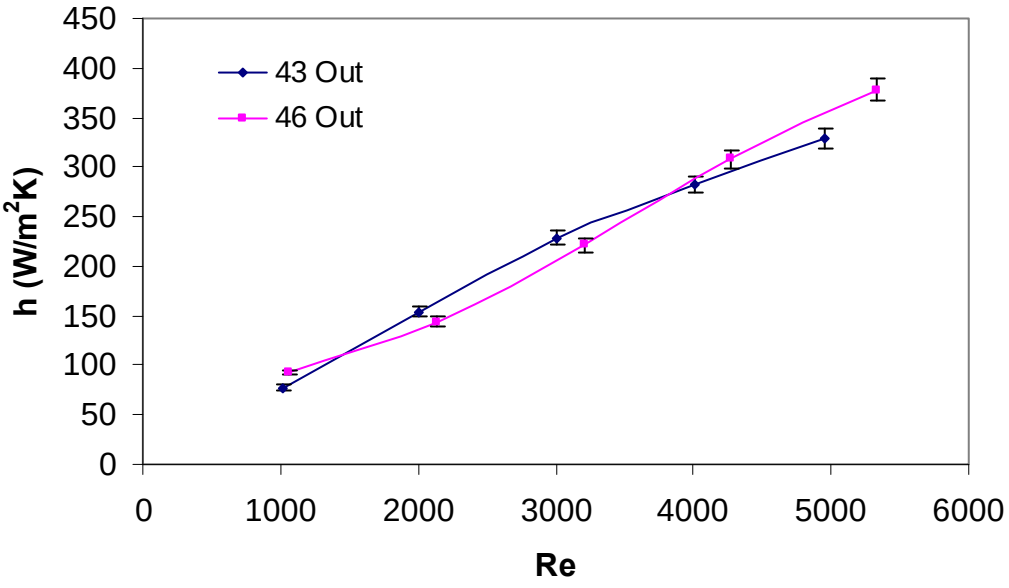

Figure 4.10: Heat Transfer Coefficient versus Reynolds Number at 9.0 MPa

As can be seen from Figures 4.9 and 4.10, there is not a significant increase in the heat transfer coefficient with a large temperature difference in the ANL PCHE at pressures of 8.0 and 9.0 MPa due to the varied outlet temperature conditions. This is in agreement with the results of Song [33] at a pressure of 7.5 MPa. These results indicate that a small variation in temperature away from the pseudocritical point at the ANL PCHE outlet does not lead to a notable decrease in S-CO_2 side heat transfer coefficient.

The effect of mass flow rate on S-CO_2 heat transfer coefficient was also examined. Figures 4.11 and 4.12 show the S-CO_2 heat transfer coefficient versus Reynolds number, along with a linear correlation, for pressures of 8.0 and 9.0 MPa.

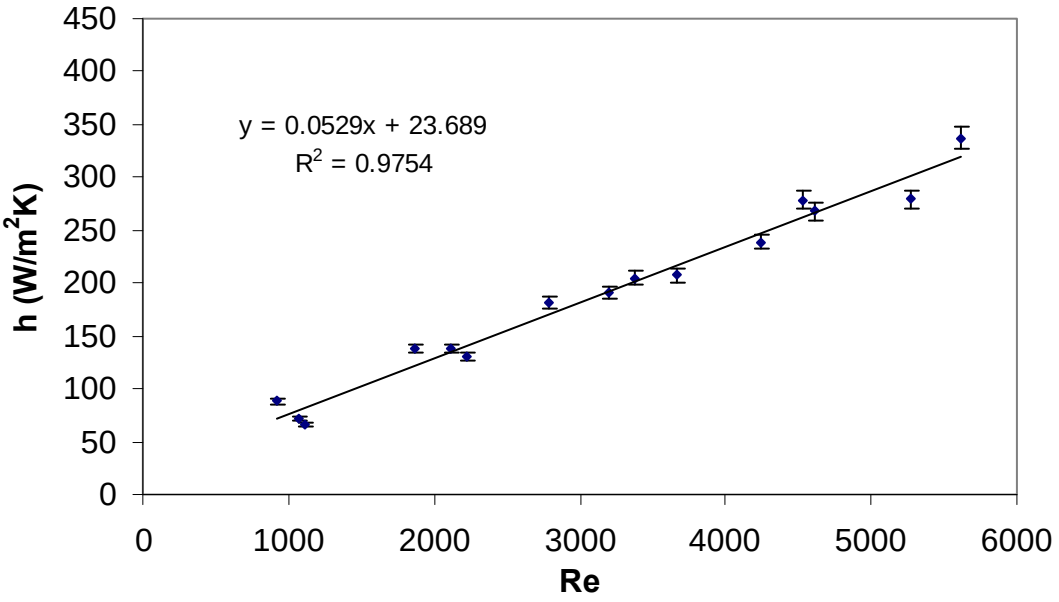

Figure 4.11: S-CO_2 Heat Transfer Coefficient at 8.0 MPa

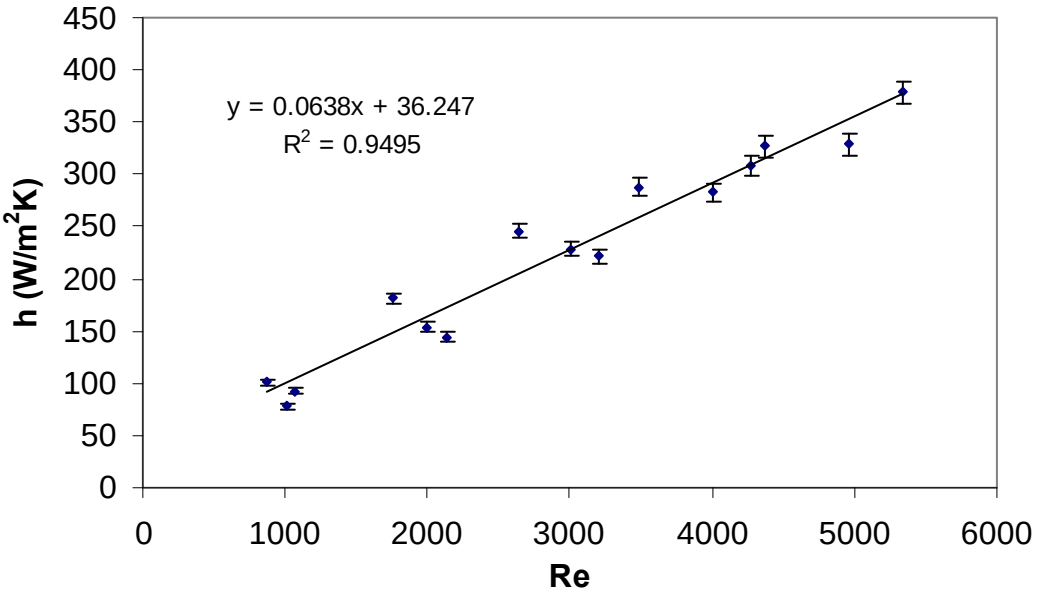

Figure 4.12: S-CO_2 Heat Transfer Coefficient at 9.0 MPa

Figures 4.11 and 4.12 show that the S-CO_2 heat transfer coefficient for a given pressure can be predicted using a linear correlation with Reynolds number. Figure 4.12 shows larger scatter because the tests with an outlet temperature of 40 ºC had a water flow rate of 700 kg/hr while the tests with an outlet temperature of 43 and 46 ºC had a flow rate of 600 kg/hr. The larger water flow rate in the 40 ºC outlet case led to higher S-CO_2 heat transfer coefficients. Ishizuka et al. [15] also noted that heat transfer coefficients were linearly related to Reynolds number in the TiTech PCHE.

Figure 4.13 shows a comparison of the S-CO_2 heat transfer coefficients at 8.0 and 9.0 MPa. Figure 4.13 shows that the heat transfer coefficients are larger for a pressure of 9.0 MPa than 8.0 MPa.

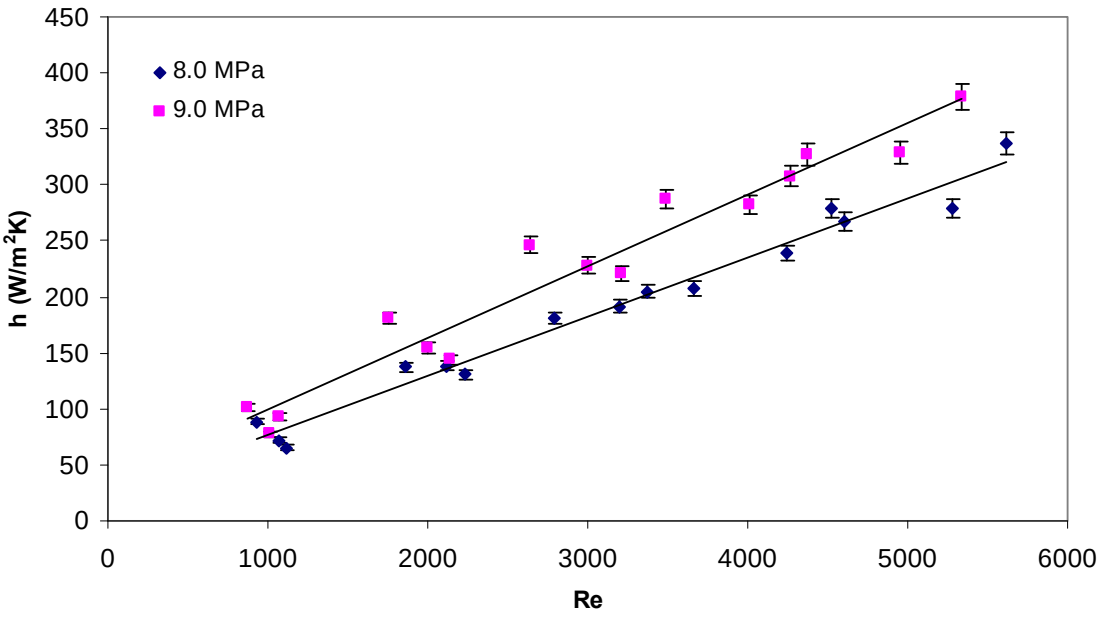

Figure 4.13: Comparison of Heat Transfer Coefficients at 8.0 and 9.0 MPa

Figure 4.14 shows data from Song [33] at pressures of 7.5 and 8.5 MPa along with data from this work at 8.0 and 9.0 MPa to show the effects of increased pressure on heat transfer coefficients in the ANL PCHE. Each set of data shown in Figure 4.14 has similar water-side and S-CO_2 inlet temperature conditions, with the S-CO_2 outlet temperature set near the pseudocritical temperature at each pressure tested. The error bars shown in Figure 4.14 for data from Song at 7.5 and 8.5 MPa are ±8%. The primary difference in the error bars shown in Figure 4.14 was the installation of a more accurate water side flow meter (0.5% versus 2%) between testing by Song and the testing presented in this work.

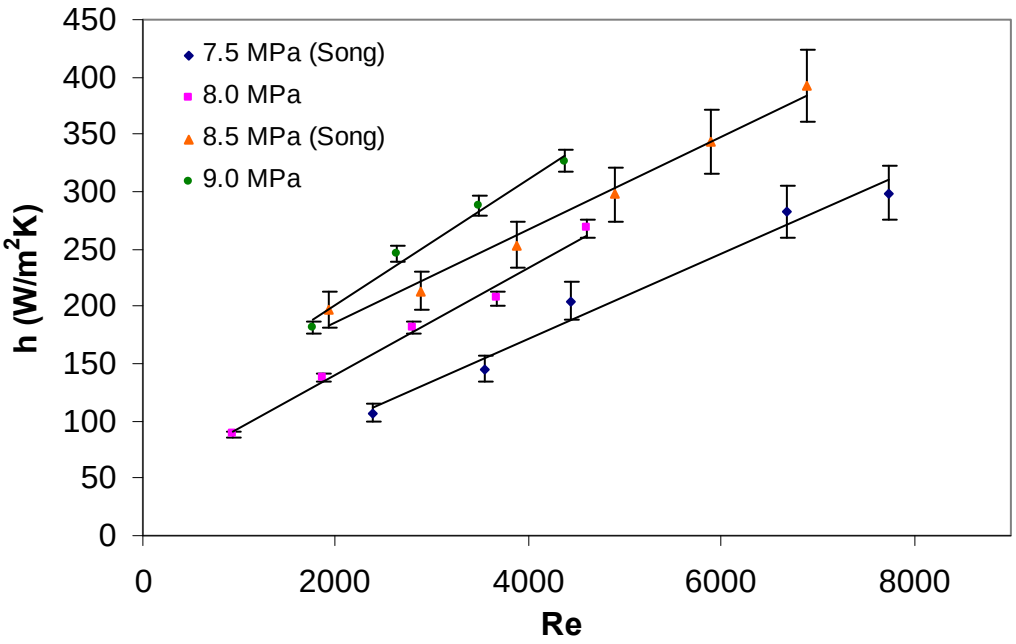

Figure 4.14: Heat Transfer Coefficients at 7.5, 8.0, 8.5, and 9.0 MPa

It can be seen from Figure 4.14 that the heat transfer coefficient for a given Reynolds number is higher at pressures further above the critical pressure of 7.377 MPa. The previous results noted that the peak in specific heat near the pseudocritical point has little influence on heat transfer coefficients inside the PCHE. At pressures above the critical pressure, the peak in specific heat decreases in magnitude while also spreading over a larger temperature range. Thus, for a pressure of 8.0 MPa, the average value of specific heat throughout the tested range is larger than that at 7.5 MPa. This can be seen in Figure 4.14, which shows the variation in specific heat with temperature for pressures of 7.5, 8.0, 8.5, and 9.0 MPa. The larger average value of specific heat at higher pressure leads to a higher S-CO_2 side heat transfer coefficient.

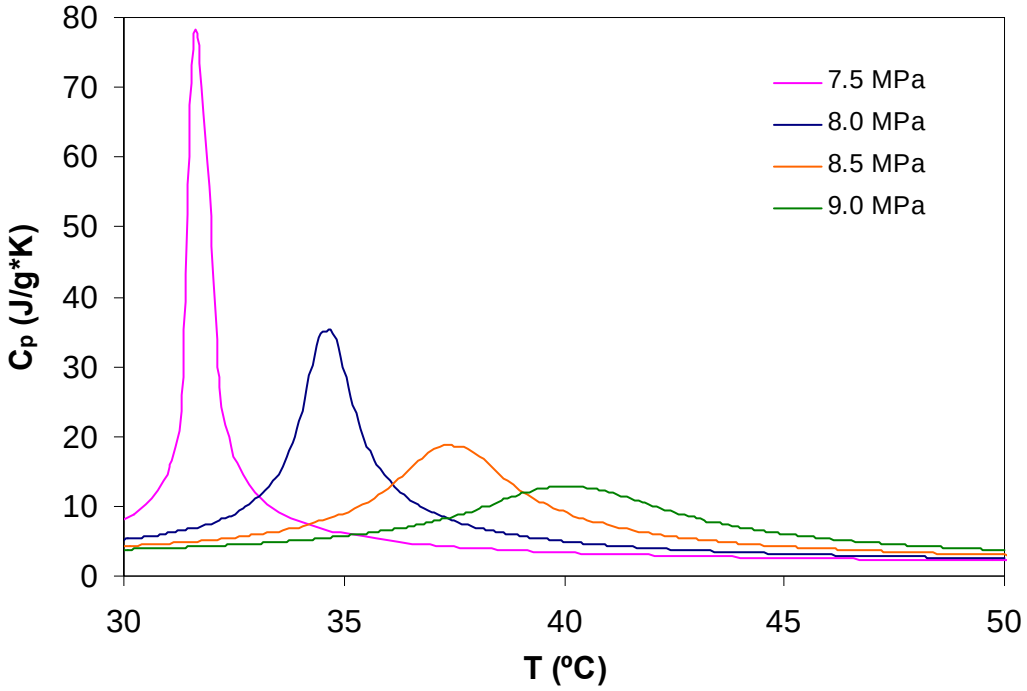

Figure 4.14: Specific Heat versus Temperature

From the data presented in this chapter, the temperatures and pressures determined through Moisseytsev's system modeling efforts as ideal for the STAR-LM system are not verified experimentally to yield the highest S-CO_2 side heat transfer coefficients in the ANL PCHE. It appears that the system would operate with higher thermal efficiency if the pressure were increased beyond the 7.4 MPa value quoted. Further, maintaining the S-CO_2 side outlet temperature near the pseudocritical temperature does not yield significant increases in heat transfer properties. This could be beneficial in overall plant design because highly accurate temperature measurement and control may not be required in order to achieve the desired heat transfer conditions.

The precooler outlet conditions were determined numerically to provide benefits in both heat transfer in the precooler and reduced compression work required by the Compressor #1 shown in Figure 4.5. This work shows that there is no significant heat transfer benefit in the PCHE when it is operated near the pseudocritical point. However, the dramatic increase in density near the pseudocritical point was also thought to decrease the required compression power needed for the system, reducing the budget required to

operate the plant. This increase in density becomes less pronounced at pressures further above the critical pressure, similar to specific heat trends seen in Figure 4.14. Figure 4.15 shows the variation of density with temperature for pressures of 7.5, 8.0, 8.5, and 9.0 MPa.

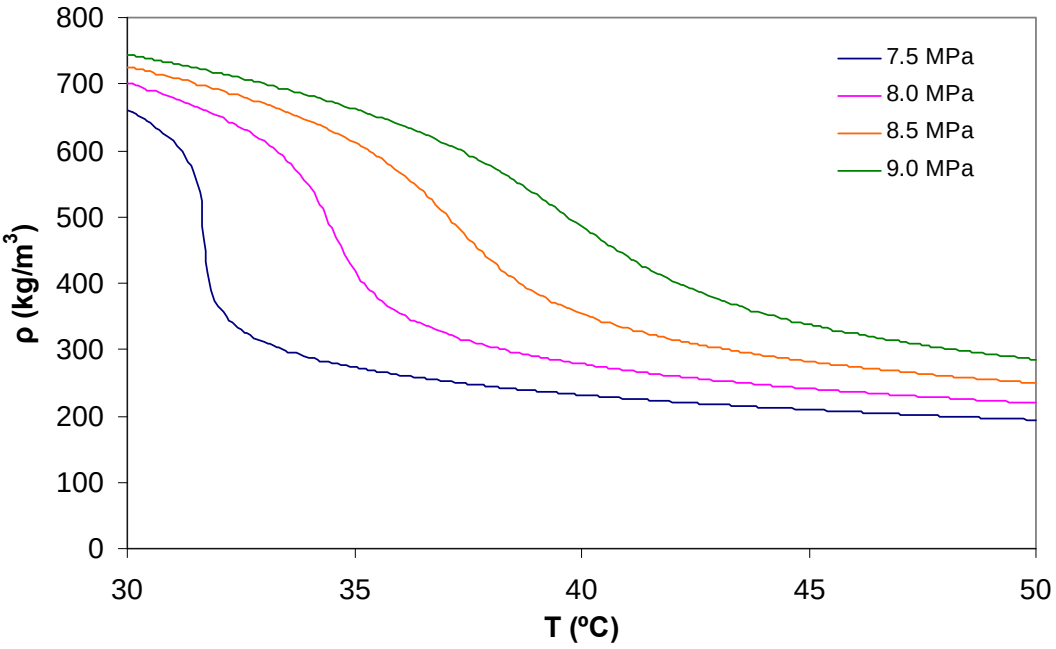

Figure 4.15: Density versus Temperature [47]

The ANL PCHE experimental system was not configured to measure the power required to circulate S-CO_2 in the experimental loop. Also, a mechanical gear pump was used for circulation, while a compressor will be used in the STAR-LM system. Further studies need to be conducted to examine the effect of varying S-CO_2 density on compression work under conditions relevant to the STAR-LM system. This will allow for better determination of the precooler outlet conditions that lead to the highest overall cycle efficiency.

CHAPTER 5 – FLUENT Simulations

5.1 FLUENT Theoretical Background

The commercially available software FLUENT was used to simulate fluid flow and heat transfer inside the PCHE. FLUENT solvers use the finite volume method to represent and evaluate partial differential equations as algebraic equations. The full computational domain is discretized onto finite sets of control volumes or cells. The general conservation equations for mass, momentum, and energy are solved numerically for these sets of control volumes. These equations are presented in tensor form. This section makes frequent use of the FLUENT User's Manual [49].

5.1.1 Conservation of Mass

The general continuity, or conservation of mass, equation used by FLUENT is

$$\frac{\partial \rho}{\partial t} + \frac{\partial (\rho u_i)}{\partial x_i} = S_m, \tag{5.1}$$

where

ρ = Density

u_i = Velocity in direction *i*

S_m = Volumetric mass source term.

The cases simulated here are steady state with no source terms. For these cases, the fluid density varies only with temperature, and is constant with respect to position. Thus, Equation 5.1 reduces to

$$\frac{\partial (\rho u_i)}{\partial x_i} = 0. \tag{5.2}$$

5.1.2 Conservation of Momentum

The inertial (non-accelerating) reference frame conservation of momentum equation used by FLUENT is

$$\frac{\partial(\rho u_i)}{\partial t}+\frac{\partial(\rho u_i u_j)}{\partial x_j}=-\frac{\partial P}{\partial x_i}+\frac{\partial}{\partial x_j}\left[\mu\left(\frac{\partial u_i}{\partial x_j}+\frac{\partial u_j}{\partial x_i}-\frac{2}{3}\partial_{ij}\frac{\partial u_k}{\partial x_k}\right)\right]+F_i, \tag{5.4}$$

where

P = Static pressure

μ = Molecular viscosity

F_i = External body force

∂_{ij} = Kronecker delta.

For steady state conditions where no body forces are present and the fluid density and viscosity are not position dependent, Equation 5.3 reduces to

$$\rho\frac{\partial(u_i u_j)}{\partial x_j}=-\frac{\partial P}{\partial x_i}+\mu\frac{\partial}{\partial x_j}\left(\frac{\partial u_i}{\partial x_j}+\frac{\partial u_j}{\partial x_i}-\frac{2}{3}\partial_{ij}\frac{\partial u_k}{\partial x_k}\right). \tag{5.6}$$

5.1.3 Energy Equation – Fluid Region

To analyze heat transfer in fluids, FLUENT solves the energy equation in the form

$$\frac{\partial(\rho E)}{\partial t}+\frac{\partial}{\partial x_i}[u_i(\rho E+P)]=\frac{\partial}{\partial x_i}\left[k_{eff}\frac{\partial T}{\partial x_i}-\sum_j h_j J_{ji}+\left(\bar{\bar{\tau}}_{eff}\cdot u_i\right)\right]+S_h, \tag{5.7}$$

where k_{eff} is the summation of the fluid thermal conductivity, k, and the turbulent thermal conductivity, k_t, which is defined by the turbulence model in use. The first three terms on the right hand side of Equation 5.6 represent energy transfer due to conduction, species diffusion, and viscous dissipation. The term S_h represents volumetric heat sources defined in the system. J_{ji} is the diffusion flux of species j. The fluid flows in these simulations contain only one species. Therefore, the value of J_{ji} is zero in these cases. In Equation 5.6,

$$E = h - \frac{P}{\rho} + \frac{v^2}{2}, \tag{5.7}$$

where v is the velocity magnitude and

$$h = \int_{298.15K}^{T} c_p dT . \tag{5.8}$$

The third term on the right side of Equation 5.6 represents the viscous dissipation term, which describes the thermal energy created by viscous shear in the fluid flow. Viscous dissipation is characterized by the Brinkman number. The Brinkman number is defined as

$$Br = \frac{\mu U^2}{k\Delta T}, \tag{5.9}$$

where

μ = Molecular viscosity

U = Fluid velocity

k = Thermal conductivity.

For Brinkman numbers approaching or greater than one, viscous dissipation effects become important. Brinkman numbers for the experiments conducted were on the order of 10^{-4}. Therefore viscous dissipation effects are neglected in the FLUENT analysis.

For the experimental conditions simulated here the fluid energy equation reduces to

$$\frac{\partial}{\partial x_i}\left[u_i(\rho E + P)\right] = \frac{\partial}{\partial x_i}\left[(k + k_t)\frac{\partial T}{\partial x_i}\right]. \tag{5.10}$$

5.1.4 Energy Equation – Solid Region

$$\frac{\partial(\rho h)}{\partial t} + \frac{\partial(u_i \rho h)}{\partial x_i} = \frac{\partial}{\partial x_i}\left(k\frac{\partial T}{\partial x_i}\right) + S_h, \tag{5.11}$$

where

ρ = Density

h = Sensible enthalpy, $\int_{298.15K}^{T} c_P dT$

u_i = Solid rotational or translational motion

S_h = Volumetric heat source.

For steady state conditions, no volumetric heat sources, a stationary solid body, and position independent thermal conductivity, Equation 5.11 reduces to

$$\frac{\partial}{\partial x_i}\left(k\frac{\partial T}{\partial x_i}\right)=0\,. \tag{5.12}$$

5.1.5 Renormalization-Group (RNG) k-ε Turbulence Model

Complete solutions to the Navier-Stokes equations for turbulent flows in complex geometries down to the smallest motion scales are not currently attainable. The Reynolds-averaging method is one way to manage the Navier-Stokes equations so that small scale turbulent fluctuations do not have to be directly simulated. The Reynolds-Averaged Navier-Stokes (RANS) equations govern the transport of the average flow quantities, modeling the full range of turbulent scales. This method introduces additional terms into the governing equations. These additional terms need to be modeled to achieve closure of the unknowns. The Renormalization-Group (RNG) *k-ε* turbulence model is used in these simulations because RNG theory accounts for low Reynolds number effects through an analytically-derived differential formula for effective viscosity.

Reynolds averaging decomposes the solution variables of the exact Navier-Stokes into mean and fluctuating components. For velocity in tensor notation (i = x, y, z for Cartesian coordinates), this is represented as

$$u_i=\bar{u}_i+u_i'\,. \tag{5.13}$$

where $\bar{u}_i$ is the mean velocity and u_i' is the fluctuating velocity. Scalar quantities such as pressure and energy are treated similarly.

The Reynolds averaged conservation of mass and momentum equations for the steady state cases simulated here are given by

$$\frac{\partial}{\partial x_i}\left(\rho\bar{u}_i\right)=0 \tag{5.14}$$

and

$$\rho\frac{\partial\left(\bar{u}_i\bar{u}_j\right)}{\partial x_j}=-\frac{\partial P}{\partial x_i}+\mu\frac{\partial}{\partial x_j}\left(\frac{\partial\bar{u}_i}{\partial x_j}+\frac{\partial\bar{u}_j}{\partial x_i}-\frac{2}{3}\partial_{ij}\frac{\partial\bar{u}_k}{\partial x_k}\right)+\frac{\partial}{\partial x_j}\left(-\rho\overline{u_i'u_j'}\right). \tag{5.15}$$

The last term on the right side of Equation 5.15 is modeled using the Boussinesq hypothesis to relate Reynolds stresses to mean velocity gradients and is given by

$$-\rho\overline{u_i'u_j'}=\mu_t\left(\frac{\partial u_i}{\partial x_j}+\frac{\partial u_j}{\partial x_x}\right)-\frac{2}{3}\left(\rho k+\mu_t\frac{\partial u_k}{\partial x_k}\right)\partial_{ij}, \tag{5.16}$$

where μ_t is the turbulent viscosity.

The RNG *k-ε* turbulence model requires two additional equations to account for the turbulent kinetic energy *k* and its dissipation rate *ε*. For steady state conditions with no source terms these are given by

$$\frac{\partial}{\partial x_i}\left(\rho k u_i\right)=\frac{\partial}{\partial x_j}\left(\alpha_k\mu_{eff}\frac{\partial k}{\partial x_j}\right)+G_k+G_b-\rho\varepsilon \tag{5.17}$$

and

$$\frac{\partial}{\partial x_i}\left(\rho\varepsilon u_i\right)=\frac{\partial}{\partial x_j}\left(\alpha_\varepsilon\mu_{eff}\frac{\partial\varepsilon}{\partial x_j}\right)+C_{1\varepsilon}\frac{\varepsilon}{k}\left(G_k+C_{3\varepsilon}G_b\right)-C_{2\varepsilon}^{*}\rho\frac{\varepsilon^2}{k} \tag{5.18}$$

The turbulent viscosity is given by a differential equation developed from RNG theory. This equation is integrated to accurately describe the effective turbulent transport variation with effective Reynolds number and allows the model to better handle low Reynolds number flows. The equation used by FLUENT for turbulent viscosity is

$$d\left(\frac{\rho^2 k}{\sqrt{\varepsilon\mu}}\right)=1.72\frac{\hat{v}}{\sqrt{\hat{v}^3-1+C_v}}d\hat{v}, \tag{5.19}$$

where

$$\hat{v}=\frac{\mu_{eff}}{\mu}$$

$$C_v\approx 100.$$

The terms α_k and α_ε used in Equations 5.17 and 5.18 are inverse effective Prandtl numbers for *k* and *ε* analytically derived from RNG theory. These are defined by

$$\left|\frac{\alpha-1.3929}{\alpha_0-1.3929}\right|^{0.6321}\left|\frac{\alpha+2.3929}{\alpha_0+2.3929}\right|^{0.3679}=\frac{\mu}{\mu_{eff}}, \tag{5.20}$$

where

$\alpha_0 = 1.$

The term G_k represents the production of turbulent kinetic energy. In a manner consistent with the Boussinesq hypothesis, G_k is defined as

$$G_k = \mu_t S^2, \tag{5.21}$$

where S is the modulus of the mean rate-of-strain tensor given by

$$S = \sqrt{2S_{ij}S_{ij}}. \tag{5.22}$$

The term G_b accounts for the generation of turbulent kinetic energy due to buoyancy when both a gravity field and temperature gradient are present. G_k is defined by

$$G_b = \beta g_i \frac{\mu_t}{\mathrm{Pr}_t}\frac{\partial T}{\partial x_i}, \tag{5.23}$$

where β is the coefficient of thermal expansion defined by

$$\beta = -\frac{1}{\rho}\left(\frac{\partial \rho}{\partial T}\right)_P. \tag{5.24}$$

The term $C_{1\varepsilon}$ in Equation 5.18 is a constant derived analytically from RNG theory with a value of 1.42. $C_{2\varepsilon}^*$ is given by

$$C_{2\varepsilon}^* = C_{2\varepsilon} + \frac{C_\mu \eta^3 (1-\eta/\eta_0)}{1+\beta\eta^3}, \tag{5.25}$$

where

$C_{2\varepsilon}$=1.68

$C_\mu = 0.0845$

$\beta = 0.012$

$\eta_0 = 4.38$

$\eta = \frac{Sk}{\varepsilon}.$

The term $C_{3\varepsilon}$ describes the degree to which ε is affected by buoyancy. It is calculated through a geometric ratio of the fluid velocity components parallel and perpendicular to the gravitational vector. The parallel component is given by u and the perpendicular component is given by v. $C_{3\varepsilon}$ is then calculated through the relation

$$C_{3\varepsilon} = \tanh\left|\frac{v}{u}\right|. \tag{5.26}$$

Convective heat transfer in the RNG k-ε turbulence model is modeled using the concept of Reynolds' analogy to turbulent momentum transfer. The energy equation for steady state conditions with no sources and negligible viscous heating effects is given by

$$\frac{\partial}{\partial x_i}\left[u_i\left(\rho E + P\right)\right] = \frac{\partial}{\partial x_j}\left(k_{eff}\frac{\partial T}{\partial x_j}\right), \tag{5.26}$$

where

$$k_{eff} = \alpha c_p \mu_{eff}. \tag{5.27}$$

The value for α in Equation 5.27 is calculated using Equation 5.20 using α_0 calculated by

$$\alpha_0 = \frac{1}{\mathrm{Pr}} = \frac{k}{\mu c_p}.$$

5.2 2-Dimensional PCHE Model

A simplified 2-Dimensional model was developed by Artit Ridluan using FLUENT to simulate heat transfer experiments in the PCHE. The model consisted of two channels with S-CO_2 and two channels with water as the working fluids. As the inside geometry of the Argonne National Laboratory (ANL) PCHE was not known, the channel geometry was based on the Tokyo Institute of Technology (TiTech) PCHE [15]. While the bends in the physical heat exchanger are in a different plane than those used in this model, bends were included to enhance turbulent flow, and also heat transfer, in the 2D model. A section of the model is shown in Figure 5.1.

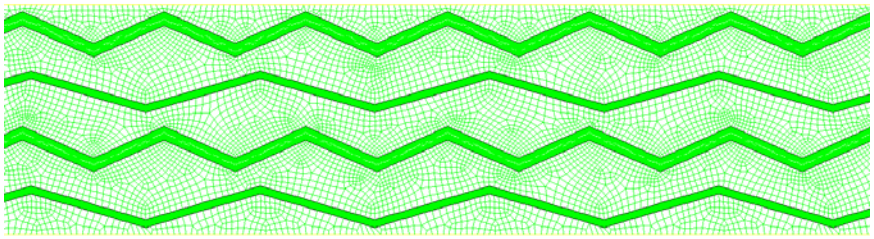

Figure 5.1: 2D PCHE Model Section

Constant property water was used in two of the model channels. The database defined FLUENT properties for steel were used for the metal walls separating the fluid channels. Curve fits for S-CO_2 properties were entered to properly account for the temperature variation of S-CO_2 properties inside the PCHE. These curve fits accounted for the changing thermophysical properties to less than 5% error for the cases presented here. However, it was not possible to accurately model the dramatic changes in thermophysical properties for the heat transfer experiments conducted with the PCHE outlet temperature set at the pseudocritical point for pressures of 8.0 and 9.0 MPa. The corresponding pseudocritical temperatures for these pressures are 34.7 and 40 ºC, respectively. Table 5.1 shows the S-CO_2 experimental conditions simulated here for pressures of 8.0 and 9.0 MPa, labeled Tests C and D. For each of these outlet temperatures, S-CO_2 mass flow rates of 100, 200, 300, 400, and 500 kg/hr were examined with an inlet temperature of 88 ºC. Water flow rates for the 8.0 and 9.0 MPa tests were 700 and 600 kg/hr, respectively, with the experimental water inlet temperatures used for simulation.

Table 5.1: Simulated Experimental Conditions

Test No.	p_h	$\dot{m}_h$	T_{h_in}	T_{h_out}	$\dot{m}_w$	T_{c_in}	T_{c_out}
	MPa	kg/hr	°C	°C	kg/hr	°C	°C
B6	8.003	100.53	88.63	36.07	701.59	35.63	40.54
B7	8.001	200.77	88.10	35.98	699.78	35.11	45.08
B8	7.972	297.14	89.36	36.20	701.80	35.05	48.89
B9	8.003	401.01	87.92	36.05	701.77	33.28	52.96
B10	7.995	500.61	87.93	35.90	700.09	31.28	56.44
B11	8.003	100.03	87.68	37.94	697.80	37.68	41.61
B12	8.005	199.73	88.85	37.97	697.80	37.53	45.66
B13	7.998	301.31	88.17	38.03	699.86	37.48	49.51
B14	8.020	404.29	88.97	38.29	701.62	37.58	53.49
B15	7.998	501.79	88.09	38.01	702.25	36.83	56.60
C5	8.998	100.48	87.51	42.91	601.65	42.64	47.50
C6	9.005	198.90	88.74	42.96	600.67	42.47	52.38
C7	9.005	299.11	88.37	42.90	600.48	42.00	56.88
C8	9.005	399.47	88.92	42.90	598.37	41.18	61.11
C9	9.004	494.92	88.11	42.84	594.21	39.78	64.50
C10	8.996	99.91	88.30	45.80	602.09	45.77	49.68
C11	9.004	200.90	88.34	45.87	603.06	45.57	53.59
C12	9.006	301.49	88.23	45.84	602.23	45.38	57.46
C13	8.994	400.09	87.14	45.86	603.21	45.24	60.87
C14	9.008	500.74	88.01	45.95	597.86	44.91	64.82

Results from the simulations were obtained from FLUENT both by calculating the average fluid temperature at 15 points along the channel length. An example temperature distribution for Test B13 using this method is shown in Figure 5.2. Temperature distributions for all 2D simulations performed are shown in Appendix E.

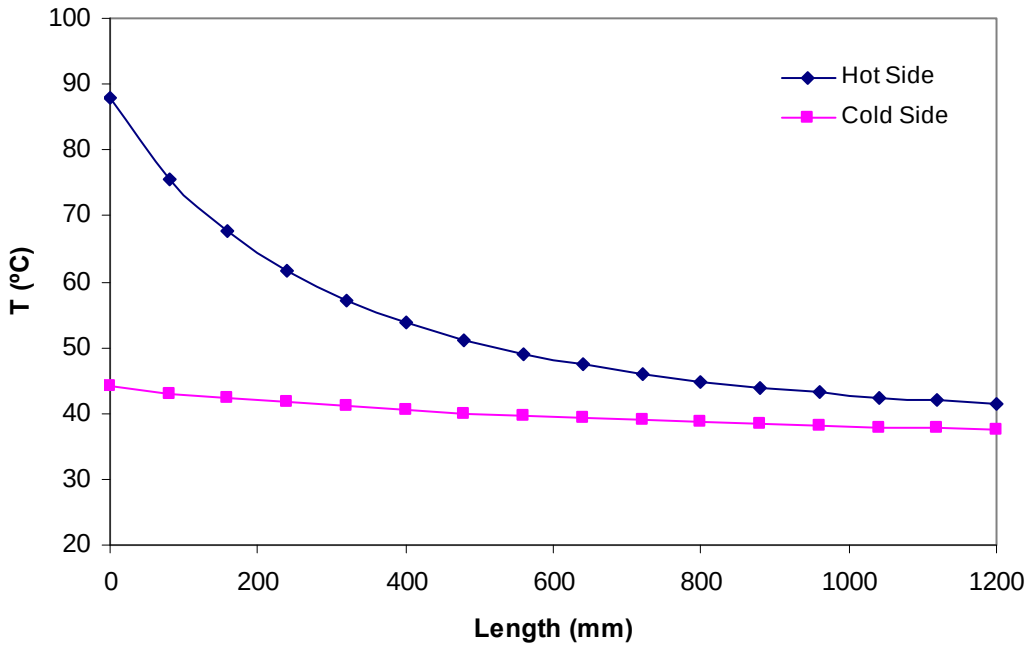

Figure 5.2: Simulated Temperature Distribution for Test B13

The experimental setup available at ANL did not allow for temperature measurements to be made at points other than the PCHE inlets and outlets. Thus, it is not possible to verify the accuracy of the temperature distributions calculated through FLUENT simulations. However, the simulated temperature distributions make physical sense with respect to typical counter-flow heat exchanger temperature distributions. This can be seen from Figure 5.2 by the fact that the fluid temperatures change most rapidly near the hot side inlet, where the temperature difference is greatest and change less rapidly as the temperature difference decreases. With the simulation inlet conditions specified to match the experimental conditions, the only experimental data available to check the accuracy of the simulations are the measured S-CO_2 and water outlet temperatures. The measured and simulated outlet temperatures are shown in Table 5.2 along with relative errors to the measured data. The relative error is defined as

$$Error = \frac{\left(T_{sim} - T_{\exp}\right)}{T_{\exp}} \times 100 . \tag{5.28}$$

Table 5.2: 2D Model Comparison of Experimental and Simulated Data

Test No.	S-CO_2				Water			
	$\dot{m}_h$	T_{exp}	T_{sim}	Error	$\dot{m}_w$	T_{exp}	T_{sim}	Error
	kg/hr	°C	°C	%	kg/hr	°C	°C	%
B6	100.53	36.07	36.47	**1.10**	701.59	40.54	38.91	**-4.03**
B7	200.77	35.98	37.83	**5.14**	699.78	45.08	40.57	**-10.00**
B8	297.14	36.20	39.77	**9.86**	701.80	48.89	42.23	**-13.63**
B9	401.01	36.05	40.63	**12.69**	701.77	52.96	41.93	**-20.83**
B10	500.61	35.90	41.38	**15.26**	700.09	56.44	41.46	**-26.55**
B11	100.03	37.94	38.10	**0.42**	697.80	41.61	40.66	**-2.29**
B12	199.73	37.97	39.50	**4.02**	697.80	45.66	42.63	**-6.65**
B13	301.31	38.03	41.38	**8.80**	699.86	49.51	44.09	**-10.94**
B14	404.29	38.29	43.37	**13.27**	701.62	53.49	45.42	**-15.09**
B15	501.79	38.01	44.79	**17.84**	702.25	56.60	45.83	**-19.04**
C5	100.48	42.91	43.32	**0.95**	601.65	47.50	46.20	**-2.73**
C6	198.90	42.96	45.12	**5.04**	600.67	52.38	48.44	**-7.52**
C7	299.11	42.90	46.89	**9.31**	600.48	56.88	49.68	**-12.65**
C8	399.47	42.90	48.51	**13.09**	598.37	61.11	50.43	**-17.47**
C9	494.92	42.84	49.50	**15.54**	594.21	64.50	50.29	**-22.03**
C10	99.91	45.80	46.08	**0.61**	602.09	49.68	48.93	**-1.50**
C11	200.90	45.87	47.45	**3.45**	603.06	53.59	50.92	**-4.98**
C12	301.49	45.84	49.25	**7.44**	602.23	57.46	52.31	**-8.96**
C13	400.09	45.86	51.03	**11.28**	603.21	60.87	53.24	**-12.54**
C14	500.74	45.95	52.70	**14.68**	597.86	64.82	54.12	**-16.51**

Table 5.2 shows that the 2D PCHE model over-predicts the S-CO_2 outlet temperature. A majority of the data falls within 15% of the experimental value. The relative error increases with S-CO_2 mass flow rate for both the 8.0 and 9.0 MPa tests conducted. The model under-predicts the water side outlet temperature. A majority of the data falls within 20% of the experimentally measured values. The absolute value of the relative error again increases with increasing S-CO_2 mass flow rate. One reason for this could be the use of constant properties for water in the simulations conducted. The water side experimental temperature difference is larger in cases with larger S-CO_2 mass

flow rate. The maximum temperature difference is approximately 20 ºC for Test C14, which has an experimental outlet temperature of 64.82 ºC. At this temperature, the difference between the thermal conductivity calculated by the National Institute of Standards (NIST) [47] and the constant property value used in the FLUENT simulations is approximately 9%. Further simulations should be conducted to examine the effect of water property variation on the 2D PCHE model accuracy.

5.3 3-Dimensional PCHE Model

A 3-Dimensional FLUENT model was developed by Artit Ridluan to simulate heat transfer in the PCHE. The model was based on dimensions presented by Ishizuka et al. of TiTech [15]. The model consisted of straight semi-circular channels with a diameter of 1.88 mm. The model used the same double-banking configuration as the TiTech PCHE, with two plates of hot channels for every plate of cold channels. A symmetry boundary at the center of the model was used to reduce computational time during simulation. Therefore only 6 channels are modeled for the top and bottom plates of hot channels, while a single plate of 5 ½ cold channels are modeled. Periodic boundaries were used at the top and bottom planes of the model to simulate channels in the center of the PCHE body. A planar cross-section of 3D model geometry is shown in Figure 5.3. Dimensions for the plate thickness and metal thickness between channels are specified.

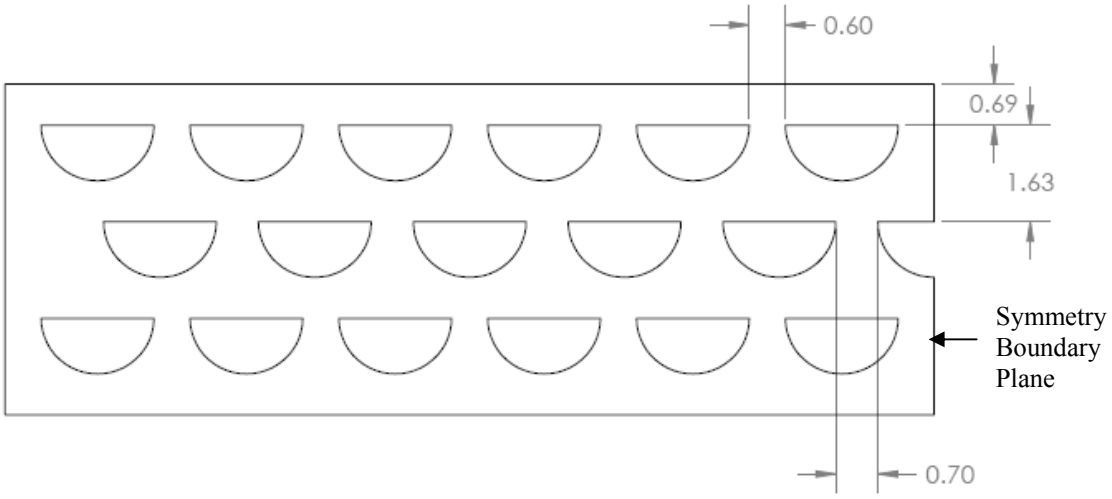

Figure 5.3: 3D Model Geometry

For the ANL PCHE cases, constant property water was used as the working fluid on the cold side. The FLUENT material database defined properties for steel were used for the solid material in the 3D model. Polynomial curve fits were used to account for the varying properties of S-CO_2 in the cases simulated. These curve fits represented the thermophysical properties calculated by NIST [47] to within 5%. The cases simulated here are the same as presented in Table 5.1 for a pressure of 8.0 MPa with S-CO_2 mass flow rates of 100, 300, and 500 kg/hr. The inlet conditions for both S-CO_2 and water were specified based on experimental conditions listed in Table 5.1.

Average temperatures were calculated by FLUENT for each of the channel outlet faces. The average outlet temperature for each of the channels was then averaged with the other channel outlets to provide a single simulated outlet temperature that is used to compare the model to experimental data. Table 5.3 shows the experimental and simulated outlet temperatures along with the relative error calculated through Equation 5.28.

Table 5.3: 3D Model Comparison of Experimental and Simulated Data

Test No.	S-CO_2				Water			
	$\dot{m}_h$	T_{exp}	T_{sim}	Error	$\dot{m}_w$	T_{exp}	T_{sim}	Error
	kg/hr	°C	°C	%	kg/hr	°C	°C	%
B6	100.53	36.07	35.85	**-0.61**	701.59	40.54	39.69	**-2.09**
B8	297.14	36.20	35.52	**-1.89**	701.80	48.89	43.80	**-10.40**
B10	500.61	35.90	36.28	**1.05**	700.09	56.44	44.97	**-20.32**
B11	100.03	37.94	37.70	**0.64**	697.80	41.61	40.53	**-2.59**
B13	301.31	38.03	38.29	**0.68**	699.86	49.51	43.90	**-11.33**
B15	501.79	38.01	39.01	**2.64**	702.25	56.60	45.20	**-20.14**

Table 5.3 shows that the 3D PCHE model based on the TiTech geometry predicts the S-CO_2 outlet temperatures of the ANL PCHE to within 3% for the cases simulated. This is more accurate than the temperatures predicted by the 2D model. The model also predicted the water side outlet temperatures to within 20%, with relative errors increasing with increasing S-CO_2 mass flow rate. Relative errors in the water outlet temperature are approximately the same for the 2D and 3D models.

This 3D PCHE model was also used to simulate experimental data presented by Ishizuka et al. of TiTech [15]. The experiments conducted by TiTech used CO_2 on both the hot and cold sides of the heat exchanger. All cases presented by TiTech used CO_2 in the vapor phase on the hot side. The cold side conditions were supercritical in some cases and in the vapor phase for others. However, all cases were carried out under temperature conditions far from the pseudocritical point, where the thermophysical properties change gradually with temperature. This allowed for more accurate modeling of the properties. In general, there was less than 0.5% error between the polynomial curve fits used and the property values calculated by NIST [47]. Table 5.4 shows the comparison experimental data from TiTech and simulations using the 3D model, along with relative error calculated using Equation 5.28.

Table 5.4: 3D Model Comparison with TiTech Data

Test	$\dot{m}$	Hot Side				Cold Side			
		P_h	T_{exp}	T_{sim}	Error	P_h	T_{exp}	T_{sim}	Error
	kg/hr	MPa	ºC	ºC	%	MPa	ºC	ºC	%
609.1	42.8	2.26	280.1	113.1	**1.16**	6.59	260.7	245.5	**-5.83**
609.2	52.6	2.22	280.2	114.1	**1.99**	6.53	260.9	244.5	**-6.28**
611.1	79.6	2.50	279.9	111.5	**-0.10**	7.34	259.9	239.3	**-7.94**
611.2	66.2	2.50	279.7	113.5	**1.83**	7.38	260.4	248.3	**-4.66**
611.3	55.9	2.48	279.8	114.1	**2.33**	7.47	260.9	247.8	**-5.04**
611.4	45.3	2.56	279.6	113.4	**1.65**	7.45	261.6	248.3	**-5.07**
611.5	33.5	2.49	279.8	113.5	**1.80**	7.44	262.3	248.1	**-5.43**
614.1	74.9	2.54	279.9	112.6	**2.10**	8.35	256.0	246.2	**-3.85**
614.2	66.6	2.58	279.9	112.6	**2.17**	8.24	255.9	246.2	**-3.80**
614.3	55.6	2.56	279.9	113.3	**2.77**	8.27	256.3	245.6	**-4.17**
614.4	44.0	2.54	279.9	114.2	**3.51**	8.31	256.4	244.5	**-4.65**
616.1	83.3	2.99	280.0	116.9	**6.29**	9.48	254.9	241.5	**-5.27**
616.2	72.0	3.00	280.0	111.7	**1.53**	9.49	255.3	244.0	**-4.41**
616.3	60.7	3.05	280.1	115.0	**4.53**	9.54	255.0	243.6	**-4.49**
616.4	48.6	3.06	280.1	113.9	**3.65**	9.5	255.6	244.7	**-4.25**
617.1	87.0	3.23	280.1	111.9	**1.82**	10.09	252.8	242.6	**-4.04**
617.2	76.3	3.33	279.9	111.7	**1.64**	10.04	253.5	242.8	**-4.23**
617.3	63.8	3.31	280.0	111.2	**1.27**	10.06	253.8	243.2	**-4.17**
617.4	52.1	3.34	280.1	111.2	**1.37**	10.08	254.5	243.2	**-4.43**

Table 5.4 shows that the 3D model predicts outlet temperatures in the TiTech PCHE to within approximately 5% for both subcritical and supercritical CO_2. This is better agreement than is seen with data from the ANL PCHE. One possible explanation for this is the polynomial curve fits used for the TiTech cases were more accurate than the ones used for near critical S-CO_2 conditions. Also, accurate curve fits were used for both the hot and cold sides in simulating TiTech PCHE experimental conditions. More accurate results for the ANL PCHE may be attainable using curve fits to match water physical properties over the range of experimental temperatures instead of constant property values. Another explanation for the more accurate simulation results with this 3D model and the TiTech data is that the model used was developed using more complete

knowledge of the interior geometry than is available for the ANL PCHE. New models based on the dimensions presented in Chapter 3 of this work may yield more accurate simulation results than are possible using a 3D model based on dimensions from a different PCHE.

CHAPTER 6 – Conclusions

This work presents the experimental and numerical simulation results of the heat transfer characteristics of a Printed Circuit Heat Exchanger (PCHE) operated with Supercritical Carbon Dioxide (S-CO_2) and water as the working fluids. The experimental operating conditions examined were based on the precooler operating conditions envisioned for the Secure Transportable Autonomous Reactor – Liquid Metal (STAR-LM) reactor plant concept. The STAR-LM system utilizes a S-CO_2 Brayton power conversion cycle and the overall plant thermal efficiency is closely tied to the operating characteristics of the precooler. The heat transfer characteristics of the PCHE were examined and reported.

The PCHE used in this work was designed and manufactured by Heatric. Detailed information about the interior geometry of the PCHE was not provided. The interior geometry of the Argonne National Laboratory (ANL) PCHE was therefore estimated using the partial specifications supplied by Heatric along with information provided by the Tokyo Institute of Technology (TiTech) [15] about the directly measured interior geometry of the TiTech PCHE. Table 6.1 shows the estimated interior geometry of the ANL PCHE.

Table 6.1: Estimated ANL PCHE Dimensions

	Hot	**Cold**
Channel Diameter, mm	1.506	1.506
Channel Travel Length, mm	1230	1378
Full Bend Angle, degrees	135.8	111.6
Number of Plates	21	21
Channels per Plate	56	50
Thickness between channels, mm	0.48	0.48
Plate Thickness, mm	1.31	1.31
Sidewall Thickness	44.6	
Top and Bottom Wall Thickness, mm	32.5	

The interior channel geometry was examined using Computational Fluid Dynamics (CFD) software. Different vertical and horizontal channel pitches were simulated in combination with varying fillet radius values on the channel bends. The simulation results were compared to experimental pressure drop data for constant temperature water on both the hot and cold sides of the PCHE. A number of possible combinations of vertical pitch and fillet radius values were found to closely match the experimental pressure drop data for the PCHE channels. However, it was not possible to select a most probable internal configuration based on information provided by Heatric or inferred from the TiTech PCHE.

Heat transfer experiments were conducted with S-CO_2 and water in the PCHE using a small S-CO_2 temperature difference across the heat exchanger. The purpose of these tests was to examine the effect of S-CO_2 thermophysical property variation of near the pseudocritical point at a pressure of 8.0 MPa. S-CO_2 temperature differences in the PCHE were kept below 2 ºC. Temperatures selected for testing were based on the specific heat curve near the pseudocritical point. It was observed that the S-CO_2 side heat transfer coefficient reached a peak near the pseudocritical temperature and decreased with temperatures away from the pseudocritical temperature. It was found that the S-CO_2 heat transfer coefficient behaved in a manner similar to that of the specific heat near the pseudocritical point. Other experimenters have reported similar behavior in both S-CO_2 and supercritical water heat transfer coefficients with geometries different from the zig-zag channels used in the ANL PCHE.

The PCHE was tested in conditions similar to those proposed by Moisseytsev [7] for the precooler operating conditions in the STAR-LM system. These tests set the S-CO_2 outlet temperature in the PCHE near the pseudocritical value. Testing with outlet temperatures slightly above the pseudocritical temperature were also examined to determine the effect of rapidly varying thermophysical properties on heat transfer in the PCHE under STAR-LM relevant conditions. No significant heat transfer coefficient increases were noted for the near-pseudocritical case as opposed to temperatures slightly above the pseudocritical temperature. Thus, highly accurate S-CO_2 temperature measurement and control systems are not required to achieve the desired heat transfer conditions in the precooler.

Heat transfer experiments were conducted with pressures above those specified by Moisseytsev. The pressures tested in this work were 8.0 and 9.0 MPa. Previous testing at 7.5 and 8.5 MPa was conducted by Hoseok Song [33]. These tests showed that the S-CO_2 heat transfer coefficients were larger for pressures further from the critical pressure. These results can be explained through the specific heat variation with temperature. At pressures further from the pseudocritical point, the peak in specific heat decreases in magnitude while also spreading over a larger temperature range. The result is that the average specific heat value is larger at pressures further from the pseudocritical point. This results in a higher heat transfer coefficient. Heat transfer coefficients were observed to vary linearly with Reynolds number for a given pressure. For 8.0 MPa, this relation is given by

$$h_{S-CO_2}\left(\frac{W}{m^2K}\right) = 0.053 \times \mathrm{Re}_{S-CO2} + 23.69 . \quad (6.1)$$

For a pressure of 9.0 MPa, this relation is given by

$$h_{S-CO_2}\left(\frac{W}{m^2K}\right) = 0.064 \times \mathrm{Re}_{S-CO2} + 36.25 . \quad (6.2)$$

Heat transfer in the PCHE was modeled using FLUENT CFD software. A 4-channel, 2-dimensional, zig-zag channel was developed. Polynomial curve fits were used to characterize the temperature-dependent variation in S-CO_2 thermophysical properties. Properties calculated using these curve fits were accurate to within 5% of the values calculated by the National Institute of Standards and Technology (NIST) [47]. Water on the cold side of the PCHE was modeled as a constant property fluid. Comparison of simulation results to experimental data showed that there was a relative error of approximately 15% for the simulated S-CO_2 outlet temperatures and approximately 20% relative error for the simulated water outlet temperatures.

A 3-dimensional, straight channel PCHE model was also developed. This model was based on the measured TiTech PCHE geometry and using a double-banking system with two plates of hot channels for every one plate of cold channels. S-CO_2 property values used were accurate to within 5% of the values calculated by NIST [47]. This 3D model predicted the ANL PCHE S-CO_2 outlet temperatures to within 3% and the water outlet temperatures to within approximately 20% for the cases simulated.

Experimental conditions for $CO_2 – CO_2$ testing presented by TiTech were also simulated using this 3D model. TiTech conducted testing in regions far from the pseudocritical point of CO_2, where property variations are not as dramatic. This allowed the thermophysical properties to be calculated within 0.5% of the values given by NIST [47]. The model predicted the outlet temperatures to within 5% for both the hot and cold sides of the TiTech PCHE.

This work noted that there was no significant difference in the heat transfer behavior for precooler outlet temperatures slightly above the critical point. Future work could examine the effects of alternate precooler outlet conditions on the compression work required to circulate S-CO_2 under STAR-LM relevant conditions. Further modeling efforts could examine the effect of using temperature-dependent water properties in the FLUENT models presented in this work. Additional CFD models can be developed using the estimated ANL PCHE internal geometry shown in Chapter 3 of this work. It is probable that more accurate physical modeling of the ANL PCHE in CFD software programs will lead to simulation results that more closely match the experimentally observed values.

References

1. "The New Economics of Nuclear Power," World Nuclear Association Report. www.world-nuclear.org.

2. Nuclear Energy Institute: http://www.nei.org, 2008.

3. Babu, B.V.. "Evaluation of Existing Treatment Techniques and Various Problems Associated with Nuclear Waste Management," Energy Education Science and Technology, 14(2), pp. 93, (2005).

4. J. Sienicki, A. Moisseytsev, D. Wade, and A. Nikiforova, "Status of Development of the Small Secure Transportable Autonomous Reactor (SSTAR) for Worldwide Sustainable Nuclear Energy Supply," Proceedings of ICAPP 2007, Nice, France (2007).

5. V. Dostal, "A Supercritical Carbon Dioxide Cycle for Next Generation Nuclear Reactors," Massachusetts Institute of Technology, Doctor of Science Thesis, January 2004.

6. A. Moisseytsev, J. Sienicki, and D. Wade, "Cycle Analysis of SCO2 Gas Turbine Brayton Cycle Power Conversion System for Liquid Metal-Cooled Fast Reactors," ICONE 11, Tokyo, Japan (2003).

7. Moisseytsev, A., "Passive Load Follow Analysis of the STAR-LM and STAR-H2 Systems," Dissertation, Texas A&M December 2003.

8. A. Moisseytsev and J. Sienicki, "Transient Analysis of a Supercritical Carbon Dioxide Brayton Cycle Energy Converter Coupled to an Autonomous Lead-Cooled Fast Reactor," Proceedings of ICONE 14, Miami, Florida.

9. S. Dewson and B. Thonon, "The Development of High Efficiency Heat Exchangers for Helium Gas Cooled Reactors,"

10. D. Reay, "Compact Heat Exchangers: A Review of Current Equipment and R&D in the Field," Heat Recovery Systems and CHP, Volume 14, No. 5, pp. 459-474, 1994.

11. www.heatric.com, 2008.

12. J. J. Sienicki, A. V. Moisseytsev, D. C. Wade, M. T. Farmer, C. P. Tzanos, J. A. Stillman, J. W. Holland, P. V. Petkov, I. U. Therios, R. F. Kulak, and Q. Wu, "The STAR-LM Lead-Cooled Closed Fuel Cycle Fast Reactor with a Supercritical Carbon Dioxide Brayton Cycle Advanced Power Converter," Global 2003: Atoms for Prosperity: Updating Eisenhowers Global Vision for Nuclear Energy, pp. 916-926.

13. P. Hejzlar, V. Dostal, M. Driscoll, P. Dumaz, G. Poullennec, and N. Alpy, "Assessment of Gas Cooled Fast Reactor with Indirect SCO_2 Cycle," Nuclear Engineering and Technology, Vol. 38 No. 2.

14. J. Sienicki, A. Moisseytsev, D. Cho, Y. Momozaki, D. Kilsdonk, R. Haglund, C. Reed, and M. Farmer, "Supercritical Carbon Dioxide Brayton Cycle Energy Conversion for Sodium-Cooled Fast Reactors / Advanced Burner Reactors," Global 2007, Boise, Idaho (2007).

15. T. Ishizuka, Y. Kato, Y. Muto, K. Nikitin, and T. Ngo, "Thermal-Hydraulic Characteristics of a Printed Circuit Heat Exchanger in a Supercritical CO_2 Loop," Bulletin of the Research Laboratory for Nuclear Reactors, Vol. 30, 2006.

16. P. Wu and W. Little, “Measurement of Friction Factor for the Flow of Gases in Very Fine Channels Used for Microminiature Joule-Thompson Refrigerators,” Cryogenics, Vol. 24, pp. 273-277, 1983.

17. J. Phaler, J. Harley, H. Bau, and J. Zemel, “Liquid Transport in Micron and Submicron Channels,” Journal of Sensors and Actuators, Vol. A22, pp. 431-434, 1990.

18. S. Choi, R. Barron, and R. Warrington, “Fluid Flow and Heat Transfer in Microtubes,” Micromechanical Sensors, Actuators and Systems, ASME DSC-Vol. 32, pp. 123-134, 1991.

19. B. Haynes and A. Johnston, “High-Effectiveness Micro-Exchanger Performance,” Unpublished.

20. I. Pioro, H. Khartabil, and R. Duffey, “Heat Transfer to Supercritical Fluids Flowing in Channels – Empirical Correlations (Survey),” Nuclear Engineering and Design, Vol. 230, pp. 69-91, 2004.

21. S. Kandlikar and W. Grande, “Evolution of Microchannel Flow Passages – Thermohydraulic Performance and Fabrication Technology,” Heat Transfer Engineering, Vol. 24, pp. 3-17, 2003.

22. A. Efanov, N. Loginov, V. Privezentsev, "Heat Transfer at Liquid Flow in MicroChannels," NURETH-11, Avignon, France (2005).

23. T. Adams, S. Abdel-Khalik, S. Jeter, Z. Quresh, "An experimental Investigation of Single-Phase Forced Convection in Microchannels," Int. Journal of Heat and Mass Transfer 41 (1998), pp. 851-857.

24. S. Mehendale, A. Jacobi, and R. Shah, “Fluid Flow and Heat Transfer at Micro- and Meso-Scales with Applications to Heat Exchanger Design,” Applied Mechanics Review, Vol. 53, pp. 175-193, 2000.

25. V. Gnielinski, “New Equations for Heat and Mass Transfer in Turbulent Pipe and Channel Flow,” International Chemical Engineering, Vol. 16, April 1976.

26. X. Peng, G. Peterson, and B. Wang, “Heat Transfer Characteristics of Water Flowing Through Microchannels,” Experimental Heat Transfer, Vol. 7, pp. 265-283, 1994.

27. X. Peng and G. Peterson, “Convective Heat Transfer and Flow Friction for Water Flow in Microchannel Structures,” International Journal of Heat and Mass Transfer, Vol. 39, pp. 2599-2608.

28. B. Wang and X. Peng, "Experimental Investigation of Liquid Forced-Convection Heat Transfer through Microchannels," Int. Journ of Heat and Mass Tranfer 17 (1994), pp 73-82.

29. X. Peng, G. Peterson, and B. Wang, "Frictional Flow Characteristics of Water Flowing Through Rectangular Microchannels," Experimental Heat Transfer (7), 1994, pp. 249-264.

30. Z. Jiao, Z. Ni, N. Zhang, and H. Kung, “The Resistance and Heat Transfer in Zigzag Duct and the Performance of Plate Heat Exchangers,” ASME Heat Transfer Division, Vol. 76, pp. 85-90, 1987.

31. J. O’Brien and E. Sparrow, “Corrugated-Duct Heat Transfer, Pressure Drop, and Flow Visualization,” ASME Journal of Heat Transfer, Vol. 104, pp. 410-416, 1982.

32. T. Clifford, “Fundamentals of Supercritical Fluids,” Oxford University Press, New York, 1999.

33. Song, H., “Investigation of a Printed Circuit Heat Exchanger for Supercritical CO_2 and Water,” M.S. Degree Thesis, Kansas State University, 2007.

34. S. Liao and T. Zhao, “An Experimental Investigation of Convection Heat Transfer to Supercritical Carbon Dioxide in Miniature Tubes,” International Journal of Heat and Mass Transfer, Vol. 45, pp. 5025-5034, 2002.

35. S. Pitla, D. Robinson, E. Groll, and S. Ramadhyani, “Heat Transfer from Supercritical Carbon Dioxide in Tube Flow: A Critical Review,” HVAC&R Research, Vol. 4, July 1998.

36. I. Pioro, H. Khartabil, and R. Duffey, “Heat Transfer to Supercritical Fluids Flowing in Channels – Empirical Correlations (Survey),” Nuclear Engineering and Design, Vol. 230, pp. 69-91, 2004.

37. R. Bringer and J. Smith, “Heat Transfer in the Critical Region,” AlChE Journal, Vol. 3, pp. 49-54, 1957.

38. E. Krasnoshchekov and V. Protopopov, “Heat Transfer at Supercritical Region in Flow of Carbon Dioxide and Water in Tubes,” Thermal Engineering, Vol. 12, pp. 26-30, 1959.

39. E. Krasnoshchekov, V. Protopopov, V. Fen, and I. Kuraeva, “Experimental Investigation of Heat Transfer for Carbon Dioxide in the Supercritical Region,” Rand Report R-451-PR, Vol. 1, pp. 26-35, 1967.

40. J. Jackson, “Consideration of the Heat Transfer Properties of Supercritical Pressure Water in Connection with the Cooling of Advanced Nuclear Reactors,”

Proceedings of the 13th Pacific Basin Nuclear Conference, Shenzhen City, China, October 2002.

41. S. Liao and T. Zhao, "Measurements of Heat Transfer Coefficients from Supercritical Carbon Dioxide Flowing in Horizontal Mini/Micro Channels," Journal of Heat Transfer, pp. 413-420, June 2002.

42. S. Liao and T. Zhao, "An Experimental Investigation of Convection Heat Transfer to Supercritical Carbon Dioxide in Miniature Tubes," International Journal of Heat and Mass Transfer, Vol. 45, pp. 5025-5034, 2002.

43. X. Huai, S. Koyama, and T. Zhao, "An Experimental Study of Flow and Heat Transfer of Supercritical Carbon Dioxide in Multi-Port Mini Channels Under Cooling Conditions," Chemical Engineering Science, Vol. 60, pp. 3337-3345, 2005.

44. www.emersonprocess.com, 2006.

45. Shah, "Fundamentals of Heat Exchanger Design," Wiley, 2003.

46. P. Asinari, "Numerical Prediction of Turbulent Convective Heat Transfer in Mini/Micro Channels for CO2 at Supercritical Pressure," International Journal of Heat and Mass Transfer, Vol. 48, pp. 3864-3879, 2005.

47. http://webbook.nist.gov/chemistry/fluid/, 2005.

48. Duffey, R. and Pioro, I., "Experimental Heat Transfer of Supercritical Carbon Dioxide Flowing Inside Channels (Survey)," Nuclear Engineering and Design, Vol. 235, pp. 913-924, 2005.

49. FLUENT User's Manual. www.fluentusers.com, 2008

Appendix A – Experimental Data

Table A.1: Hot Side Pressure Drop Data – Water [33]

Test	m_h (kg/hr)	Re	T_h (ºC)	ΔP_h (kPa)	90% ΔP_h (kPa)
Hot PD 1	190.12	84.88	50.0	1.40	1.26
Hot PD 2	310.53	138.98	50.2	2.55	2.30
Hot PD 3	400.73	179.25	50.1	3.71	3.34
Hot PD 4	600.28	268.28	50.1	6.61	5.95
Hot PD 5	805.05	359.57	50.0	10.57	9.51
Hot PD 6	999.34	445.46	49.9	15.06	13.55
Hot PD 7	1199.13	535.31	50.0	20.20	18.18

Table A.2: Cold Side Pressure Drop Data – Water [33]

Test	m_c (kg/hr)	Re	T_c (ºC)	ΔP_c (kPa)	90% ΔP_c (kPa)
Cold PD 1	153.27	77.30	50.2	1.66	1.49
Cold PD 2	309.32	155.81	50.1	4.62	4.16
Cold PD 3	517.01	260.58	50.2	10.11	9.10
Cold PD 4	703.00	355.57	50.4	17.17	15.45
Cold PD 5	981.15	494.81	50.2	29.94	26.95
Cold PD 6	1199.21	605.13	50.3	42.11	37.90

Table A.3: Experimental Conditions for Small Temperature Difference Testing at 8.0 MPa

Test No.	p_h	$\dot{m}_h$	T_{h_in}	T_{h_out}	$\dot{m}_w$	T_{c_in}	T_{c_out}
	MPa	kg/hr	^oC	^oC	kg/hr	^oC	^oC
SD1	79.87	248.53	33.87	33.00	698.21	32.52	33.55
SD2	79.87	248.26	35.05	34.01	690.96	32.18	34.90
SD3	80.11	252.01	35.31	34.26	696.59	32.19	35.22
SD4	80.05	248.62	35.56	34.68	698.00	32.32	35.45
SD5	79.96	248.20	35.94	35.06	696.11	32.59	35.87
SD6	80.13	249.73	36.83	35.54	692.04	33.54	36.65
SD7	80.07	247.68	37.3	35.87	701.27	34.43	37.05
SD8	80.05	250.49	38.48	37.03	700.10	36.43	37.88
SD9	80.05	250.39	39.42	38.09	699.32	37.65	38.61

Table A.4: Experimental Conditions for Test Set B

Test No.	p_h	T_{pseudo}	C_{p_pseudo}	$\dot{m}_h$	T_{h_in}	T_{h_out}	$\dot{m}_w$	T_{c_in}	T_{c_out}
	MPa	°C	J/g·K	kg/hr	°C	°C	kg/hr	°C	°C
B1	8.006	34.67	34.82	99.49	88.39	34.75	707.78	34.32	40.29
B2	8.001	34.64	35.12	200.65	88.62	34.71	701.88	32.60	45.08
B3	8.004	34.66	34.95	300.15	88.65	34.73	703.72	30.54	49.18
B4	7.998	34.62	35.30	398.73	87.54	34.63	706.20	27.93	52.67
B5	8.001	34.64	35.12	498.05	86.44	34.68	704.38	25.43	55.89
B6	8.003	34.65	34.99	100.53	88.63	36.07	701.59	35.63	40.54
B7	8.001	34.64	35.12	200.77	88.10	35.98	699.78	35.11	45.08
B8	7.972	34.48	37.07	297.14	89.36	36.20	701.80	35.05	48.89
B9	8.003	34.65	34.99	401.01	87.92	36.05	701.77	33.28	52.96
B10	7.995	34.61	35.52	500.61	87.93	35.90	700.09	31.28	56.44
B11	8.003	34.65	34.99	100.03	87.68	37.94	697.80	37.68	41.61
B12	8.005	34.66	34.86	199.73	88.85	37.97	697.80	37.53	45.66
B13	7.998	34.62	35.30	301.31	88.17	38.03	699.86	37.48	49.51
B14	8.020	34.75	33.97	404.29	88.97	38.29	701.62	37.58	53.49
B15	7.998	34.63	35.34	501.79	88.09	38.01	702.25	36.83	56.60

Table A.5: Experimental Conditions for Test Set C

Test No.	p_h	T_{pseudo}	C_{p_pseudo}	$\dot{m}_h$	T_{h_in}	T_{h_out}	$\dot{m}_w$	T_{c_in}	T_{c_out}
	MPa	°C	J/g·K	kg/hr	°C	°C	kg/hr	°C	°C
C1	8.987	39.93	12.94	199.20	88.49	40.03	709.12	39.47	50.06
C2	8.990	39.95	12.91	300.78	87.46	39.97	704.87	38.53	54.5
C3	9.002	40.01	12.82	399.78	88.38	39.96	701.91	36.95	58.55
C4	8.987	39.93	12.94	498.40	89.10	39.95	701.20	35.09	62.03
C5	8.998	39.99	12.85	100.48	87.51	42.91	601.65	42.64	47.50
C6	9.005	40.03	12.79	198.90	88.74	42.96	600.67	42.47	52.38
C7	9.005	40.02	12.79	299.11	88.37	42.90	600.48	42.00	56.88
C8	9.005	40.03	12.79	399.47	88.92	42.90	598.37	41.18	61.11
C9	9.004	40.02	12.80	494.92	88.11	42.84	594.21	39.78	64.50
C10	8.996	39.98	12.87	99.91	88.30	45.80	602.09	45.77	49.68
C11	9.004	40.02	12.80	200.90	88.34	45.87	603.06	45.57	53.59
C12	9.006	40.03	12.79	301.49	88.23	45.84	602.23	45.38	57.46
C13	8.994	39.97	12.88	400.09	87.14	45.86	603.21	45.24	60.87
C14	9.008	40.04	12.77	500.74	88.01	45.95	597.86	44.91	64.82

Appendix B – Error Analysis

This appendix calculates the error associated with the S-CO_2 heat transfer coefficients determined in Chapter 4 based on the measurement uncertainties of the instruments used to gather experimental data. The error relations used in these calculations are given in Table B.1.

Table B.1: Error Analysis Rules

Relation between Z and (A,B)	Relation between errors ΔZ and (ΔA, ΔB)	Equation
Z = A + B	$(\Delta Z)^2 = (\Delta A)^2 + (\Delta B)^2$	B.1
Z = A - B	$(\Delta Z)^2 = (\Delta A)^2 + (\Delta B)^2$	B.2
Z = AB	$\left(\frac{\Delta Z}{Z}\right)^2 = \left(\frac{\Delta A}{A}\right)^2 + \left(\frac{\Delta B}{B}\right)^2$	B.3
Z = A/B	$\left(\frac{\Delta Z}{Z}\right)^2 = \left(\frac{\Delta A}{A}\right)^2 + \left(\frac{\Delta B}{B}\right)^2$	B.4
$Z = A^n$	$\frac{\Delta Z}{Z} = n\frac{\Delta A}{A}$	B.5
Z = ln A	$\Delta Z = \frac{\Delta A}{A}$	B.6
$Z = e^A$	$\frac{\Delta Z}{Z} = \Delta A$	B.7

The S-CO_2 heat transfer coefficient is defined by

$$\frac{1}{h_{CO_2}} = \frac{1}{U} - \frac{1}{h_{H_2O}} = \frac{h_{H_2O} - U}{U \cdot h_{H_2O}} \qquad \text{B.8}$$

Equation B.8 is rearranged to

$$h_{CO_2} = \frac{U \cdot h_{H_2O}}{h_{H_2O} - U} \tag{B.9}$$

Propagation of error in h_{CO_2} due to errors in U and h_{H_2O} is expressed using Equation B.4.

$$\frac{\Delta h_{CO_2}}{h_{CO_2}} = \left[\left(\frac{\Delta(U \cdot h_{H_2O})}{U \cdot h_{H_2O}} \right)^2 + \left(\frac{\Delta(h_{H_2O} - U)}{h_{H_2O} - U} \right)^2 \right]^{1/2} \tag{B.10}$$

The overall heat transfer coefficient, U, is defined by

$$q = AU\Delta T_{lm} \tag{B.11}$$

Errors in U are expressed through Equation B.4 as

$$\frac{\Delta U}{U} = \left[(\frac{\Delta q}{q})^2 + (\frac{\Delta T_{lm}}{T_{lm}})^2 \right]^{1/2} \tag{B.12}$$

q can be defined in terms of the enthalpy and mass flow rate of S-CO_2

$$q = \dot{m}_{CO2} \cdot [i_{in} - i_{out}] \tag{B.13}$$

Errors in q are expressed through Equation B.4 as

$$\frac{\Delta q}{q} = \left[\left(\frac{\Delta \dot{m}_{CO2}}{\dot{m}_{CO2}} \right)^2 + \left(\frac{\Delta[i_{in} - i_{out}]}{[i_{in} - i_{out}]} \right)^2 \right]^{1/2} \tag{B.14}$$

The errors in the enthalpy term of Equation B.14 are expressed by Equation B.2 as

$$\Delta(i_{in} - i_{out}) = \left[(\Delta i_{in})^2 + (\Delta i_{out})^2 \right] \tag{B.15}$$

The enthalpy of S-CO_2 shows the highest rate of change with temperature near the pseudocritical point. Therefore the experimental data point selected to calculate error is the one closest to the pseudocritical point, so that this shows the maximum error present in the data. This data point is Test C4, and the experimental conditions are given in Table B.2.

Table Error! No text of specified style in document.**.1: Experimental Data for Test C4**

$T_{h,in}$	$T_{h,out}$	$T_{c,in}$	$T_{c,out}$	ΔT_{lm}	U	Re_h	Re_c	h_{H2O}	h_{CO2}
^oC	^oC	^oC	^oC	^oC	W/m^2	-	-	W/m^2	W/m^2
87.54	34.63	27.93	52.67	17.08	196.68	3664.70	292.87	3803.65	207.41

The enthalpy is affected by temperature which was measured by platinum RTDs. These have an accuracy of 0.1 ºC. The S-CO_2 enthalpy at the inlet and outlet temperatures from Table B.2 as well as temperatures 0.1 ºC higher and lower than these values is shown in Table B.3.

Table Error! No text of specified style in document.**.1: Enthalpy for the hot side**

Temperature	i_{in}	Temperature	i_{out}
87.44^{o}C	502.60 kJ/kg	34.53^{o}C	336.79 kJ/kg
87.54^{o}C	502.75 kJ/kg	34.63 ^{o}C	340.31 kJ/kg
87.64^{o}C	502.89 kJ/kg	34.73^{o}C	343.84 kJ/kg

$$\Delta i_{in} = (502.89 - 502.75) = 0.14 \quad \text{B.16}$$

$$\frac{\Delta i_{in}}{i_{in}} = \frac{(502.89 - 502.75)}{502.75} = 0.000278 \quad \text{B.17}$$

$$\Delta i_{out} = (343.84 - 340.31) = 3.53 \quad \text{B.18}$$

$$\frac{\Delta i_{out}}{i_{out}} = \frac{(343.84 - 340.31)}{340.31} = 0.0103 \quad \text{B.19}$$

These results are substituted into Equation B.15 as follows:

$$\begin{aligned} \Delta[i_{in} - i_{out}] &= \left[(\Delta i_{in})^2 + (\Delta i_{out})^2\right]^{1/2} \\ &= [(0.14)^2 + (3.53)^2]^{1/2} \\ &= 3.53 \end{aligned} \quad \text{B.20}$$

The errors in the mass flow rate can be determined knowing that the flow meter has a maximum error of less than 0.5%.

$$\frac{\Delta \dot{m}_{CO2}}{\dot{m}_{CO2}} = 0.005 \tag{B.21}$$

$$\frac{\Delta q}{q} = \left[\left(\frac{\Delta \dot{m}_{CO2}}{\dot{m}_{CO2}} \right)^2 + \left(\frac{\Delta [i_h - i_l]}{[i_h - i_l]} \right)^2 \right]^{1/2}$$

$$= \left[(0.005)^2 + \left(\frac{3.53}{(502.75 - 340.31)} \right)^2 \right]^{1/2} \tag{B.22}$$

$$= 0.0223$$

Next, we need to estimate the errors in the log mean temperature difference, which is defined by equation B.23.

$$\Delta T_{lm} = \frac{(T_{h,out} - T_{c,in}) - (T_{h,in} - T_{c,out})}{\ln[(T_{h,out} - T_{c,in})/(T_{h,in} - T_{c,out})]} \tag{B.23}$$

From the fourth rule, errors in the log mean temperature difference is written as follows:

$$\frac{\Delta T_{lm}}{T_{lm}}$$

$$= \left[\left(\frac{\Delta[(T_{h,out} - T_{c,in}) - (T_{h,in} - T_{c,out})]}{[(T_{h,out} - T_{c,in})/(T_{h,in} - T_{c,out})]} \right)^2 + \left(\frac{\Delta(\ln[(T_{h,out} - T_{c,in}) - (T_{h,in} - T_{c,out})])}{\ln[(T_{h,out} - T_{c,in})/(T_{h,in} - T_{c,out})]} \right)^2 \right]^{1/2} \tag{B.24}$$

For $(T_{h,out} - T_{c,in}) - (T_{h,in} - T_{c,out})$, the errors are estimated based on the accuracy of 0.1°C by the Equation B.1.

$$[(0.1)^2 + (0.1)^2 + (0.1)^2 + (0.1)^2]^{1/2} = 0.2 \tag{B.25}$$

$$(T_{h,out} - T_{c,in}) - (T_{h,in} - T_{c,out}) = (87.54 - 52.67) - (34.63 - 27.93) = 28.17 \tag{B.26}$$

In $\ln\left[\frac{(T_{h,out} - T_{c,in})}{(T_{h,in} - T_{c,out})}\right]$ term, we define the term inside the bracket as follows:

$$D \equiv \frac{(T_{h,out} - T_{c,in})}{(T_{h,in} - T_{c,out})} \equiv \frac{A}{B} \tag{B.27}$$

We can calculate the errors in A and B due to the RTD error (0.1 °C) by the Equation B.2.

$$\Delta A = \Delta B = [(0.1)^2 + (0.1)^2]^{1/2} = 0.14 \tag{B.28}$$

Using Equation B.4, we can estimate the errors in D.

$$\frac{\Delta D}{D} = \left[\left(\frac{\Delta A}{A} \right)^2 + \left(\frac{\Delta B}{B} \right)^2 \right]^{1/2}$$
$$= \left[\left(\frac{0.14}{34.87} \right)^2 + \left(\frac{0.14}{6.70} \right)^2 \right]^{1/2} \quad \text{B.29}$$
$$= 0.0213$$

where $A = 87.54 - 52.67 = 34.87$, $B = 34.63 - 27.93 = 6.70$

Using Equation B.29, we can estimate the error in $\ln\left[\frac{(T_{h,out} - T_{c,in})}{(T_{h,in} - T_{c,out})} \right]$ using Equation B.6 as shown in Equation B.29.

$$\Delta\left\{ \ln\left[\frac{(T_{h,out} - T_{c,in})}{(T_{h,in} - T_{c,out})} \right] \right\} = \frac{\Delta D}{D} = 0.0213 \quad \text{B.30}$$

Therefore, errors in the log mean temperature difference is calculated using the above results.

$$\frac{\Delta T_{lm}}{T_{lm}}$$
$$= \left[\left(\frac{\Delta\left[(T_{h,out} - T_{c,in}) - (T_{h,in} - T_{c,out}) \right]}{\left[(T_{h,out} - T_{c,in}) - (T_{h,in} - T_{c,out}) \right]} \right)^2 + \left(\frac{\Delta\left(\ln\left[(T_{h,out} - T_{c,in}) / (T_{h,in} - T_{c,out}) \right] \right)}{\ln\left[(T_{h,out} - T_{c,in}) / (T_{h,in} - T_{c,out}) \right]} \right)^2 \right]^{1/2} \quad \text{B.31}$$
$$= \left[\left(\frac{0.2}{28.17} \right)^2 + \left(\frac{0.0213}{1.64} \right)^2 \right]^{1/2}$$
$$= 0.0148$$
$$\Delta T_{lm} = (0.0148) * (17.08) = 0.2528 \quad \text{B.32}$$

Substituting the above results into B.12, we can estimate errors in the overall coefficient as shown in Equation 27.

$$\frac{\Delta U}{U} = \left[(\frac{\Delta q}{q})^2 + (\frac{\Delta T_{lm}}{T_{lm}})^2 \right]^{1/2}$$
$$= \left[(0.0223)^2 + (0.0148)^2 \right]^{1/2} \quad \text{B.33}$$
$$= 0.0268$$
$$\Delta U = 0.0268 * (196.68) = 5.26 \quad \text{B.34}$$

For errors in the water side, we need to look at the heat transfer coefficient of water, which is defined by Equation B.35.

$$h_{H2O} = 11.035 * \mathrm{Re}_{H_2O} + 570.36 \qquad \text{B.35}$$

Re_{H_2O} is defined by Equation B.36 and errors in Reynolds number is estimated by Equation B.37 using Equation B.4.

$$\mathrm{Re}_{H2O} = \frac{\rho \cdot u \cdot D}{\mu} \qquad \text{B.36}$$

$$\frac{\Delta \mathrm{Re}_{H_2O}}{\mathrm{Re}_{H_2O}} = \left[\left(\frac{\Delta \rho}{\rho} \right)^2 + \left(\frac{\Delta u}{u} \right)^2 + \left(\frac{\Delta \mu}{\mu} \right)^2 \right]^{1/2} \qquad \text{B.37}$$

Density and viscosity are function of temperature in this study. The errors are caused by the temperature inaccuracy, 0.1°C.

Table Error! No text of specified style in document.**.1 Density and viscosity for CO_2**

Temperature	Density	Viscosity
87.44°C	151.84 kg/m^3	20.167 μPa·s
87.54°C	151.74 kg/m^3	20.169 μPa·s
87.64°C	151.64 kg/m^3	20.171 μPa·s

Using the values shown in Table B.3, each error in Equation B.37 is calculated. The water velocity has errors occurred by the water flow meter, which has an accuracy is 0.5%.

$$\frac{\Delta u}{u} = 0.005 \qquad \text{B.38}$$

$$\frac{\Delta \rho}{\rho} = \frac{(151.74 - 151.64)}{151.74} = 0.000659 \qquad \text{B.39}$$

$$\frac{\Delta \mu}{\mu} = \frac{(20.171 - 20.169)}{20.169} = 0.0000992 \qquad \text{B.40}$$

Substitute the above results into Equation B.37,

$$\frac{\Delta \mathrm{Re}_{H_2O}}{\mathrm{Re}_{H_2O}} = \left[\left(\frac{\Delta u}{u} \right)^2 + \left(\frac{\Delta \rho}{\rho} \right)^2 + \left(\frac{\Delta \mu}{\mu} \right)^2 \right]^{1/2} = 0.005 \quad \text{B.41}$$

So the error in heat transfer coefficient for water is calculated as follows.

$$\frac{\Delta h_{H_2O}}{h_{H_2O}} = \frac{16.16}{3802.18} = 0.0043 \quad \text{B.42}$$

Now, the errors in heat transfer coefficient for CO_2 can be estimated by substitute the above results into Equation B.10. Before that, we need to calculate the two terms in the right hand side of Equation B.10 as follows.

$$\left(\frac{\Delta(U \cdot h_{H_2O})}{U \cdot h_{H_2O}} \right) = \left[\left(\frac{\Delta U}{U} \right)^2 + \left(\frac{\Delta h_{H_2O}}{h_{H_2O}} \right)^2 \right]^{1/2}$$
$$= \left[(0.0268)^2 + (0.0043)^2 \right]^{1/2} \quad \text{B.43}$$
$$= 0.0271$$

$$\Delta(h_{H_2O} - U) = \left[(\Delta h_{H_2O})^2 + (\Delta U)^2 \right]^{1/2}$$
$$= \left[(16.16)^2 + (5.26)^2 \right]^{1/2} \quad \text{B.44}$$
$$= 16.99$$

Therefore, errors in the heat transfer coefficient for S-CO_2 are estimated by Equation B.45.

$$\frac{\Delta h_{CO_2}}{h_{CO_2}} = \left[\left(\frac{\Delta(U \cdot h_{H_2O})}{U \cdot h_{H_2O}} \right)^2 + \left(\frac{\Delta(h_{H_2O} - U)}{h_{H_2O} - U} \right)^2 \right]^{1/2}$$
$$= \left[(0.0271)^2 + \left(\frac{16.99}{(3802.18 - 196.68)} \right)^2 \right]^{1/2} \quad \text{B.45}$$
$$= 0.0275$$

From these calculations, the error in heat transfer coefficient for S-CO_2 in this work is ±3%.

Appendix C – Experimental Procedure

This appendix shows the ANL Procedure for operational testing of the ANL PCHE with S-CO_2 and water.

Procedure for Testing a Compact Heat Exchanger with the SNAC Facility

This document describes the procedure used to precondition and run the SNAC facility for testing the performance of a compact heat exchanger with supercritical CO_2. The procedure describes the method used to establish a pure CO_2 atmosphere at a pressure ~60 bar and ambient temperature on the hot side of the loop. It then details a method that can be used to increase the hot side temperature and pressure to produce supercritical CO_2 (T_{cr} = 31°C ; P_{cr} = 73.8 bar). The procedure also includes an outline of the typical steps used to conduct the HX testing itself (data collection), followed by shutdown and emergency procedures.

Note that this procedure is intended only as a guide and, with the exception of the section describing emergency shutdown, no part of this procedure is mandatory. The actual procedure used to operate the SNAC loop and test the heat exchanger is left to the discretion of the operator.

Initial charge of CO_2 for the loop primary side

1) Connect vacuum pump to loop via ¼" hose and Swagelok fittings.
2) Open pump isolation valve and evacuate pump to ~0.1 bar as shown by Rosemount transmitter.
3) Close pump isolation valve.
4) Open valve on line to CO_2 reservoir and pressurize loop to ~1 bar.
5) Close valve on line to CO_2 reservoir.
6) Repeat steps 2-5 three times to establish an essentially pure CO_2 atmosphere within the loop.
7) Pressurize the loop to slightly above 1 bar.
8) Remove ¼" hose and quickly replace Swagelok cap. Tighten fitting.
9) Open valve on line to CO_2 reservoir *slightly* to slowly pressurize the loop. If gas flow is too high, the valve will ice up and the seat may begin to leak. A conservative method is to pressurize to ~20 bar and let the system stand for 20-30 minutes to let the valve warm up to room temperature.
10) Initial pressurization is complete when the system reaches the reservoir pressure, ~60 bar.

Supplemental charge of CO_2

Because the reservoir pressure is only ~60 bar, we are unable to charge the loop up to supercritical pressures directly from the gas bottle. The loop pressure can be increased by heating the fluid and/or adding helium to the pressurizer. However, we would like to minimize the amount of helium added to the pressurizer to reduce the chances of helium transport into the loop itself.

This part of the procedure describes a technique used to increase the loop CO_2 inventory by lowering the loop temperature below ambient temperature to draw in extra gas from the reservoir. The added CO_2 makes it easier to reach supercritical pressure when the loop is later heated. The chiller in the hi-bay is used to cool the loop.

1) In the hi-bay, turn on the chiller pump to establish flow to the cooling coils. Turn on the switch marked "refrigeration" and check that thermostat is set to about 1^{o}C.
2) Switch the 3-way valve on the secondary side so that the lab water is routed through the copper cooling coils. Open valve on lab water line that supplies cooling to the secondary side. Open the valve only a little bit to keep the water flow rate low so that the temperature drop across the copper coils is maximized. Turn on gear pump and run at a low speed, <20 Hz.
3) Loop pressure should drop as the secondary side cools the primary. Open valve on CO_2 reservoir to allow in-flow of additional CO_2.
4) Wait until HX temperatures stabilize. This will take about 15-30 minutes and the CO_2 temperature will stabilize around 5-10^{o}C.
5) Close valves on line to CO_2 reservoir and secondary side cooling. Turn off chiller.
6) Turn off gear pump.

HX testing

Helium may be added at this stage to increase the loop pressure beyond the critical pressure. If the loop pressure is already above 60 bar, the added helium should not cause problems. If the pressure is lower, it is suggested that the loop be heated at low power to increase the pressure before adding helium.

1) Check ΔP signals, which should read zero ± 0.05 kPa with no flow on either the primary or secondary sides. If necessary, purge water from secondary side lines to achieve an acceptable reading at zero flow.
2) Initiate secondary side water flow by opening valve on secondary side water line.
3) Verify that the pressurizer is connected to main loop (isolation valves *open*).
4) Check that power supply control vernier (on control panel) is set to zero.
5) Open padlock on isolation switch for 480 VAC supply.

6) Open valve on cooling water for power supply. The first two trip lights on control panel should light up.

7) Set gear pump speed control to 15 Hz and then turn on the pump to circulate the CO_2 on the primary side.

8) Activate voltage and current trip overrides (the two right hand toggle switches on the control panel should be in the "up" position). All four trip lights should be "on".

9) Engage 480 VAC by pushing black button. There will be an audible closing of the breaker. The power supply is now energized and can be controlled through the verniers on the control panel.

10) Begin low level loop heating. Slowly turn vernier to 2.4, which is the level that the regulators first switch "on" and begin to supply current. Both the current and voltage meters should now be showing low, nonzero values. The power supply is now operating at low level and providing a few hundred watts of heating.

11) Deactivate trip overrides: *first* press the reset buttons on the current and voltage meters and then move the two right hand override toggle switches to the down position. The system is now able to trip on over and under ranges in current and voltage.

12) Slowly increase power to about 2 kW by adjustment of the vernier. Power may be increased to raise loop pressure before final addition of helium. Be watchful for excessive boiling in the heater section if the pressure is low.

13) Helium may be added to achieve target operating pressure. Pressure must not exceed 80 bar (rupture disk setting is 84 bar).

14) Flow rates and power may now be adjusted as desired. During all adjustments, keep in mind the upper bound pressure limit. Gas may be bled from the pressurizer to lower pressure when necessary. Keep in mind that adjustments should not allow the loop pressure to fall below the critical pressure, which precipitates boiling and can cause an upswing in pressure that exceeds the rupture disk rating).

Normal shutdown

The following steps should be used for all normal shutdowns and also unplanned shutdowns that do not involve emergencies directly related to room C-111 or the loop itself. This includes the need to shutdown because of a general fire alarm, tornado drill/warning, or any similar evacuation order that allows one to safely leave the lab and/or building within ~1 minute.

1) Switch off power by turning vernier to zero. When the current and/or voltage falls below the trip set points there will be an audible opening of the breaker in the 480 VAC supply. The power supply is now switched off.

2) Turn off pump.

3) Close valve on power supply cooling water.

4) Close valve on line providing water flow to HX secondary side.

5) Isolate loop from pressurizer by closing one of the ¼" valves (this step is only to minimize gas loss in case there is a substantial leak, and to help identify the source of the leak, but this step is not required).

6) Lock out 480 VAC mains by closing padlock and returning key to console drawer.

Emergency shutdown

This procedure should be used in the event of fire, electrical failure, heater over-temperature, sudden depressurization, or any other event that calls for an urgent shutdown of the loop:

1) Push red "trip" button.

2) Leave room and dial 911 if necessary, e.g., in the case of fire or injury.

3) If disabling power supply with trip button terminates emergency condition, e.g., heater over temperature or burst of a rupture disk, proceed with normal shutdown procedure.

Appendix D - Thermophysical properties of CO_2

This appendix lists the thermophysical properties of CO_2 at pressures of 74, 75, 80, 85, and 90 bar. At each pressure, specific heat, density, thermal conductivity, enthalpy, viscosity, and thermal diffusivity will be shown in the order.

Table D.1: Thermal properties at 74bar

Temperature (^oC)	Density (kg/m3)	Internal Energy (kJ/kg)	Enthalpy (kJ/kg)	Cv (J/g*K)	Cp (J/g*K)	Viscosity (uPa*s)	Therm. Cond. (W/m*K)	Phase
20	816.82	10.543	10.942	42.228	138.61	73.661	0.091125	liquid
21	806.68	10.679	11.083	42.441	143.7	71.828	0.089651	liquid
22	795.93	10.82	11.23	42.687	149.69	69.952	0.08815	liquid
23	784.43	10.968	11.383	42.973	156.87	68.021	0.086623	liquid
24	772.03	11.122	11.544	43.312	165.67	66.018	0.085073	liquid
25	758.5	11.286	11.715	43.722	176.78	63.923	0.083507	liquid
26	743.52	11.461	11.899	44.232	191.43	61.703	0.081946	liquid
27	726.57	11.651	12.1	44.892	211.98	59.307	0.080437	liquid
28	706.7	11.865	12.326	45.795	243.54	56.643	0.0791	liquid
29	682.02	12.117	12.595	47.147	299.66	53.528	0.078267	liquid
30	647.42	12.447	12.95	49.631	434.86	49.484	0.079145	liquid
31	565.95	13.139	13.715	64.201	2085.7	41.192	0.10034	supercritical
32	314.99	15.628	16.662	54.789	629.89	23.702	0.060668	supercritical
33	288.25	16.006	17.135	50.567	372.81	22.474	0.049917	supercritical
34	271.82	16.258	17.456	48.191	280.28	21.79	0.044723	supercritical
35	259.77	16.456	17.71	46.536	230.85	21.327	0.04144	supercritical
36	250.2	16.622	17.924	45.282	199.57	20.984	0.039112	supercritical
37	242.23	16.768	18.112	44.283	177.77	20.717	0.03735	supercritical
38	235.4	16.898	18.281	43.461	161.6	20.501	0.035958	supercritical
39	229.41	17.017	18.436	42.769	149.07	20.324	0.034826	supercritical
40	224.07	17.127	18.58	42.174	139.04	20.176	0.033884	supercritical
41	219.26	17.23	18.715	41.655	130.81	20.051	0.033089	supercritical
42	214.88	17.327	18.842	41.198	123.91	19.944	0.032407	supercritical
43	210.86	17.419	18.963	40.79	118.05	19.852	0.031818	supercritical
44	207.14	17.506	19.079	40.422	112.98	19.773	0.031303	supercritical
45	203.68	17.59	19.189	40.089	108.57	19.704	0.030851	supercritical
46	200.45	17.671	19.296	39.786	104.67	19.645	0.030451	supercritical
47	197.42	17.749	19.399	39.508	101.21	19.594	0.030095	supercritical
48	194.57	17.825	19.499	39.251	98.12	19.549	0.029778	supercritical
49	191.87	17.898	19.595	39.015	95.332	19.511	0.029494	supercritical
50	189.31	17.969	19.689	38.795	92.807	19.478	0.029239	supercritical
51	186.89	18.038	19.781	38.591	90.508	19.45	0.02901	supercritical

52	184.57	18.106	19.87	38.401	88.406	19.426	0.028804	supercritical
53	182.36	18.172	19.958	38.224	86.476	19.407	0.028617	supercritical
54	180.25	18.237	20.043	38.058	84.698	19.39	0.028449	supercritical
55	178.23	18.3	20.127	37.903	83.053	19.377	0.028297	supercritical
56	176.28	18.362	20.21	37.758	81.528	19.367	0.028159	supercritical
57	174.41	18.423	20.29	37.621	80.109	19.36	0.028035	supercritical
58	172.62	18.483	20.37	37.493	78.786	19.355	0.027922	supercritical
59	170.88	18.542	20.448	37.373	77.55	19.353	0.027821	supercritical
60	169.21	18.6	20.525	37.259	76.391	19.352	0.02773	supercritical
61	167.59	18.658	20.601	37.153	75.304	19.354	0.027647	supercritical
62	166.03	18.714	20.676	37.052	74.281	19.357	0.027574	supercritical
63	164.52	18.77	20.749	36.958	73.317	19.362	0.027508	supercritical
64	163.05	18.825	20.822	36.868	72.407	19.369	0.027449	supercritical
65	161.63	18.879	20.894	36.784	71.547	19.377	0.027397	supercritical
66	160.24	18.933	20.965	36.704	70.733	19.387	0.027351	supercritical
67	158.9	18.986	21.036	36.629	69.96	19.398	0.027311	supercritical
68	157.6	19.039	21.105	36.557	69.227	19.41	0.027277	supercritical
69	156.33	19.091	21.174	36.49	68.53	19.423	0.027247	supercritical
70	155.09	19.142	21.242	36.426	67.866	19.437	0.027222	supercritical
71	153.89	19.194	21.31	36.366	67.234	19.452	0.027202	supercritical
72	152.71	19.244	21.377	36.309	66.63	19.469	0.027185	supercritical
73	151.57	19.294	21.443	36.255	66.054	19.486	0.027172	supercritical
74	150.45	19.344	21.509	36.203	65.503	19.504	0.027163	supercritical
75	149.36	19.394	21.574	36.155	64.977	19.523	0.027158	supercritical
76	148.3	19.443	21.639	36.109	64.472	19.543	0.027156	supercritical
77	147.26	19.491	21.703	36.065	63.989	19.563	0.027156	supercritical
78	146.24	19.54	21.767	36.024	63.525	19.584	0.02716	supercritical
79	145.24	19.588	21.83	35.985	63.08	19.606	0.027166	supercritical
80	144.27	19.636	21.893	35.948	62.652	19.628	0.027175	supercritical
81	143.31	19.683	21.955	35.913	62.241	19.651	0.027187	supercritical
82	142.38	19.73	22.018	35.88	61.846	19.675	0.0272	supercritical
83	141.46	19.777	22.079	35.849	61.465	19.699	0.027216	supercritical
84	140.56	19.824	22.14	35.819	61.099	19.724	0.027234	supercritical
85	139.68	19.87	22.201	35.791	60.746	19.749	0.027254	supercritical
86	138.82	19.916	22.262	35.765	60.406	19.774	0.027276	supercritical
87	137.97	19.962	22.322	35.74	60.077	19.801	0.0273	supercritical
88	137.14	20.007	22.382	35.717	59.761	19.827	0.027325	supercritical
89	136.33	20.053	22.442	35.695	59.455	19.854	0.027352	supercritical
90	135.53	20.098	22.501	35.675	59.16	19.882	0.027381	supercritical

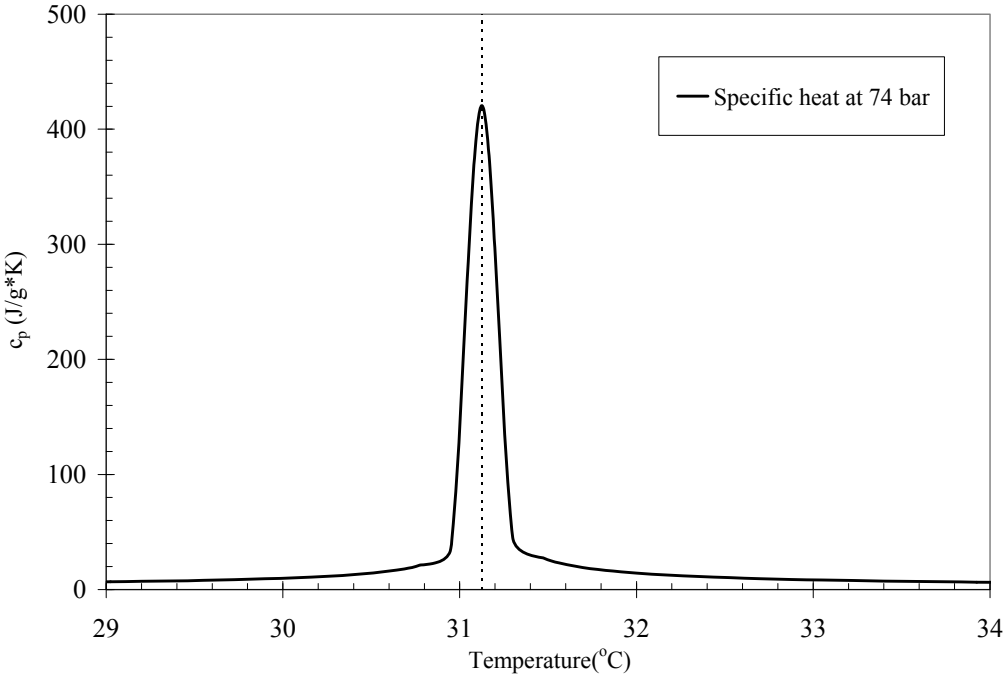

Figure D.1: Specific heat at 74bar

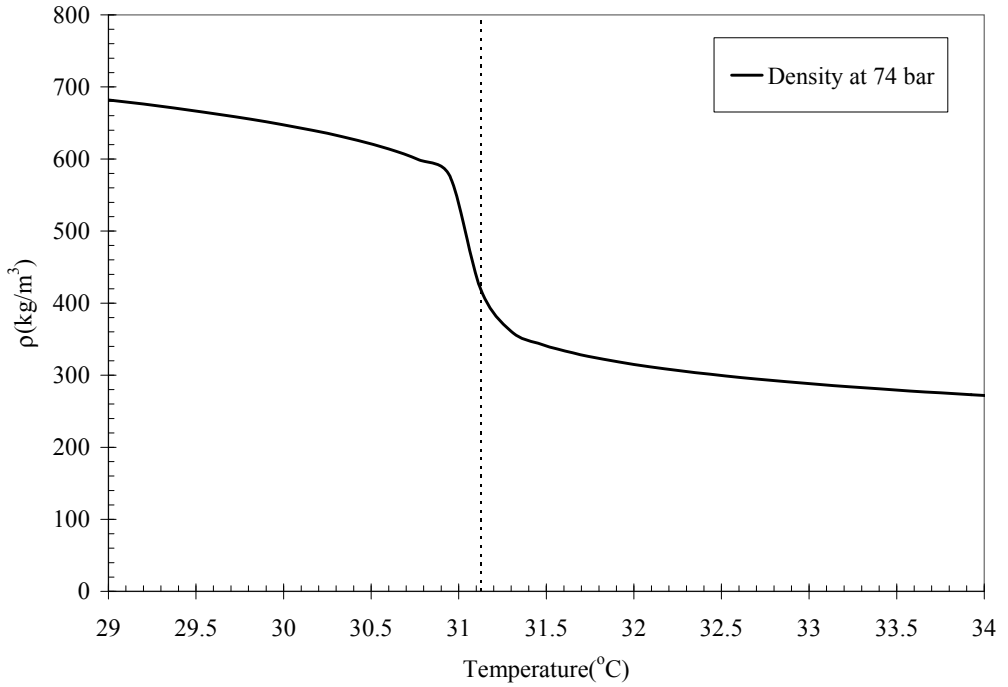

Figure D.2: Density at 74bar

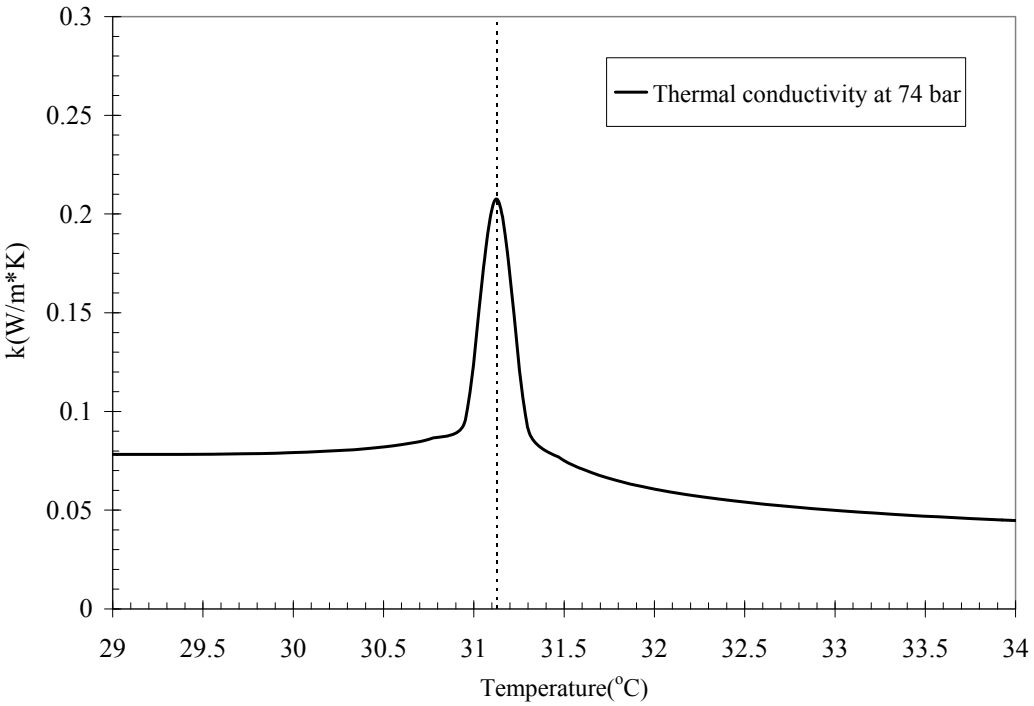

Figure D.1: Thermal Conductivity at 74bar

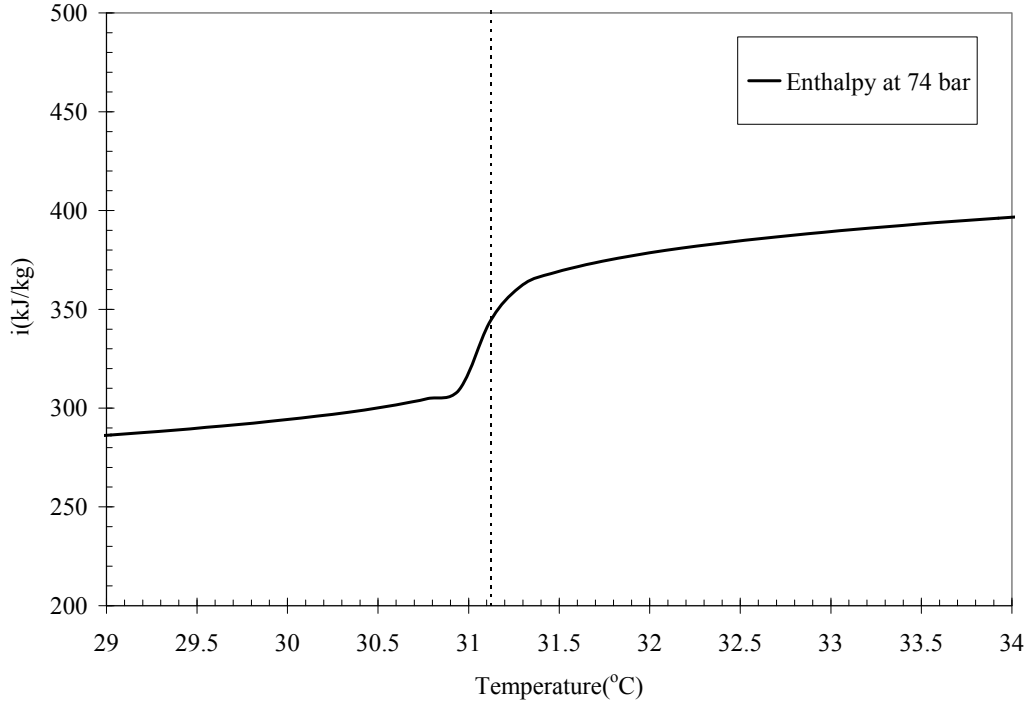

Figure D.1: Enthalpy at 74bar

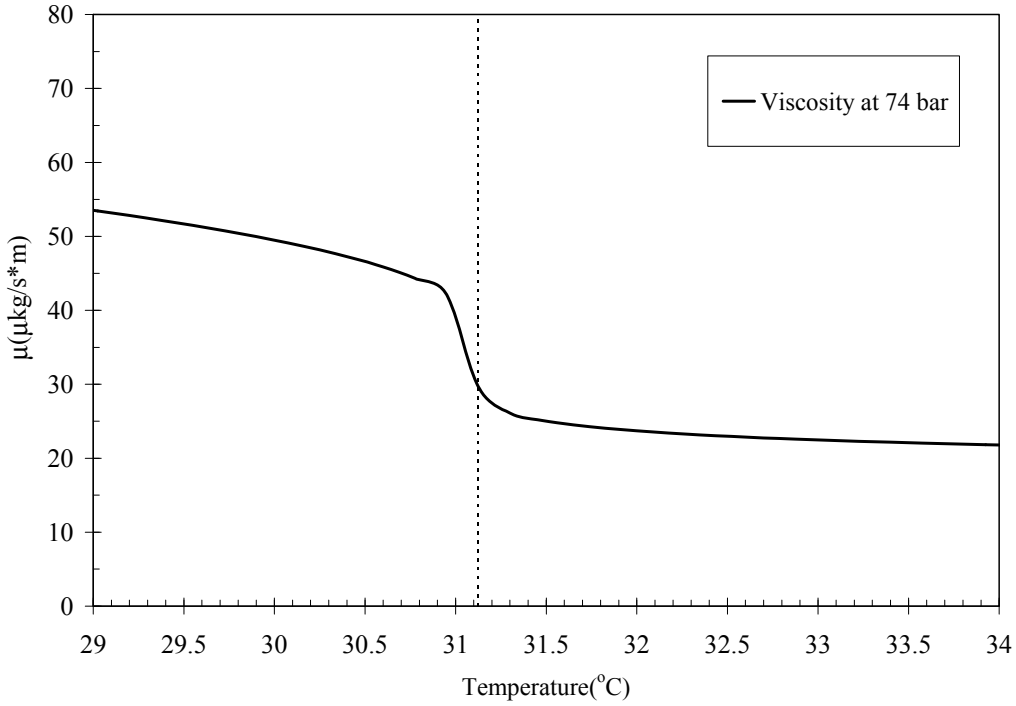

Figure D.1: Viscosity at 74bar

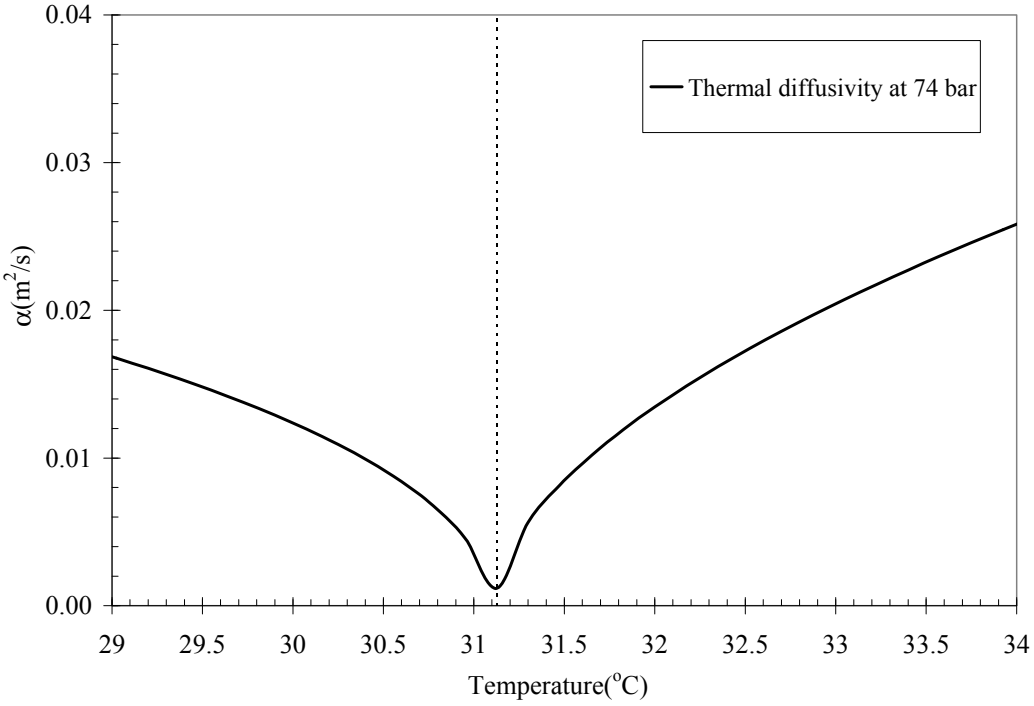

Figure D.2: Thermal diffusivity at 74bar

Table D.1: Thermophysical properties of CO2 at 75bar

Temperature (°C)	Density (kg/m3)	Internal Energy (kJ/kg)	Enthalpy (kJ/kg)	Cv (J/g*K)	Cp (J/g*K)	Viscosity (uPa*s)	Therm. Cond. (W/m*K)	Phase
20	818.74	10.525	10.928	42.157	137.16	74.019	0.091411	liquid
21	808.79	10.66	11.068	42.359	141.98	72.207	0.08995	liquid
22	798.25	10.799	11.213	42.592	147.61	70.356	0.088463	liquid
23	787.02	10.944	11.364	42.862	154.31	68.455	0.086951	liquid
24	774.96	11.096	11.522	43.179	162.42	66.49	0.085414	liquid
25	761.87	11.256	11.689	43.558	172.52	64.442	0.083859	liquid
26	747.47	11.426	11.868	44.024	185.58	62.286	0.082299	liquid
27	731.34	11.61	12.062	44.617	203.35	59.978	0.08077	liquid
28	712.77	11.814	12.277	45.404	229.43	57.45	0.079352	liquid
29	690.38	12.048	12.526	46.52	272.25	54.572	0.078251	liquid
30	661.1	12.336	12.835	48.301	358.15	51.055	0.078087	liquid
31	614.17	12.763	13.3	52.41	648.55	45.925	0.081862	supercritical
32	365.93	15.039	15.941	62.312	1655	26.429	0.086212	supercritical
33	311.47	15.724	16.784	53.063	519.48	23.576	0.056981	supercritical
34	288.3	16.055	17.2	49.744	343.29	22.524	0.048759	supercritical
35	272.97	16.292	17.501	47.663	267.15	21.888	0.04424	supercritical
36	261.4	16.482	17.745	46.161	223.67	21.443	0.041244	supercritical
37	252.07	16.644	17.953	45.001	195.16	21.107	0.039063	supercritical
38	244.24	16.786	18.138	44.067	174.88	20.843	0.037387	supercritical
39	237.48	16.915	18.305	43.293	159.61	20.629	0.036048	supercritical
40	231.53	17.033	18.458	42.636	147.66	20.452	0.03495	supercritical
41	226.22	17.142	18.601	42.068	138.03	20.303	0.034032	supercritical
42	221.42	17.244	18.735	41.571	130.07	20.176	0.033253	supercritical
43	217.04	17.341	18.861	41.131	123.37	20.068	0.032582	supercritical
44	213.01	17.432	18.982	40.737	117.65	19.974	0.032	supercritical
45	209.28	17.52	19.097	40.381	112.69	19.894	0.031491	supercritical
46	205.81	17.604	19.207	40.057	108.36	19.824	0.031042	supercritical
47	202.57	17.684	19.314	39.762	104.53	19.763	0.030645	supercritical
48	199.52	17.762	19.417	39.49	101.13	19.71	0.030291	supercritical
49	196.65	17.838	19.516	39.24	98.073	19.664	0.029975	supercritical
50	193.93	17.911	19.613	39.008	95.319	19.624	0.029691	supercritical
51	191.36	17.982	19.707	38.793	92.821	19.59	0.029436	supercritical
52	188.91	18.051	19.799	38.593	90.545	19.561	0.029207	supercritical
53	186.58	18.119	19.888	38.407	88.461	19.536	0.029	supercritical
54	184.36	18.185	19.976	38.233	86.547	19.515	0.028812	supercritical
55	182.23	18.25	20.061	38.07	84.781	19.498	0.028643	supercritical
56	180.19	18.313	20.145	37.917	83.147	19.483	0.02849	supercritical
57	178.23	18.376	20.228	37.774	81.631	19.472	0.028351	supercritical
58	176.34	18.437	20.309	37.64	80.22	19.464	0.028226	supercritical
59	174.53	18.497	20.388	37.514	78.904	19.458	0.028112	supercritical
60	172.78	18.556	20.466	37.395	77.672	19.455	0.02801	supercritical
61	171.09	18.614	20.543	37.284	76.518	19.453	0.027917	supercritical
62	169.46	18.672	20.619	37.179	75.435	19.454	0.027834	supercritical
63	167.88	18.728	20.694	37.08	74.415	19.457	0.027759	supercritical
64	166.35	18.784	20.768	36.986	73.454	19.461	0.027692	supercritical

65	164.87	18.839	20.841	36.898	72.546	19.467	0.027632	supercritical
66	163.43	18.894	20.913	36.815	71.688	19.474	0.027579	supercritical
67	162.04	18.948	20.985	36.736	70.874	19.483	0.027532	supercritical
68	160.68	19.001	21.055	36.662	70.103	19.493	0.027491	supercritical
69	159.36	19.054	21.125	36.591	69.371	19.504	0.027455	supercritical
70	158.08	19.106	21.194	36.525	68.674	19.517	0.027425	supercritical
71	156.83	19.158	21.262	36.462	68.011	19.53	0.027399	supercritical
72	155.62	19.209	21.33	36.402	67.378	19.545	0.027377	supercritical
73	154.43	19.26	21.397	36.346	66.775	19.561	0.02736	supercritical
74	153.27	19.31	21.463	36.292	66.199	19.577	0.027346	supercritical
75	152.15	19.36	21.529	36.241	65.648	19.595	0.027336	supercritical
76	151.04	19.41	21.595	36.193	65.121	19.613	0.02733	supercritical
77	149.97	19.459	21.66	36.148	64.616	19.632	0.027326	supercritical
78	148.92	19.508	21.724	36.105	64.132	19.652	0.027326	supercritical
79	147.89	19.556	21.788	36.064	63.668	19.672	0.027329	supercritical
80	146.88	19.604	21.851	36.025	63.222	19.694	0.027334	supercritical
81	145.89	19.652	21.914	35.989	62.794	19.715	0.027342	supercritical
82	144.93	19.7	21.977	35.954	62.382	19.738	0.027353	supercritical
83	143.99	19.747	22.039	35.921	61.986	19.761	0.027366	supercritical
84	143.06	19.794	22.101	35.89	61.605	19.785	0.027381	supercritical
85	142.15	19.84	22.162	35.861	61.238	19.809	0.027398	supercritical
86	141.26	19.887	22.223	35.833	60.884	19.834	0.027417	supercritical
87	140.39	19.933	22.284	35.807	60.543	19.859	0.027438	supercritical
88	139.54	19.979	22.345	35.783	60.214	19.885	0.027461	supercritical
89	138.7	20.025	22.405	35.759	59.896	19.911	0.027486	supercritical
90	137.87	20.07	22.464	35.738	59.59	19.937	0.027512	supercritical

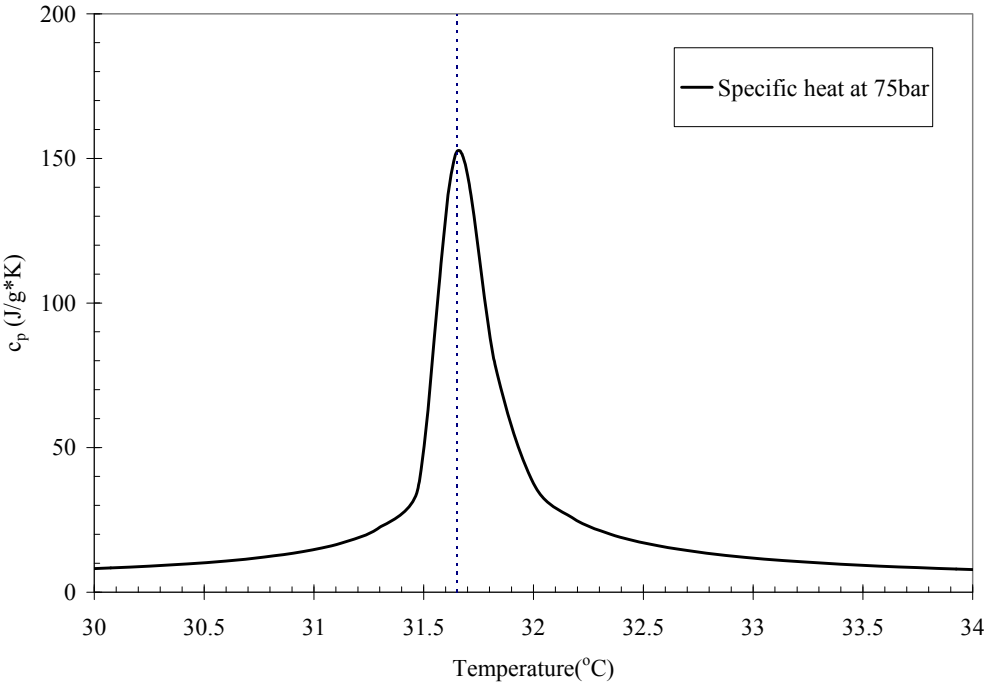

Figure D.1: Specific heat at 75bar

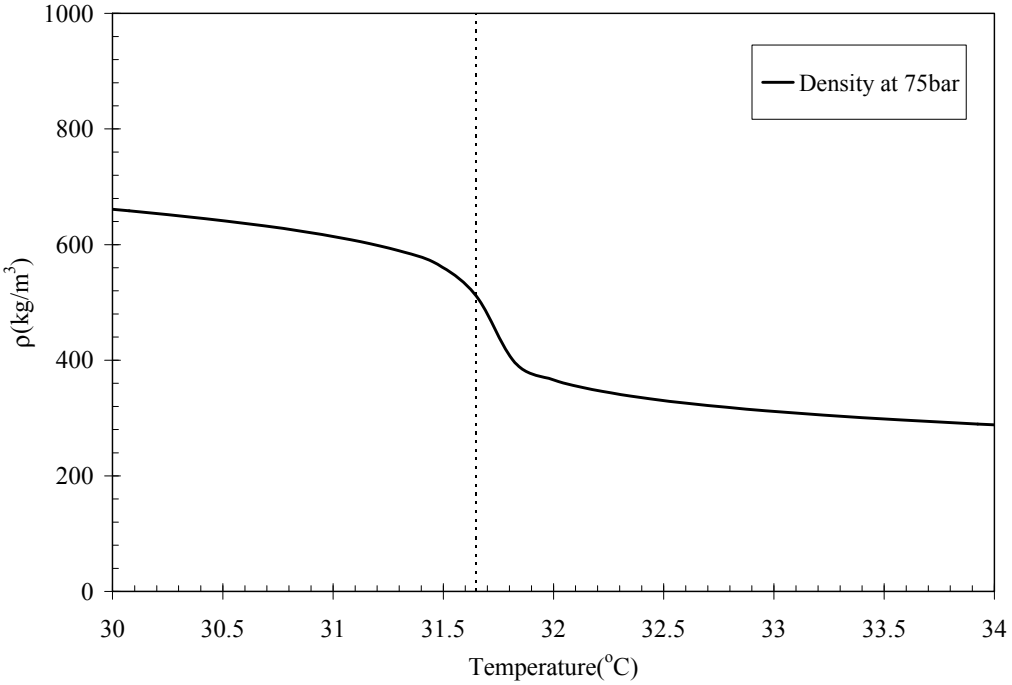

Figure D.2: Density at 75bar

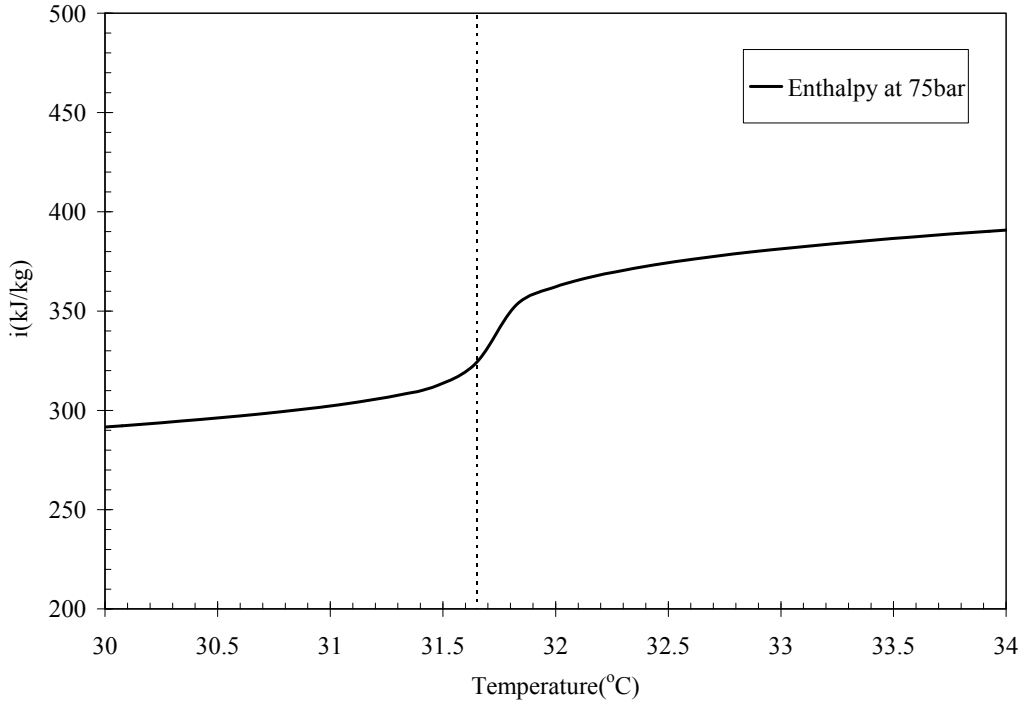

Figure D.1: Enthalpy at 75bar

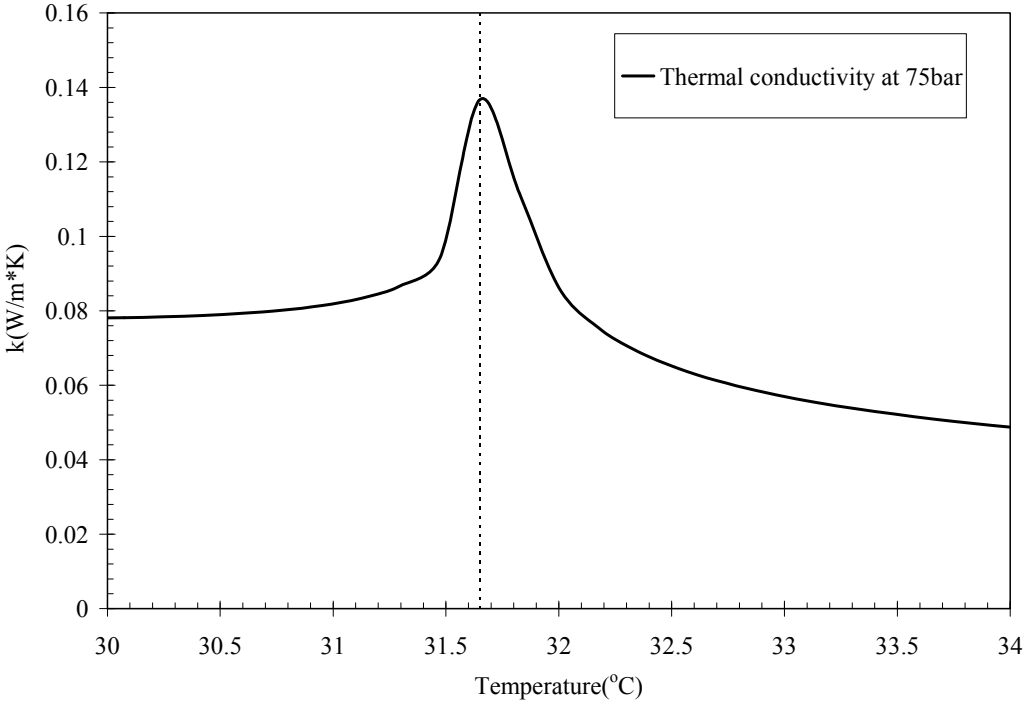

Figure D.2: Thermal conductivity at 75bar

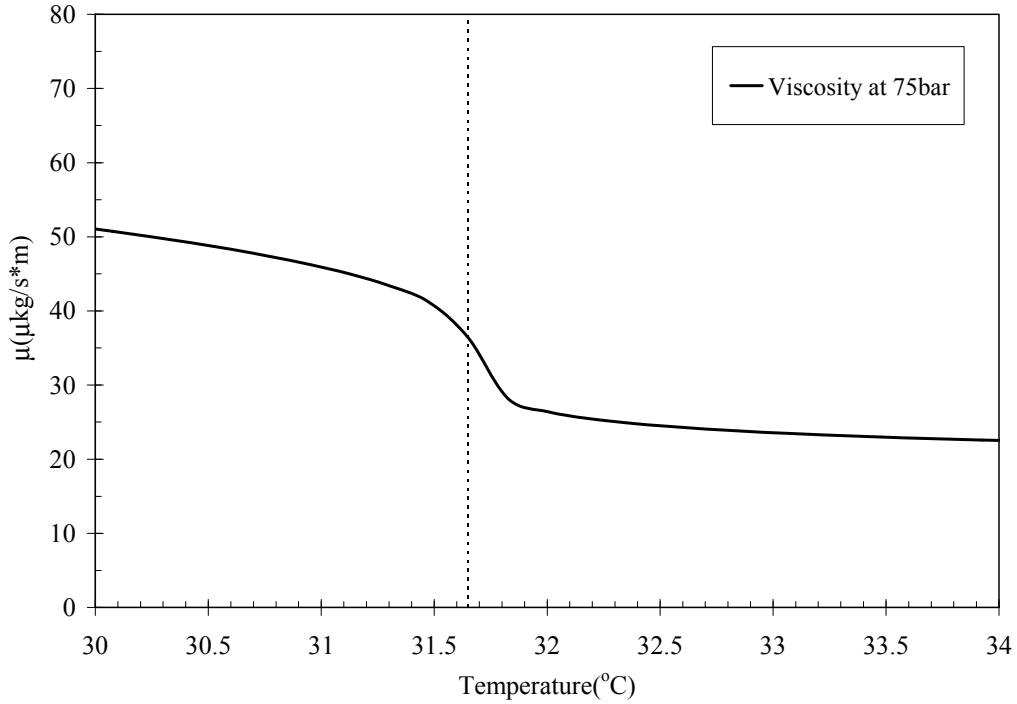

Figure D.1: Viscosity at 75bar

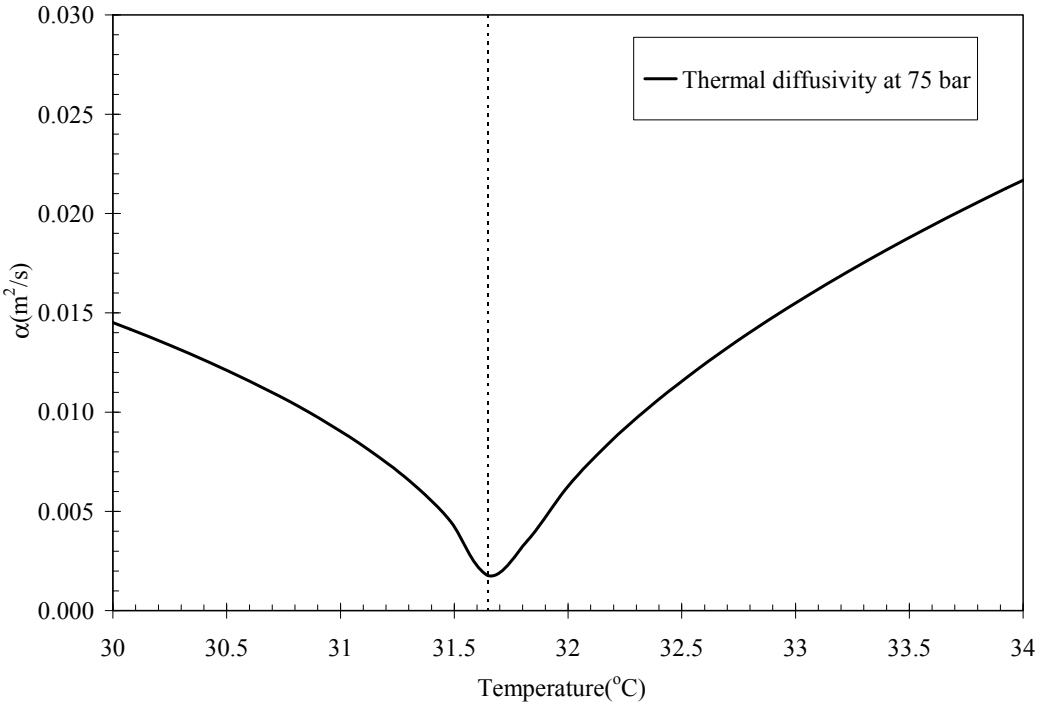

Figure D.1: Thermal diffusivity at 75bar

Table D.1: Thermophysical properties at 80bar

Temperature (°C)	Density (kg/m3)	Internal Energy (kJ/kg)	Enthalpy (kJ/kg)	Cv (J/g*K)	Cp (J/g*K)	Viscosity (uPa*s)	Therm. Cond. (W/m*K)	Phase
20	827.71	237.25	246.91	0.95097	2.9745	75.717	0.092784	liquid
21	818.55	240.16	249.93	0.95458	3.0598	73.994	0.091383	liquid
22	808.93	243.15	253.04	0.95868	3.1572	72.247	0.089961	liquid
23	798.8	246.23	256.25	0.96335	3.2693	70.468	0.088516	liquid
24	788.07	249.43	259.58	0.96869	3.3998	68.651	0.087048	liquid
25	776.64	252.76	263.06	0.97486	3.5541	66.785	0.085557	liquid
26	764.38	256.23	266.7	0.9821	3.74	64.859	0.084047	liquid
27	751.1	259.9	270.55	0.99075	3.97	62.855	0.082524	liquid
28	736.53	263.8	274.66	1.0013	4.2646	60.748	0.081004	liquid
29	720.29	268.01	279.11	1.0146	4.6595	58.502	0.07952	liquid
30	701.72	272.63	284.04	1.0318	5.2214	56.059	0.078142	liquid
31	679.73	277.89	289.66	1.055	6.0894	53.32	0.077022	supercritical
32	652.12	284.16	296.42	1.088	7.6094	50.097	0.076521	supercritical
33	613.68	292.41	305.44	1.1391	10.936	45.958	0.077605	supercritical
34	546.47	306.05	320.69	1.239	22.484	39.561	0.084016	supercritical
35	419.09	333.2	352.29	1.3171	29.594	29.843	0.082512	supercritical
36	354.75	349.68	372.23	1.2117	13.824	25.988	0.062933	supercritical
37	324.02	358.65	383.34	1.1412	9.1169	24.397	0.053859	supercritical
38	304.14	364.97	391.27	1.0939	6.9703	23.46	0.048551	supercritical
39	289.49	369.94	397.58	1.0594	5.7449	22.819	0.044981	supercritical
40	277.9	374.11	402.9	1.0329	4.9501	22.345	0.042376	supercritical
41	268.31	377.74	407.56	1.0115	4.3907	21.975	0.040371	supercritical
42	260.13	380.98	411.73	0.99377	3.9744	21.678	0.038772	supercritical
43	253.01	383.92	415.54	0.97874	3.6514	21.434	0.037462	supercritical
44	246.71	386.63	419.05	0.96574	3.3931	21.229	0.036368	supercritical
45	241.05	389.15	422.34	0.95432	3.1813	21.054	0.035439	supercritical
46	235.92	391.52	425.43	0.94416	3.0043	20.905	0.03464	supercritical
47	231.23	393.76	428.36	0.93505	2.8539	20.776	0.033947	supercritical
48	226.91	395.89	431.14	0.9268	2.7244	20.663	0.03334	supercritical
49	222.91	397.92	433.81	0.91928	2.6117	20.565	0.032805	supercritical
50	219.18	399.87	436.37	0.91238	2.5125	20.479	0.03233	supercritical
51	215.7	401.75	438.84	0.90604	2.4246	20.403	0.031908	supercritical
52	212.42	403.56	441.22	0.90018	2.3461	20.336	0.031529	supercritical
53	209.33	405.32	443.53	0.89475	2.2756	20.277	0.031189	supercritical
54	206.41	407.02	445.78	0.88971	2.2118	20.226	0.030883	supercritical
55	203.64	408.68	447.96	0.88501	2.1538	20.18	0.030607	supercritical
56	201.01	410.29	450.09	0.88063	2.1009	20.14	0.030357	supercritical
57	198.5	411.86	452.16	0.87654	2.0524	20.105	0.03013	supercritical
58	196.11	413.4	454.19	0.87271	2.0078	20.075	0.029924	supercritical
59	193.82	414.9	456.18	0.86913	1.9666	20.049	0.029737	supercritical
60	191.62	416.38	458.13	0.86577	1.9284	20.026	0.029567	supercritical
61	189.52	417.82	460.04	0.86262	1.893	20.007	0.029412	supercritical

62	187.49	419.24	461.91	0.85966	1.86	19.991	0.029271	supercritical
63	185.54	420.64	463.76	0.85687	1.8291	19.978	0.029142	supercritical
64	183.66	422.01	465.57	0.85425	1.8003	19.968	0.029026	supercritical
65	181.84	423.37	467.36	0.85178	1.7733	19.96	0.02892	supercritical
66	180.09	424.7	469.12	0.84945	1.7478	19.954	0.028823	supercritical
67	178.4	426.01	470.85	0.84725	1.7239	19.95	0.028736	supercritical
68	176.76	427.31	472.57	0.84518	1.7014	19.949	0.028657	supercritical
69	175.16	428.59	474.26	0.84322	1.68	19.949	0.028586	supercritical
70	173.62	429.85	475.93	0.84137	1.6599	19.951	0.028522	supercritical
71	172.12	431.1	477.58	0.83961	1.6407	19.955	0.028464	supercritical
72	170.67	432.34	479.21	0.83795	1.6226	19.96	0.028413	supercritical
73	169.26	433.56	480.82	0.83638	1.6054	19.966	0.028367	supercritical
74	167.88	434.77	482.42	0.83489	1.589	19.974	0.028327	supercritical
75	166.54	435.97	484	0.83348	1.5734	19.984	0.028292	supercritical
76	165.24	437.15	485.57	0.83214	1.5585	19.994	0.028262	supercritical
77	163.97	438.33	487.12	0.83087	1.5443	20.005	0.028236	supercritical
78	162.73	439.49	488.66	0.82967	1.5307	20.018	0.028214	supercritical
79	161.52	440.65	490.18	0.82852	1.5177	20.032	0.028196	supercritical
80	160.34	441.8	491.69	0.82744	1.5052	20.046	0.028182	supercritical
81	159.18	442.93	493.19	0.82641	1.4933	20.061	0.028172	supercritical
82	158.06	444.06	494.68	0.82543	1.4819	20.078	0.028164	supercritical
83	156.96	445.19	496.16	0.82451	1.471	20.095	0.02816	supercritical
84	155.88	446.3	497.62	0.82363	1.4604	20.113	0.028159	supercritical
85	154.82	447.4	499.08	0.8228	1.4503	20.131	0.02816	supercritical
86	153.79	448.5	500.52	0.82201	1.4406	20.151	0.028165	supercritical
87	152.78	449.6	501.96	0.82126	1.4312	20.171	0.028171	supercritical
88	151.79	450.68	503.38	0.82055	1.4222	20.191	0.028181	supercritical
89	150.82	451.76	504.8	0.81989	1.4136	20.213	0.028192	supercritical
90	149.87	452.83	506.21	0.81925	1.4052	20.235	0.028206	supercritical

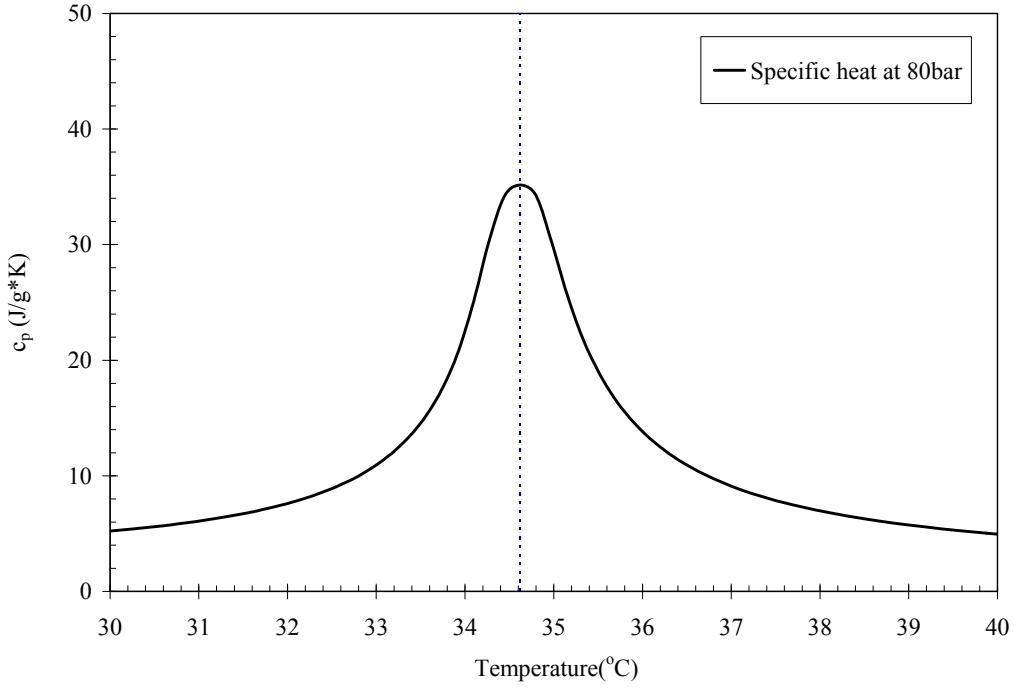

Figure D.1: Specific heat at 80bar

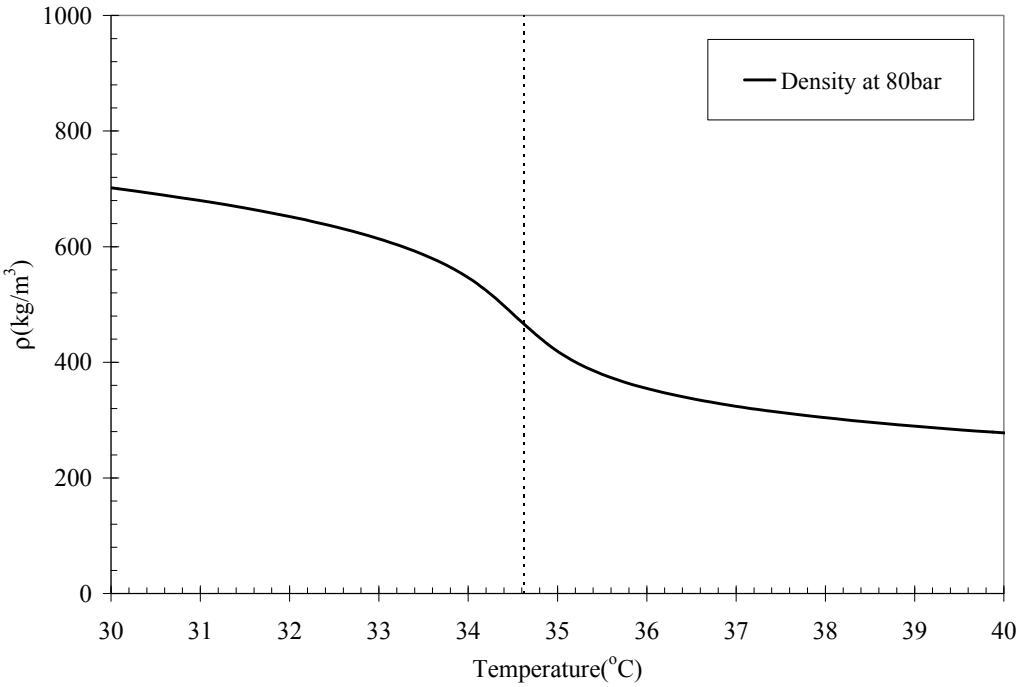

Figure D.1: Density at 80bar

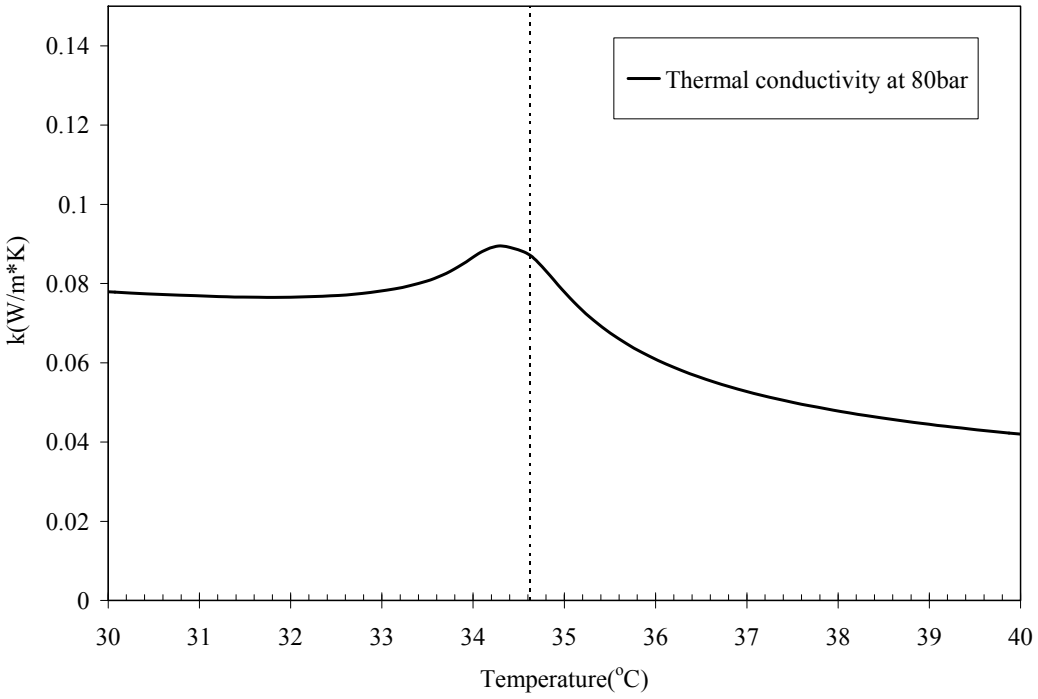

Figure D.1: Thermal conductivity at 80bar

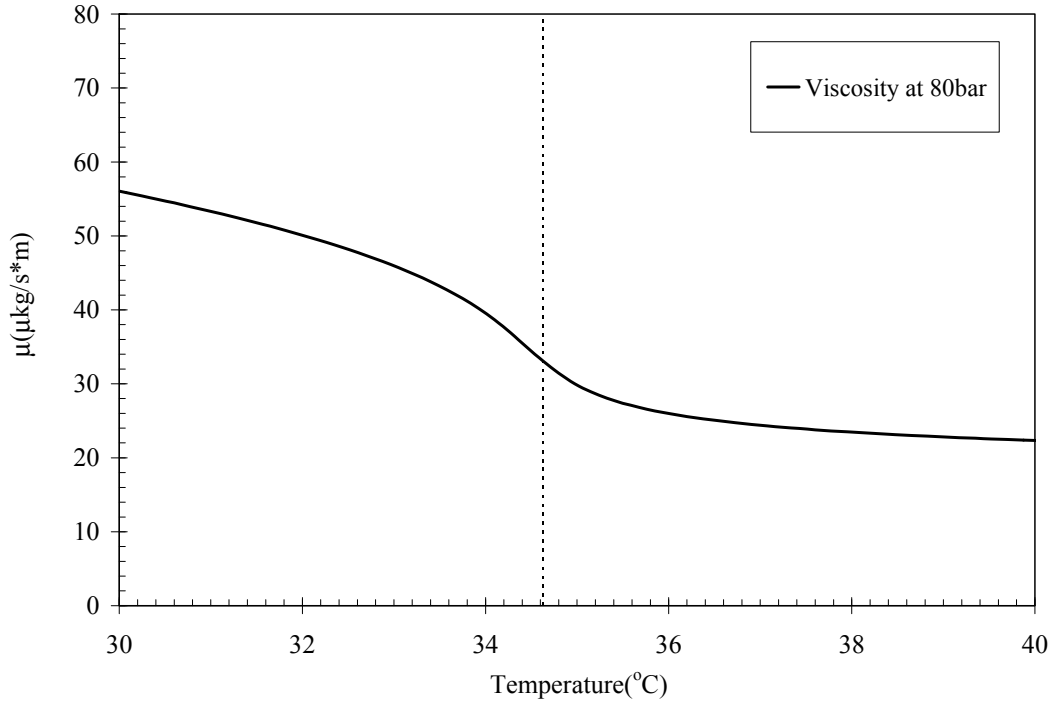

Figure D.1: Viscosity at 80bar

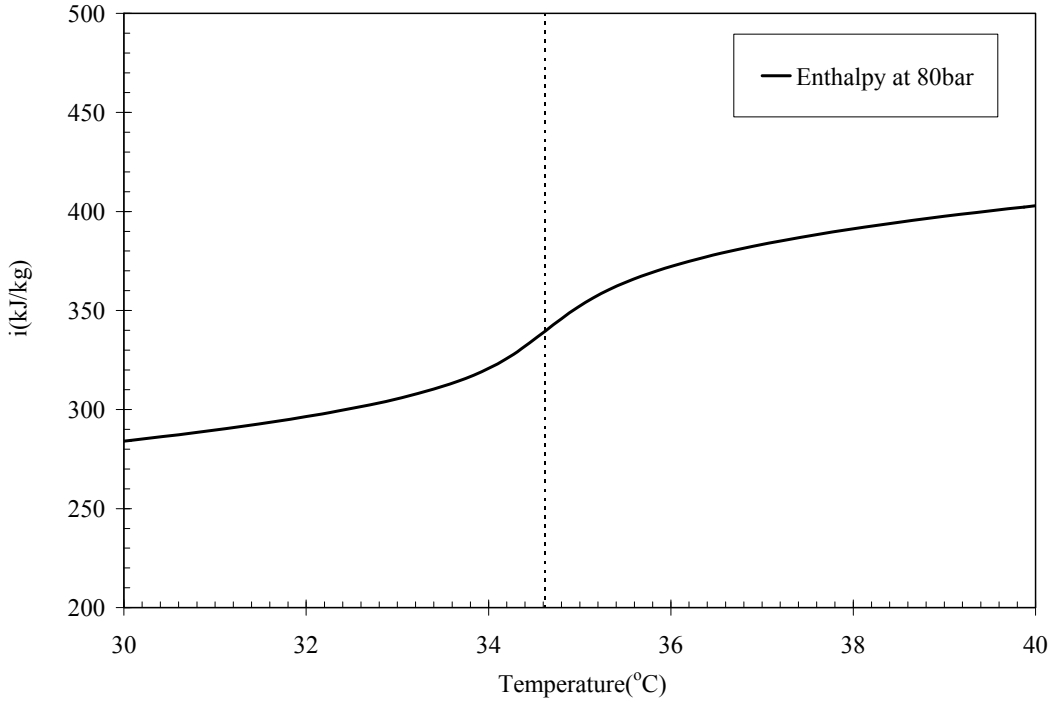

Figure D.1: Enthalpy at 80bar

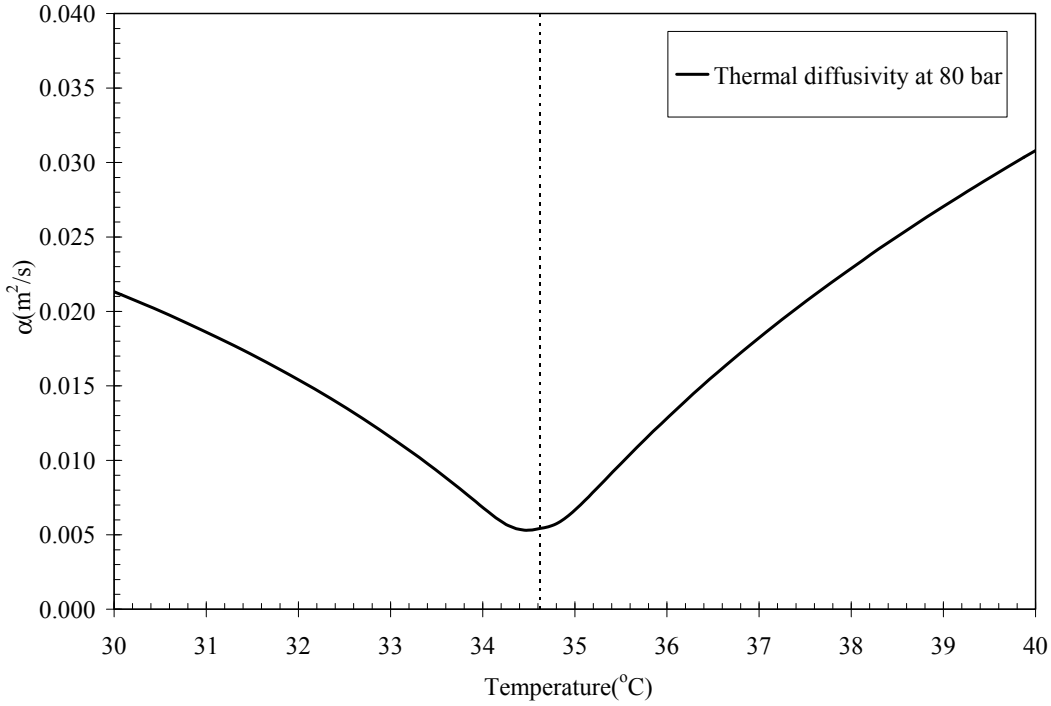

Figure D.1: Thermal diffusivity at 80bar

Table D.1: Thermophysical properties at 85bar.

Temperature (°C)	Density (kg/m3)	Internal Energy (kJ/kg)	Enthalpy (kJ/kg)	Cv (J/g*K)	Cp (J/g*K)	Viscosity (uPa*s)	Therm. Cond. (W/m*K)	Phase
20	835.8	10.365	10.812	41.612	125.91	77.292	0.094073	liquid
21	827.24	10.487	10.94	41.74	128.94	75.637	0.092725	liquid
22	818.33	10.613	11.07	41.883	132.34	73.967	0.091358	liquid
23	809.02	10.742	11.204	42.045	136.17	72.278	0.089973	liquid
24	799.26	10.875	11.343	42.226	140.52	70.566	0.088567	liquid
25	788.98	11.012	11.486	42.432	145.5	68.824	0.087142	liquid
26	778.11	11.153	11.634	42.665	151.26	67.045	0.085696	liquid
27	766.54	11.301	11.789	42.934	158.04	65.221	0.084231	liquid
28	754.15	11.455	11.951	43.248	166.16	63.341	0.08275	liquid
29	740.76	11.617	12.122	43.62	176.11	61.388	0.081263	liquid
30	726.15	11.789	12.304	44.07	188.7	59.343	0.079784	liquid
31	709.94	11.973	12.5	44.626	205.2	57.174	0.078341	supercritical
32	691.62	12.175	12.716	45.327	227.79	54.836	0.07699	supercritical
33	670.35	12.401	12.959	46.229	260.37	52.262	0.07583	supercritical
34	644.7	12.662	13.243	47.412	310.71	49.339	0.075046	supercritical
35	612.12	12.981	13.592	48.983	395.38	45.881	0.07495	supercritical
36	567.77	13.398	14.057	51.125	551.99	41.583	0.076002	supercritical
37	504.09	13.992	14.734	53.551	794.87	36.126	0.077506	supercritical
38	434.5	14.682	15.543	53.728	767.77	31.017	0.072484	supercritical
39	385.19	15.224	16.195	51.585	543.03	27.897	0.063115	supercritical
40	353.91	15.603	16.66	49.447	401.14	26.134	0.056118	supercritical
41	332.01	15.89	17.017	47.787	319.11	25.001	0.051266	supercritical
42	315.42	16.122	17.308	46.501	266.96	24.203	0.047721	supercritical
43	302.16	16.318	17.557	45.473	231.23	23.605	0.045014	supercritical
44	291.17	16.489	17.774	44.626	205.33	23.136	0.042875	supercritical
45	281.81	16.642	17.969	43.91	185.72	22.758	0.041138	supercritical
46	273.68	16.78	18.147	43.291	170.36	22.447	0.039699	supercritical
47	266.49	16.907	18.311	42.748	158	22.185	0.038486	supercritical
48	260.06	17.025	18.464	42.266	147.84	21.962	0.03745	supercritical
49	254.25	17.136	18.607	41.832	139.33	21.771	0.036555	supercritical
50	248.95	17.24	18.743	41.438	132.09	21.604	0.035775	supercritical
51	244.08	17.339	18.872	41.08	125.86	21.459	0.03509	supercritical
52	239.58	17.433	18.995	40.751	120.44	21.332	0.034484	supercritical
53	235.4	17.524	19.113	40.448	115.68	21.219	0.033945	supercritical
54	231.5	17.61	19.226	40.168	111.46	21.119	0.033464	supercritical
55	227.84	17.694	19.336	39.908	107.69	21.031	0.033032	supercritical
56	224.4	17.775	19.442	39.667	104.31	20.952	0.032643	supercritical
57	221.15	17.853	19.545	39.443	101.26	20.882	0.032291	supercritical
58	218.07	17.929	19.644	39.234	98.487	20.82	0.031973	supercritical
59	215.15	18.003	19.742	39.039	95.961	20.764	0.031684	supercritical
60	212.37	18.075	19.836	38.857	93.647	20.714	0.031422	supercritical
61	209.72	18.145	19.929	38.686	91.521	20.67	0.031182	supercritical

62	207.19	18.214	20.02	38.526	89.561	20.631	0.030964	supercritical
63	204.77	18.281	20.108	38.376	87.747	20.597	0.030764	supercritical
64	202.45	18.347	20.195	38.235	86.063	20.566	0.030582	supercritical
65	200.22	18.412	20.28	38.103	84.497	20.54	0.030416	supercritical
66	198.07	18.475	20.364	37.979	83.036	20.517	0.030263	supercritical
67	196	18.538	20.446	37.862	81.67	20.497	0.030124	supercritical
68	194.01	18.599	20.527	37.751	80.389	20.48	0.029996	supercritical
69	192.09	18.66	20.607	37.647	79.187	20.466	0.02988	supercritical
70	190.23	18.719	20.686	37.549	78.055	20.454	0.029773	supercritical
71	188.44	18.778	20.763	37.456	76.989	20.445	0.029676	supercritical
72	186.7	18.836	20.84	37.368	75.982	20.438	0.029587	supercritical
73	185.01	18.893	20.915	37.285	75.03	20.432	0.029507	supercritical
74	183.37	18.95	20.99	37.206	74.128	20.429	0.029433	supercritical
75	181.79	19.006	21.064	37.132	73.273	20.428	0.029367	supercritical
76	180.25	19.061	21.137	37.061	72.461	20.428	0.029307	supercritical
77	178.75	19.116	21.209	36.994	71.688	20.43	0.029253	supercritical
78	177.29	19.17	21.28	36.93	70.953	20.434	0.029205	supercritical
79	175.87	19.223	21.351	36.87	70.251	20.439	0.029162	supercritical
80	174.49	19.277	21.42	36.813	69.583	20.445	0.029125	supercritical
81	173.14	19.329	21.49	36.758	68.944	20.452	0.029091	supercritical
82	171.82	19.381	21.558	36.706	68.333	20.461	0.029063	supercritical
83	170.54	19.433	21.626	36.657	67.748	20.471	0.029038	supercritical
84	169.29	19.484	21.694	36.611	67.189	20.481	0.029017	supercritical
85	168.07	19.535	21.761	36.566	66.652	20.493	0.029	supercritical
86	166.87	19.585	21.827	36.524	66.137	20.506	0.028986	supercritical
87	165.7	19.635	21.893	36.484	65.643	20.52	0.028976	supercritical
88	164.56	19.685	21.958	36.446	65.168	20.534	0.028969	supercritical
89	163.44	19.735	22.023	36.41	64.712	20.55	0.028965	supercritical
90	162.35	19.784	22.088	36.376	64.273	20.566	0.028963	supercritical

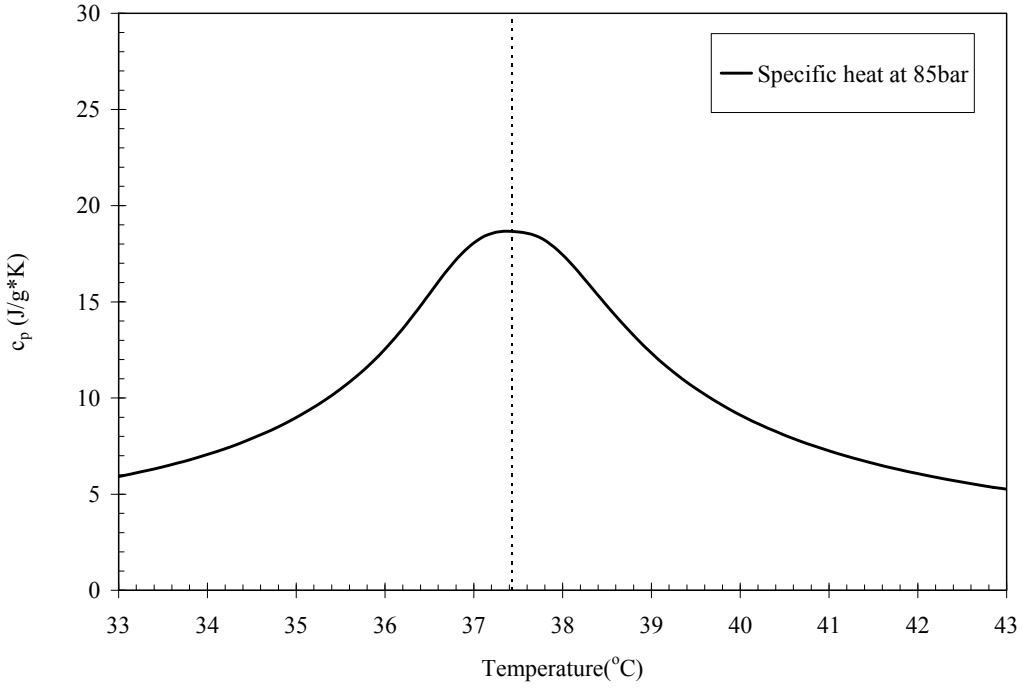

Figure D.1: Specific heat at 85bar

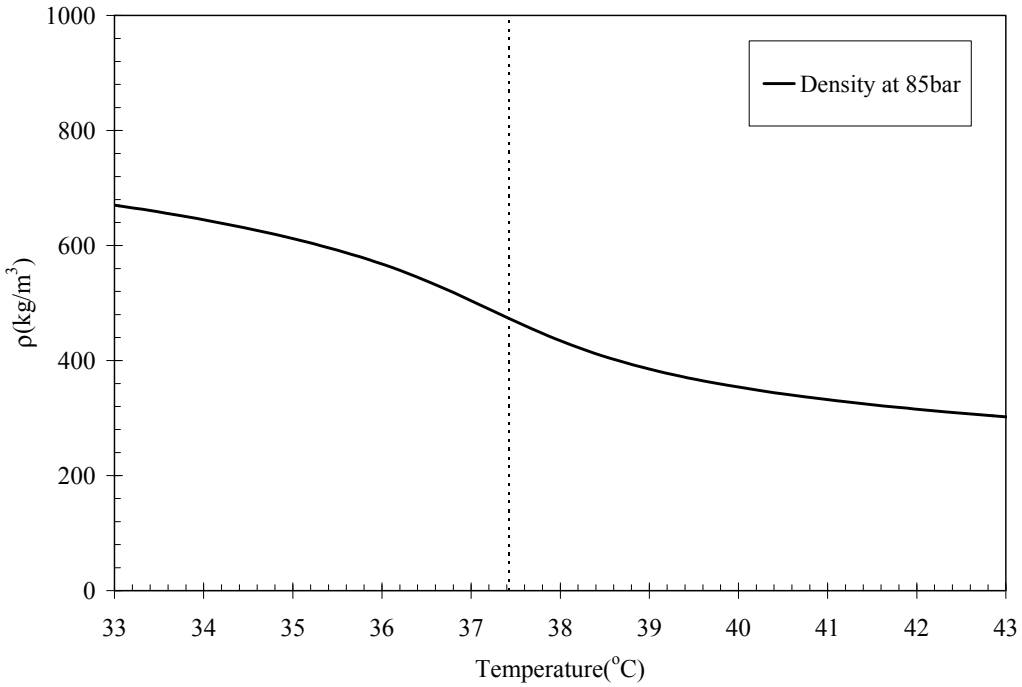

Figure D.1: Density at 85bar

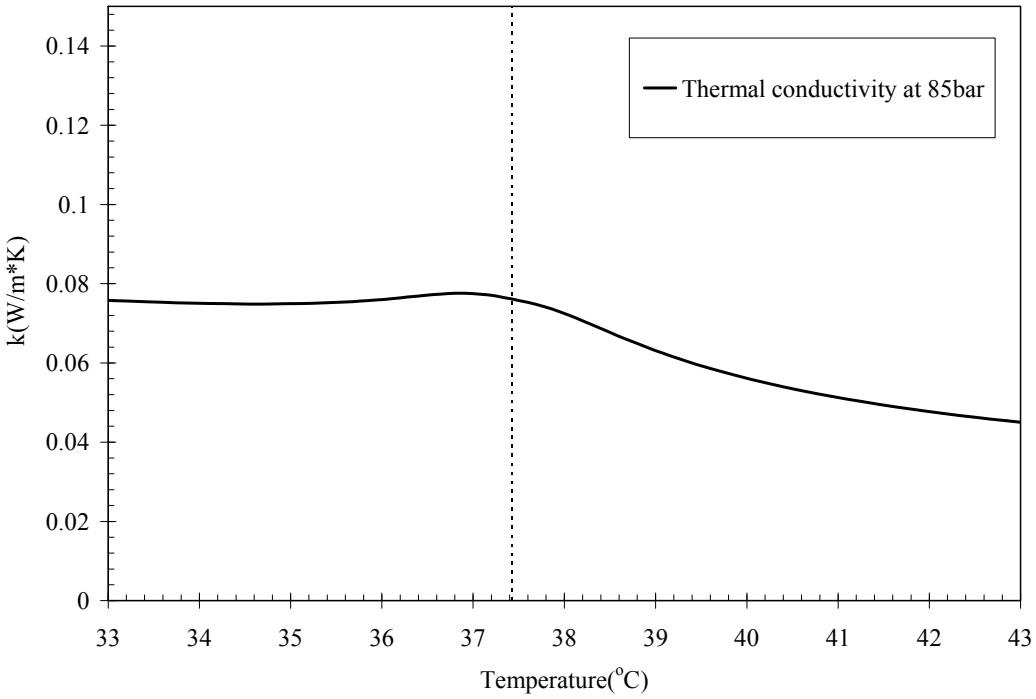

Figure D.1: Thermal conductivity at 85bar

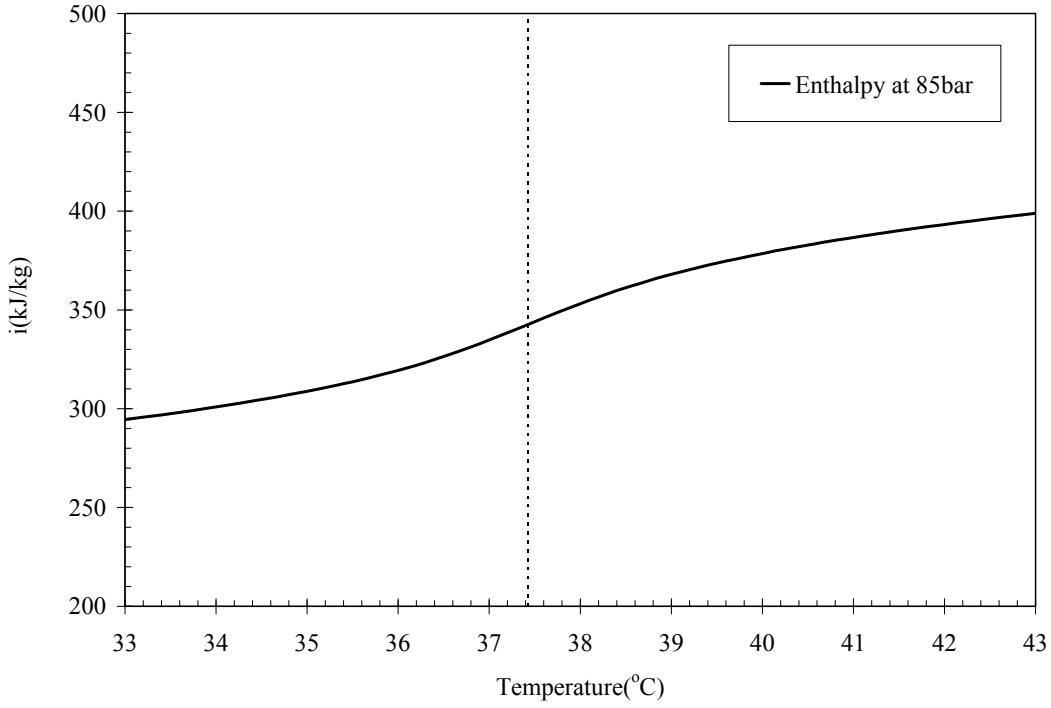

Figure D.2: Enthalpy at 85bar

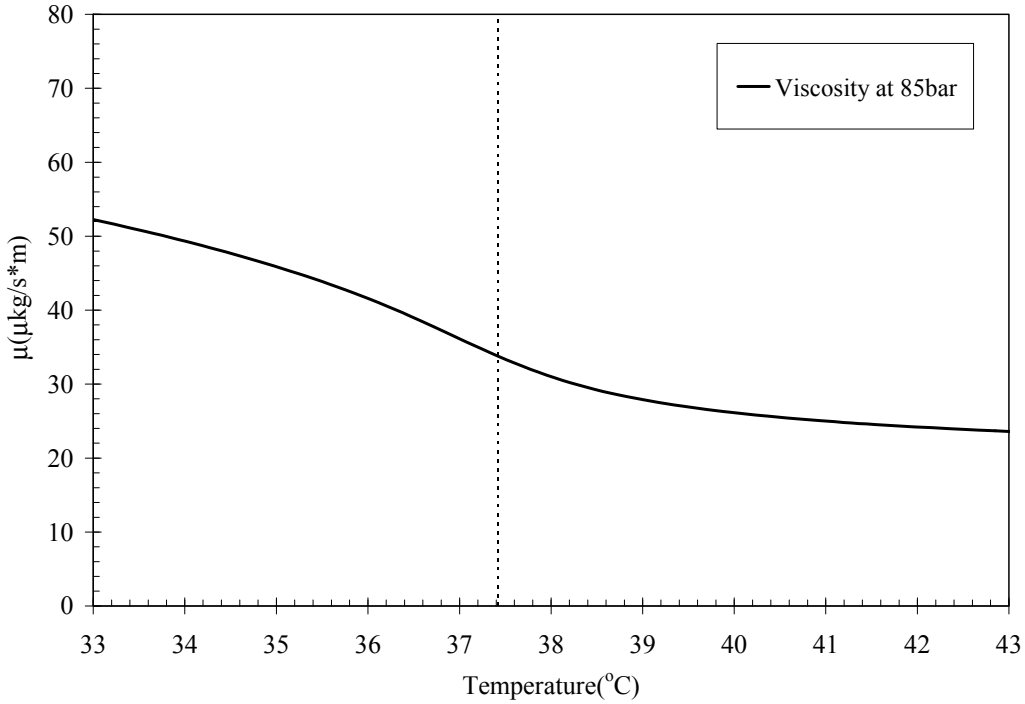

Figure D.1: Viscosity at 85bar

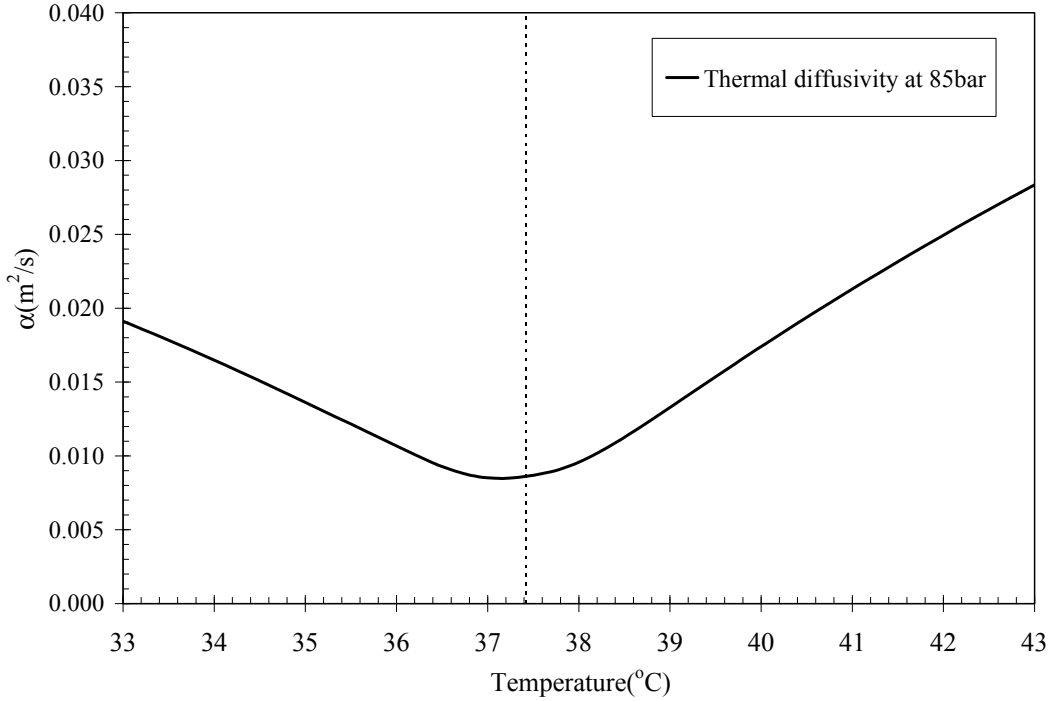

Figure D.1: Thermal diffusivity at 85bar

Table D.1: Thermophysical properties at 90bar

Temperature (°C)	Density (kg/m3)	Internal Energy (kJ/kg)	Enthalpy (kJ/kg)	Cv (J/g*K)	Cp (J/g*K)	Viscosity (uPa*s)	Therm. Cond. (W/m*K)	Phase
20	843.17	10.294	10.764	41.42	121.8	78.767	0.095291	liquid
21	835.12	10.413	10.887	41.524	124.31	77.166	0.093987	liquid
22	826.78	10.534	11.013	41.64	127.09	75.558	0.092669	liquid
23	818.11	10.657	11.141	41.77	130.17	73.938	0.091335	liquid
24	809.08	10.784	11.273	41.914	133.61	72.304	0.089985	liquid
25	799.65	10.913	11.409	42.075	137.46	70.652	0.088617	liquid
26	789.77	11.047	11.548	42.254	141.82	68.978	0.087232	liquid
27	779.38	11.184	11.692	42.455	146.78	67.276	0.085828	liquid
28	768.41	11.327	11.842	42.683	152.49	65.54	0.084408	liquid
29	756.75	11.474	11.998	42.942	159.16	63.763	0.082972	liquid
30	744.31	11.629	12.161	43.243	167.08	61.934	0.081525	liquid
31	730.91	11.791	12.332	43.595	176.7	60.041	0.080076	supercritical
32	716.36	11.962	12.515	44.014	188.65	58.066	0.078637	supercritical
33	700.34	12.145	12.711	44.517	203.89	55.986	0.077231	supercritical
34	682.47	12.344	12.924	45.13	223.84	53.768	0.075896	supercritical
35	662.13	12.563	13.161	45.878	250.7	51.369	0.07469	supercritical
36	638.48	12.809	13.429	46.789	287.9	48.73	0.073697	supercritical
37	610.3	13.093	13.742	47.892	340.46	45.779	0.073005	supercritical
38	575.93	13.43	14.118	49.2	415.84	42.436	0.07269	supercritical
39	533.61	13.84	14.582	50.496	514.4	38.668	0.072523	supercritical
40	485.5	14.314	15.13	51.07	564.78	34.806	0.07059	supercritical
41	440.2	14.783	15.683	50.521	530.89	31.549	0.066528	supercritical
42	403.5	15.19	16.172	49.316	443.34	29.171	0.061187	supercritical
43	375.79	15.52	16.574	48.049	363.94	27.528	0.056335	supercritical
44	354.49	15.79	16.907	46.936	306.2	26.356	0.052442	supercritical
45	337.51	16.018	17.191	45.993	264.39	25.482	0.049335	supercritical
46	323.56	16.215	17.439	45.188	233.25	24.804	0.046818	supercritical
47	311.8	16.39	17.66	44.49	209.38	24.263	0.044744	supercritical
48	301.69	16.547	17.86	43.877	190.61	23.821	0.043011	supercritical
49	292.84	16.69	18.043	43.331	175.52	23.452	0.041544	supercritical
50	285	16.822	18.212	42.838	163.15	23.141	0.040288	supercritical
51	277.97	16.945	18.37	42.392	152.84	22.874	0.039201	supercritical
52	271.61	17.06	18.518	41.983	144.12	22.643	0.038253	supercritical
53	265.8	17.168	18.658	41.608	136.65	22.442	0.037421	supercritical
54	260.47	17.271	18.792	41.263	130.19	22.265	0.036684	supercritical
55	255.55	17.369	18.919	40.943	124.54	22.109	0.03603	supercritical
56	250.97	17.463	19.041	40.647	119.56	21.971	0.035445	supercritical
57	246.7	17.553	19.158	40.372	115.14	21.848	0.03492	supercritical
58	242.7	17.639	19.271	40.117	111.19	21.738	0.034447	supercritical
59	238.94	17.723	19.381	39.879	107.64	21.639	0.034019	supercritical
60	235.39	17.804	19.487	39.657	104.42	21.551	0.033632	supercritical
61	232.04	17.883	19.59	39.45	101.51	21.471	0.033279	supercritical

62	228.85	17.959	19.69	39.256	98.848	21.4	0.032959	supercritical
63	225.83	18.033	19.787	39.075	96.411	21.336	0.032666	supercritical
64	222.94	18.106	19.883	38.905	94.171	21.278	0.032398	supercritical
65	220.19	18.177	19.976	38.747	92.105	21.226	0.032153	supercritical
66	217.55	18.246	20.067	38.597	90.192	21.179	0.031928	supercritical
67	215.03	18.314	20.156	38.457	88.418	21.138	0.031722	supercritical
68	212.61	18.381	20.244	38.326	86.766	21.1	0.031533	supercritical
69	210.28	18.446	20.33	38.202	85.226	21.067	0.031359	supercritical
70	208.04	18.51	20.414	38.085	83.785	21.037	0.031199	supercritical
71	205.88	18.574	20.497	37.975	82.435	21.011	0.031052	supercritical
72	203.8	18.636	20.579	37.871	81.168	20.988	0.030917	supercritical
73	201.79	18.697	20.66	37.772	79.975	20.968	0.030793	supercritical
74	199.84	18.757	20.739	37.679	78.85	20.951	0.030679	supercritical
75	197.96	18.817	20.818	37.591	77.789	20.936	0.030574	supercritical
76	196.14	18.875	20.895	37.508	76.785	20.924	0.030478	supercritical
77	194.37	18.933	20.971	37.429	75.834	20.914	0.030391	supercritical
78	192.66	18.991	21.046	37.354	74.933	20.906	0.03031	supercritical
79	191	19.047	21.121	37.283	74.076	20.9	0.030237	supercritical
80	189.38	19.103	21.195	37.215	73.262	20.896	0.030171	supercritical
81	187.81	19.158	21.268	37.151	72.487	20.893	0.03011	supercritical
82	186.28	19.213	21.34	37.09	71.748	20.892	0.030056	supercritical
83	184.79	19.268	21.411	37.032	71.043	20.893	0.030006	supercritical
84	183.33	19.321	21.482	36.977	70.37	20.895	0.029962	supercritical
85	181.92	19.375	21.552	36.924	69.726	20.899	0.029923	supercritical
86	180.54	19.427	21.621	36.875	69.11	20.904	0.029888	supercritical
87	179.19	19.48	21.69	36.827	68.52	20.91	0.029858	supercritical
88	177.88	19.532	21.758	36.782	67.955	20.917	0.029831	supercritical
89	176.59	19.583	21.826	36.739	67.413	20.925	0.029808	supercritical
90	175.34	19.634	21.893	36.698	66.892	20.935	0.029789	supercritical

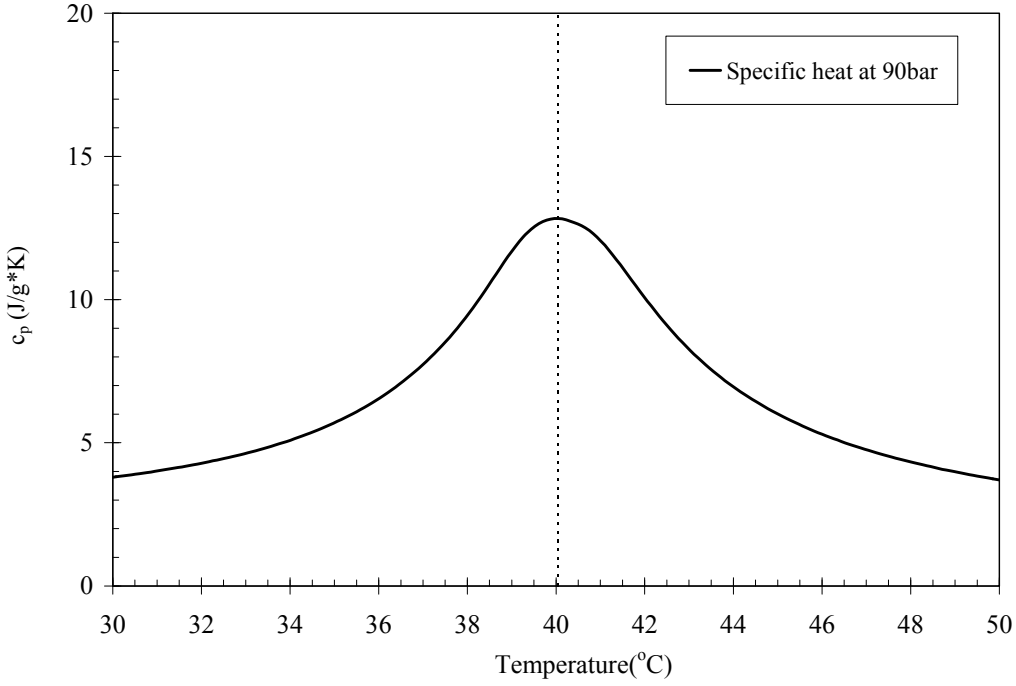

Figure D.1: Specific heat at 90bar

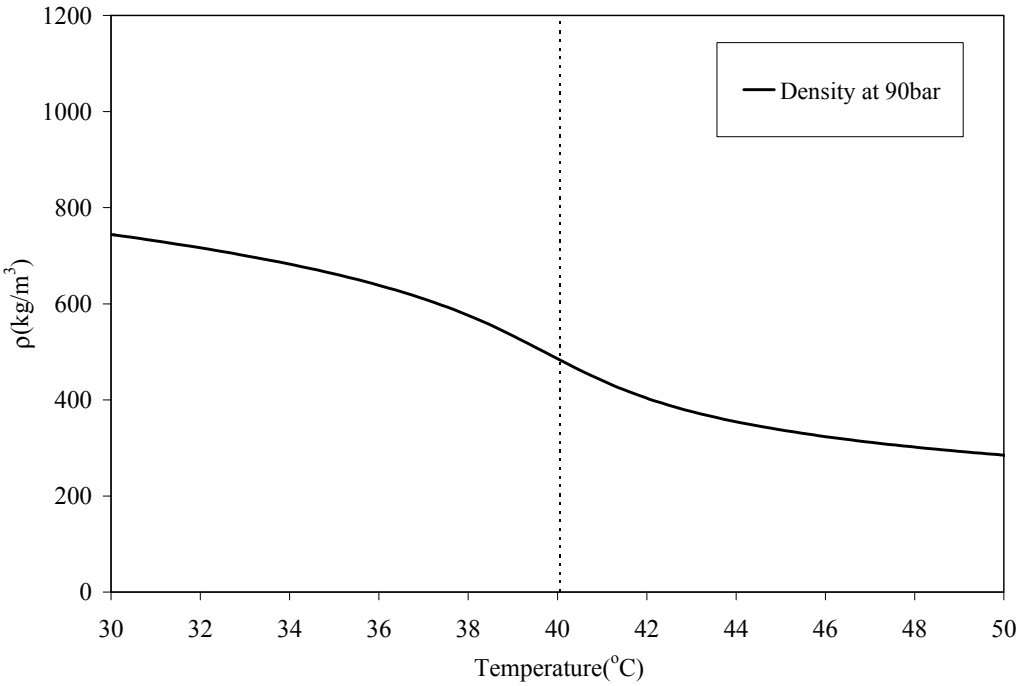

Figure D.2: Density at 90bar

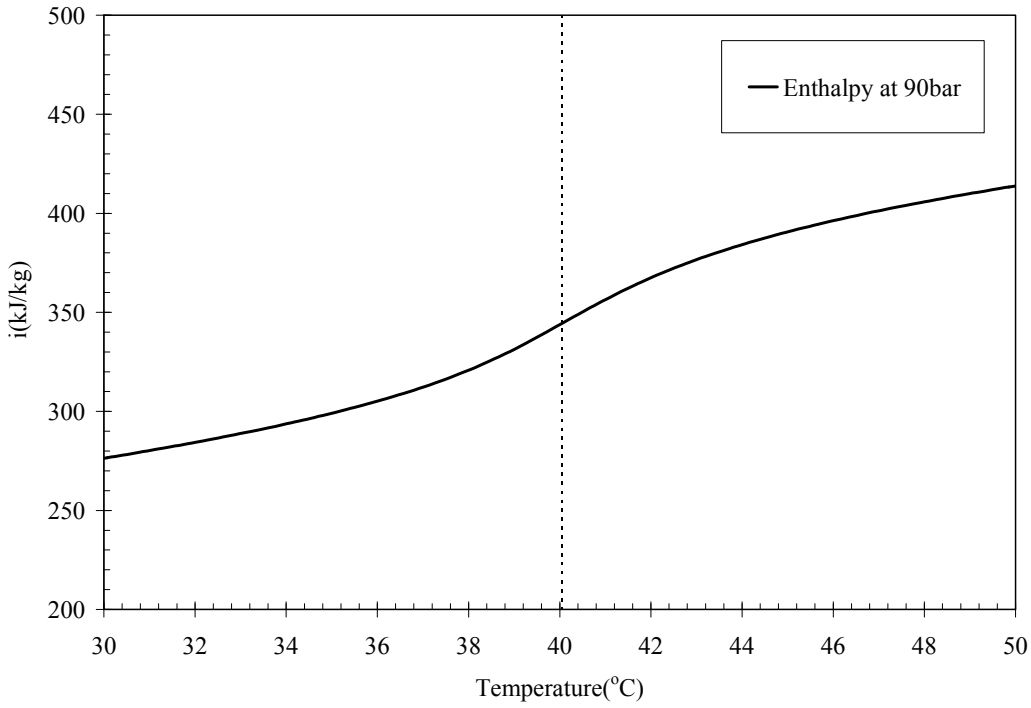

Figure D.1: Enthalpy at 90bar

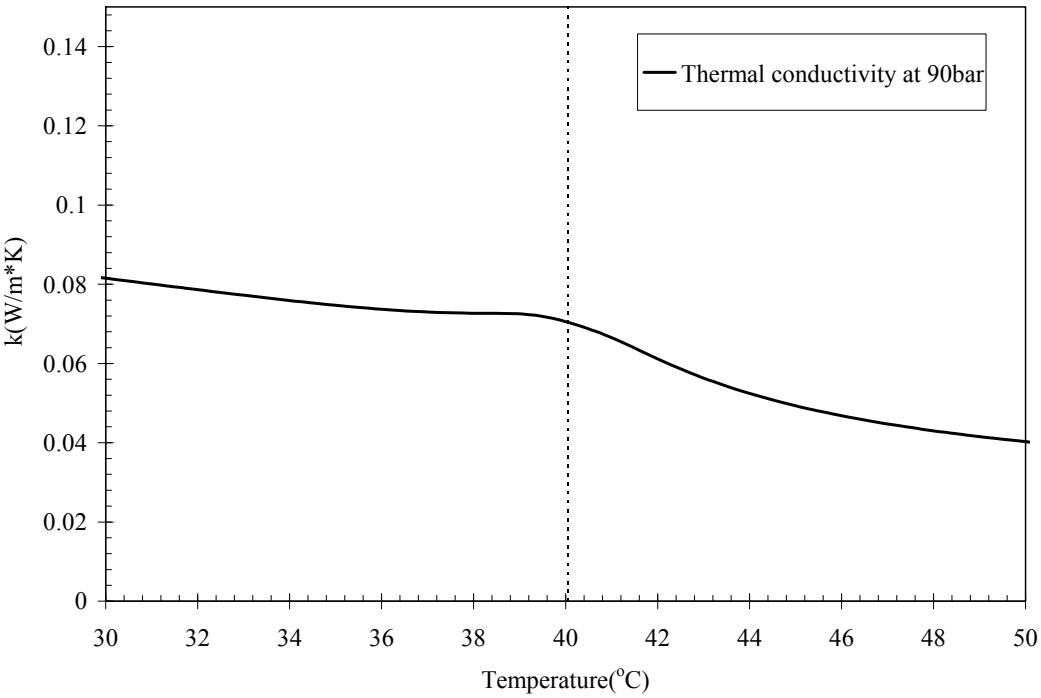

Figure D.2: Thermal conductivity at 90bar

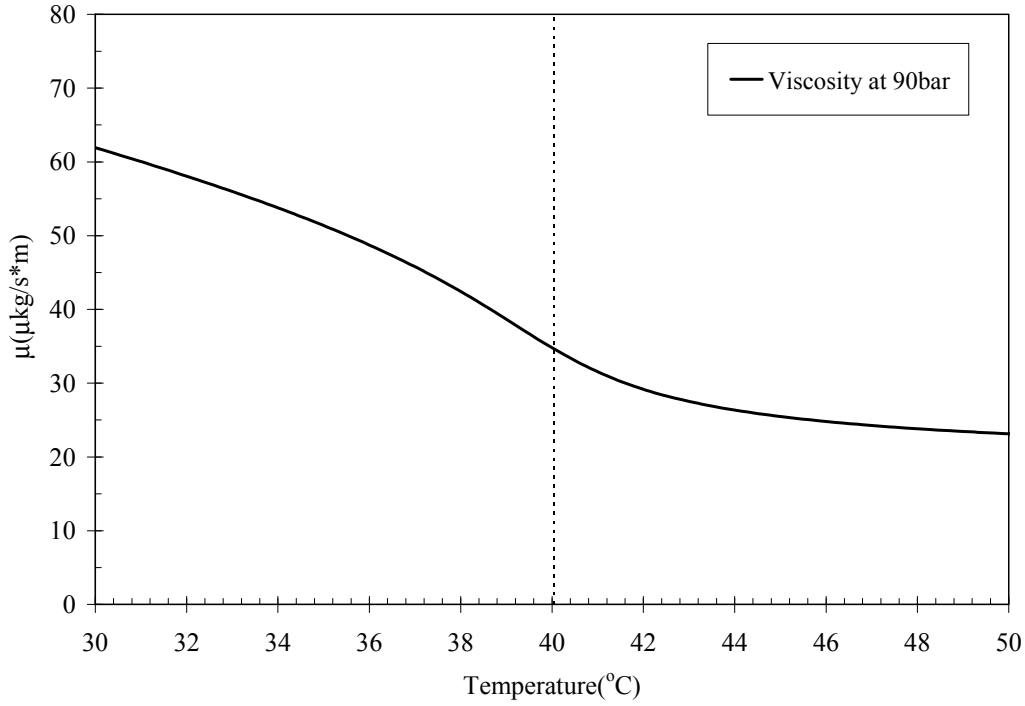

Figure D.1: Viscosity at 90bar

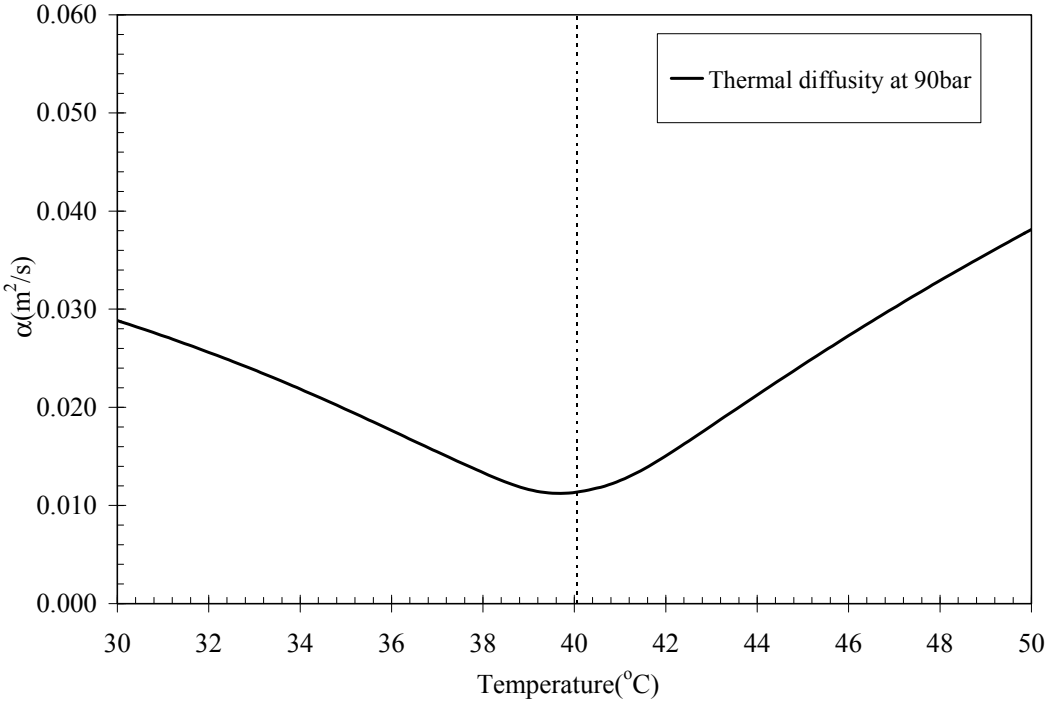

Figure D.1: Thermal diffusivity at 90bar

Appendix E – 2D FLUENT Model Results

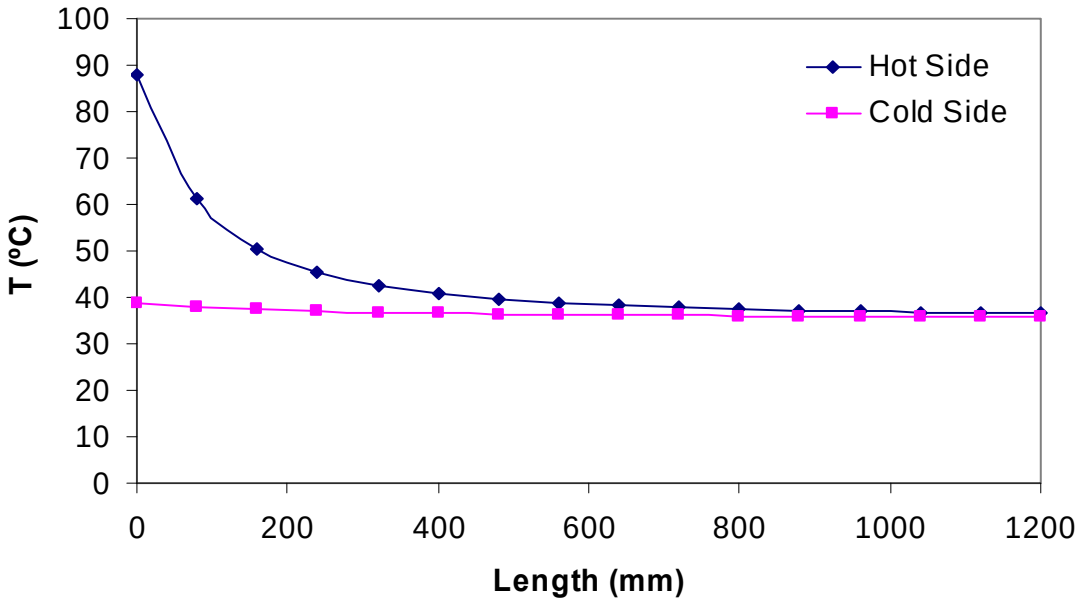

Figure E.1: Temperature Distribution of Test B6

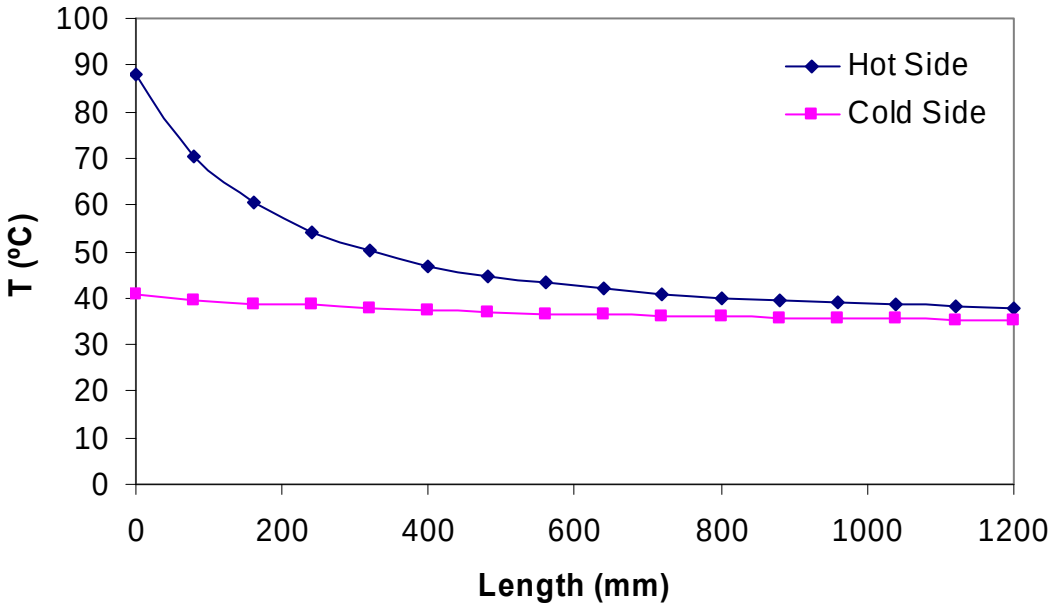

Figure E.2: Temperature Distribution of Test B7

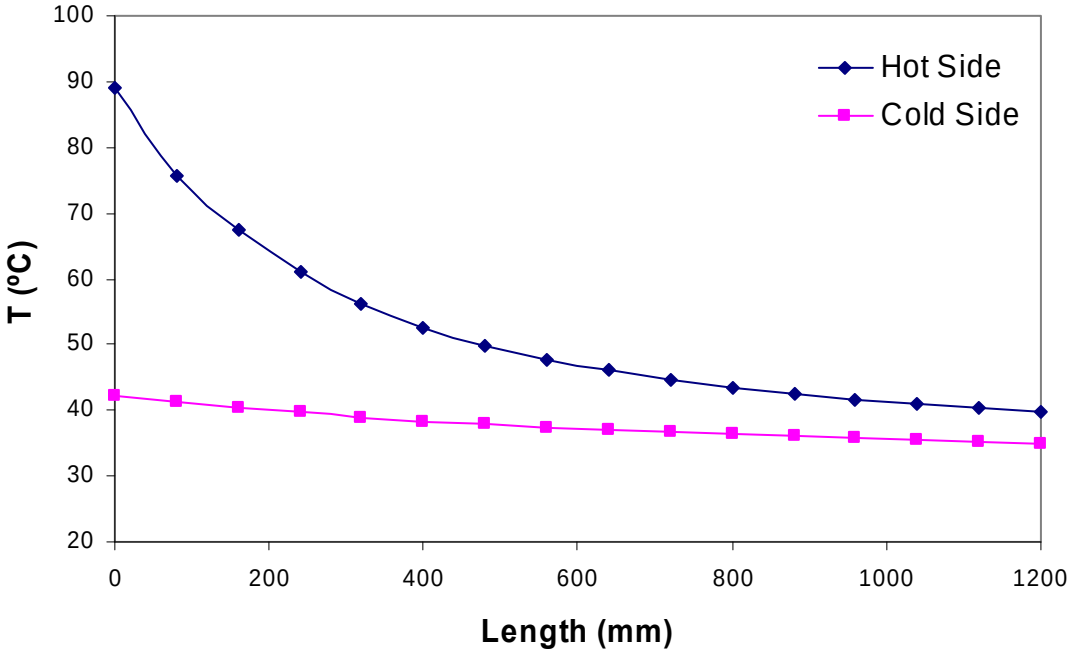

Figure E.3: Temperature Distribution of Test B8

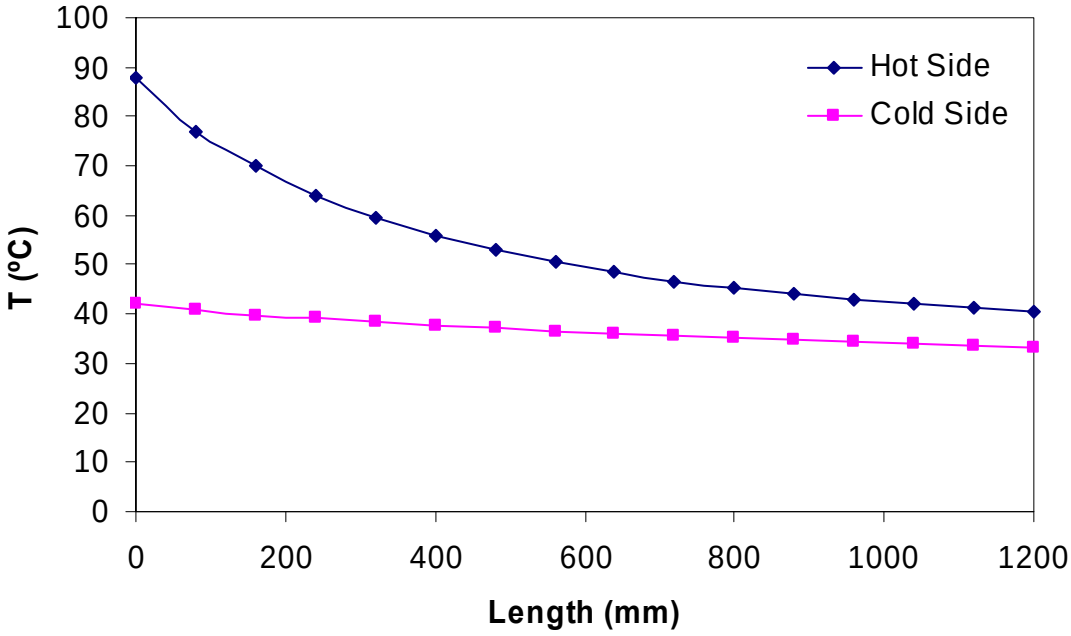

Figure E.4: Temperature Distribution of Test B9

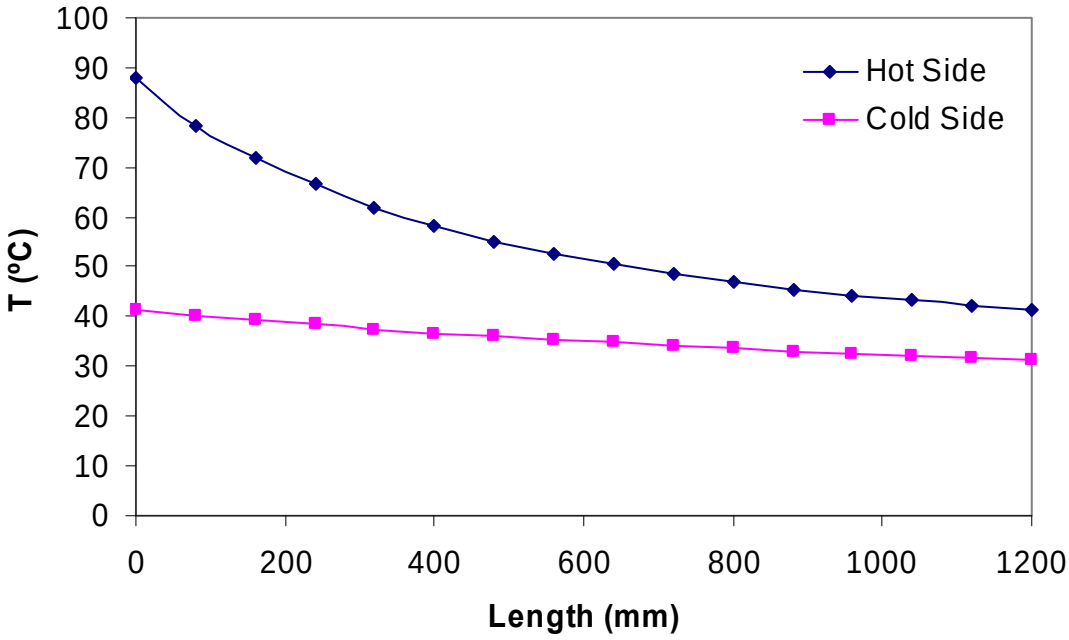

Figure E.5: Temperature Distribution for Test B10

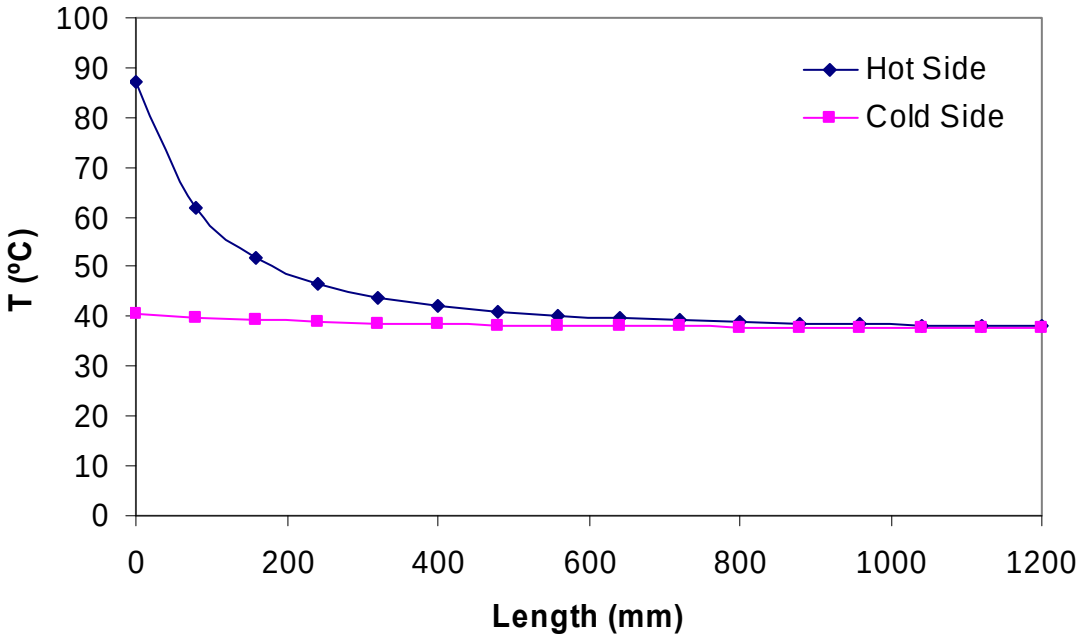

Figure E.6: Temperature Distribution for Test B11

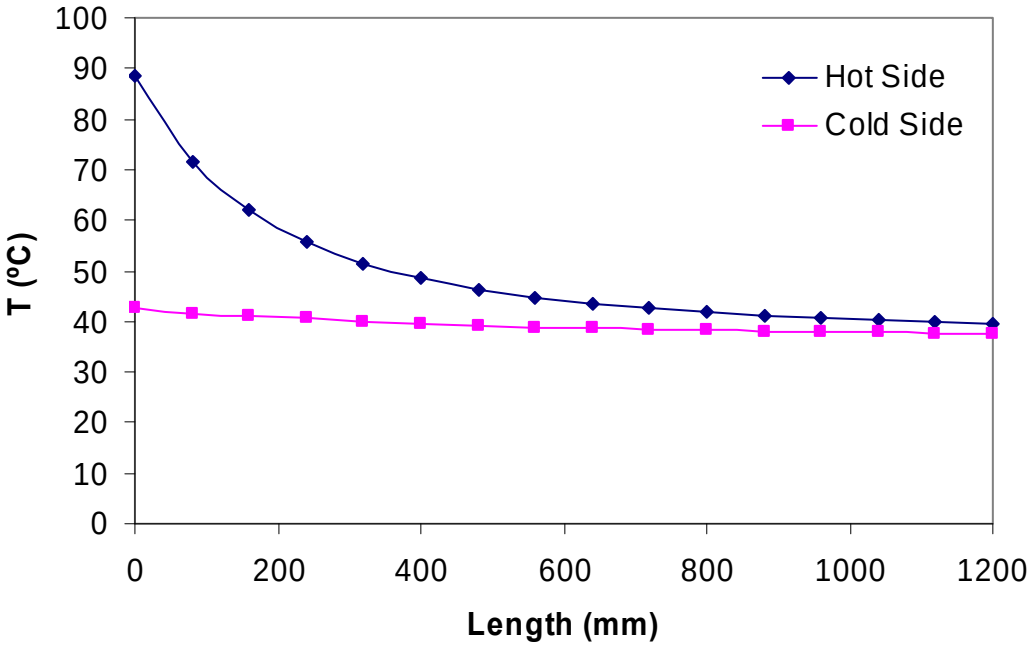

Figure E.7: Temperature Distribution for Test B12

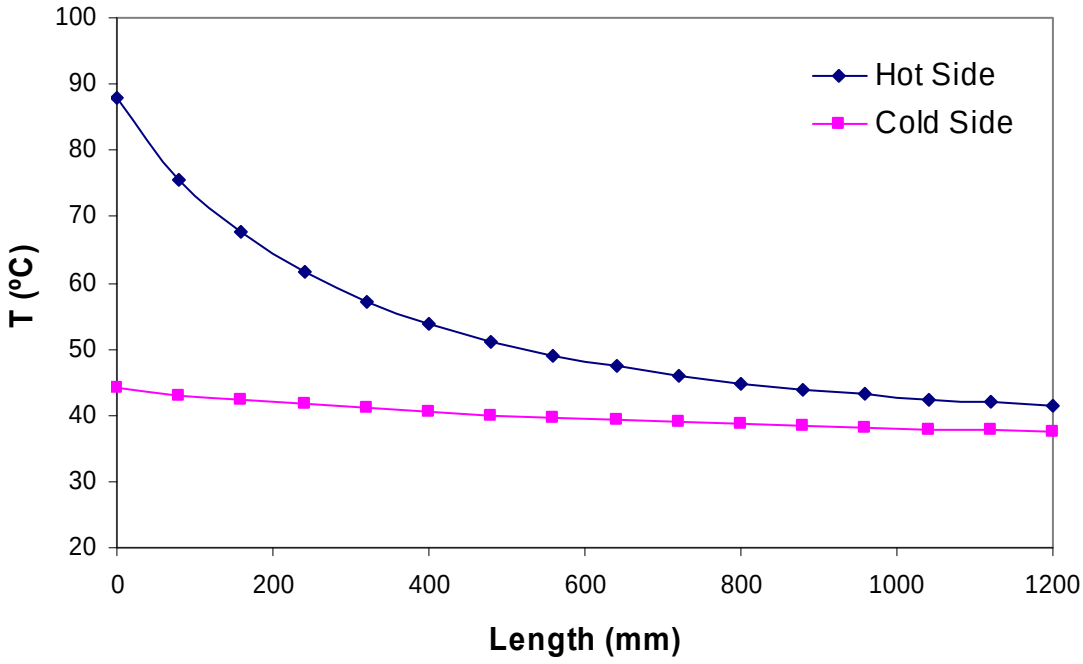

Figure E.8: Temperature Distribution for Test B13

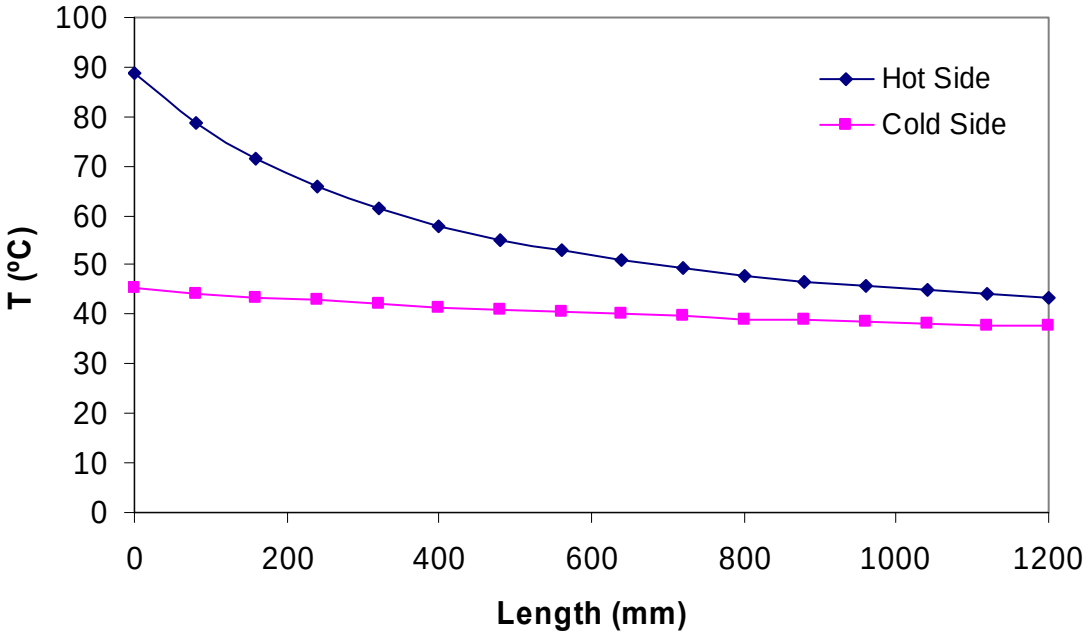

Figure E.9: Temperature Distribution for Test B14

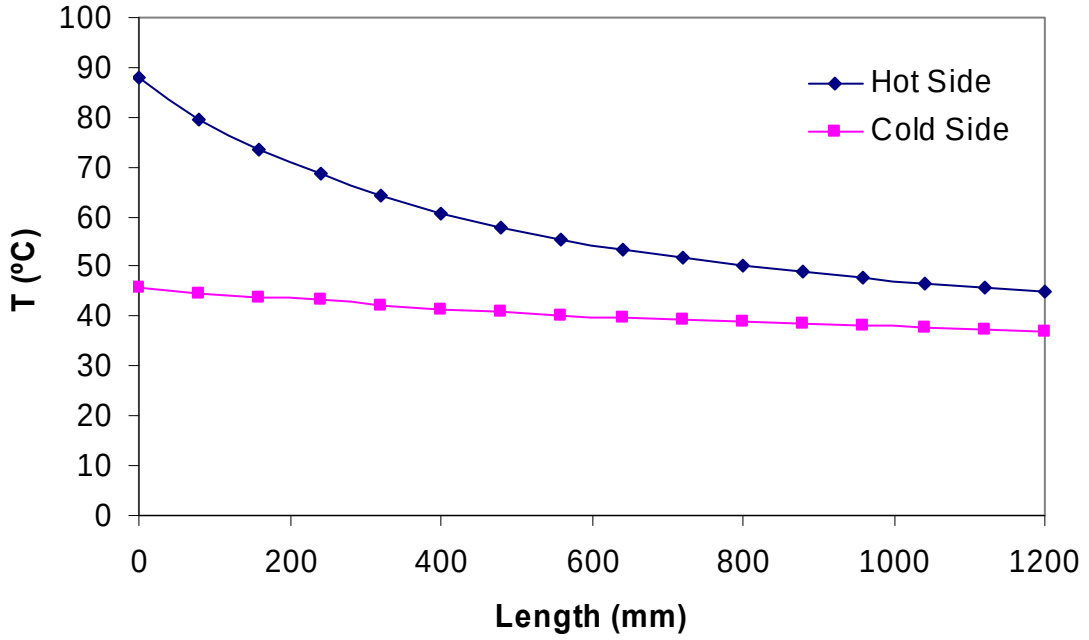

Figure E.10: Temperature Distribution for Test B15

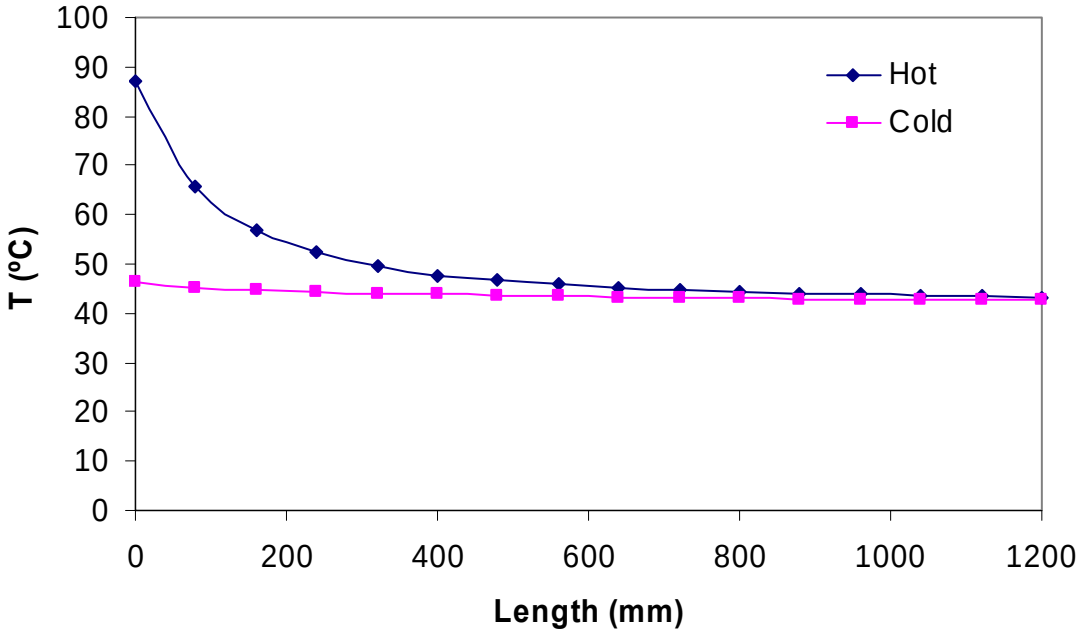

Figure E.11: Temperature Distribution for Test C5

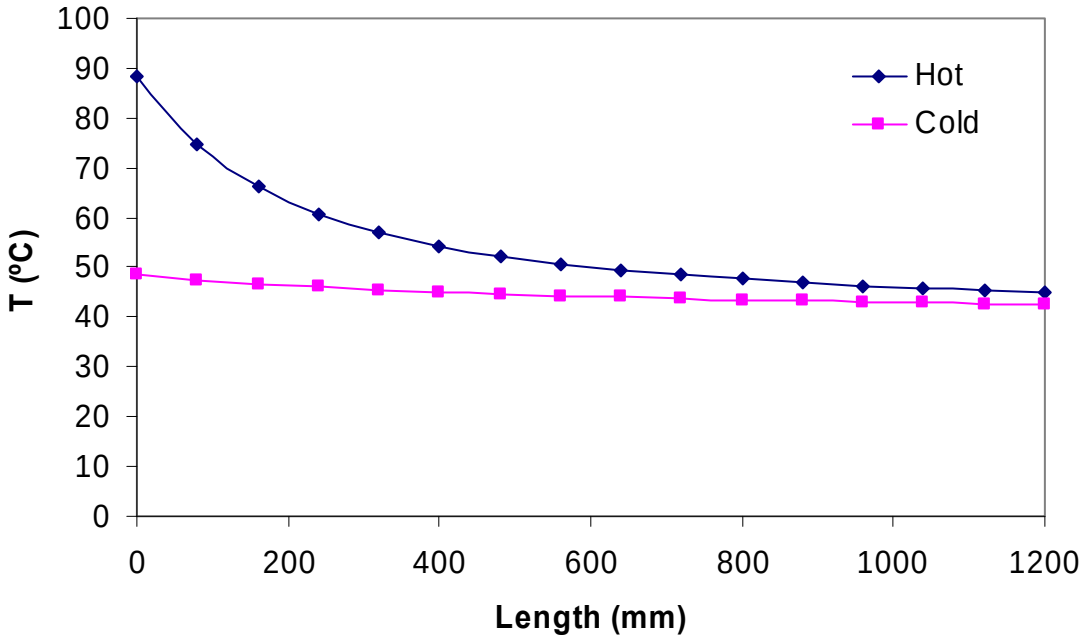

Figure E.12: Temperature Distribution for Test C6

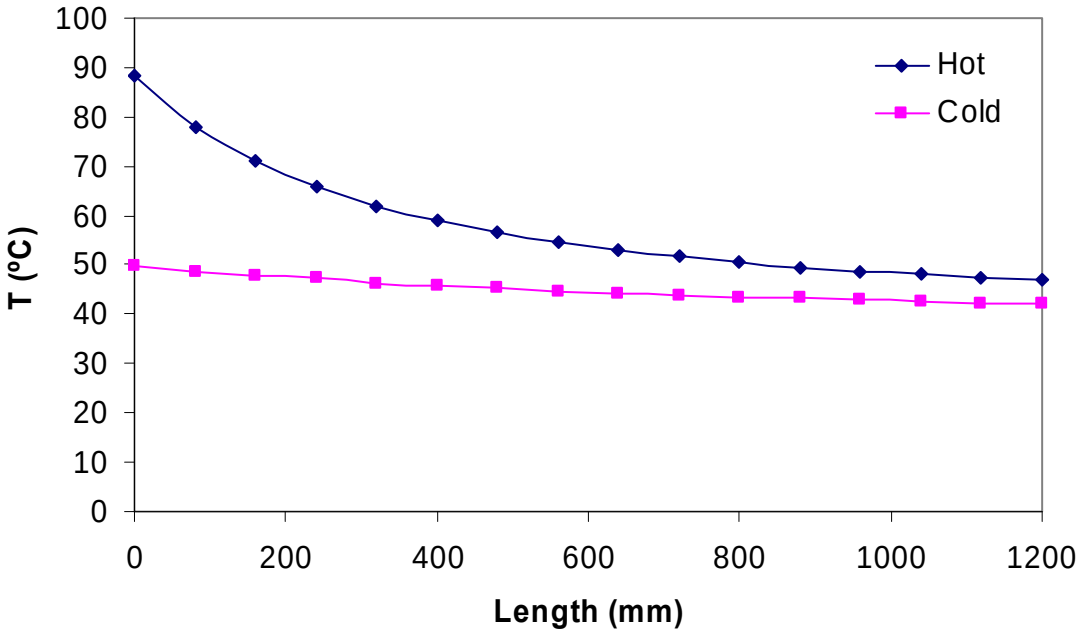

Figure E.13: Temperature Distribution for Test C7

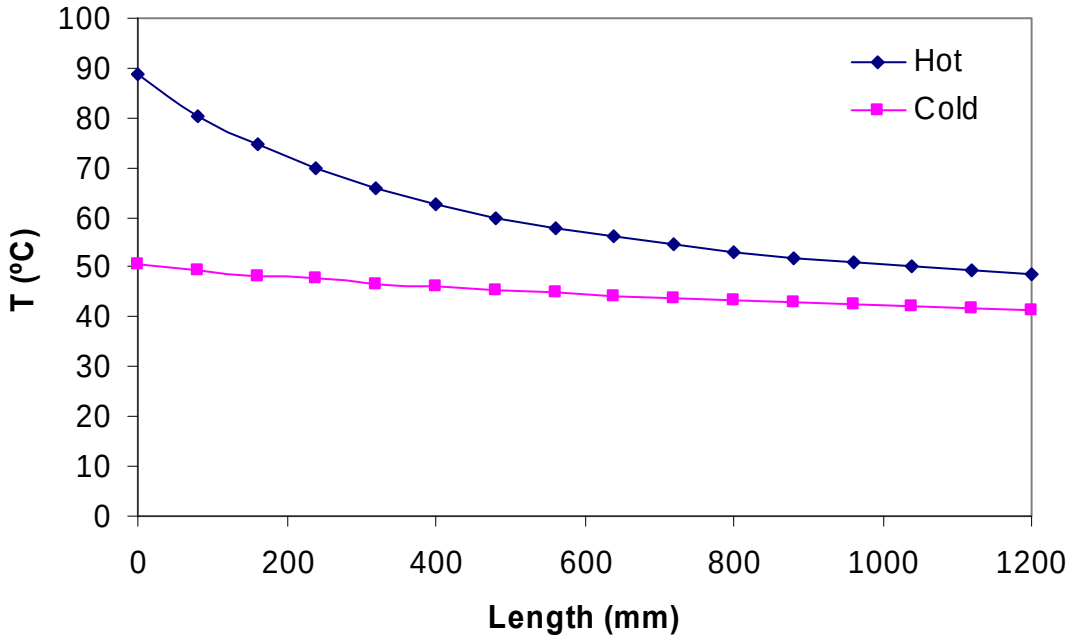

Figure E.14: Temperature Distribution for Test C8

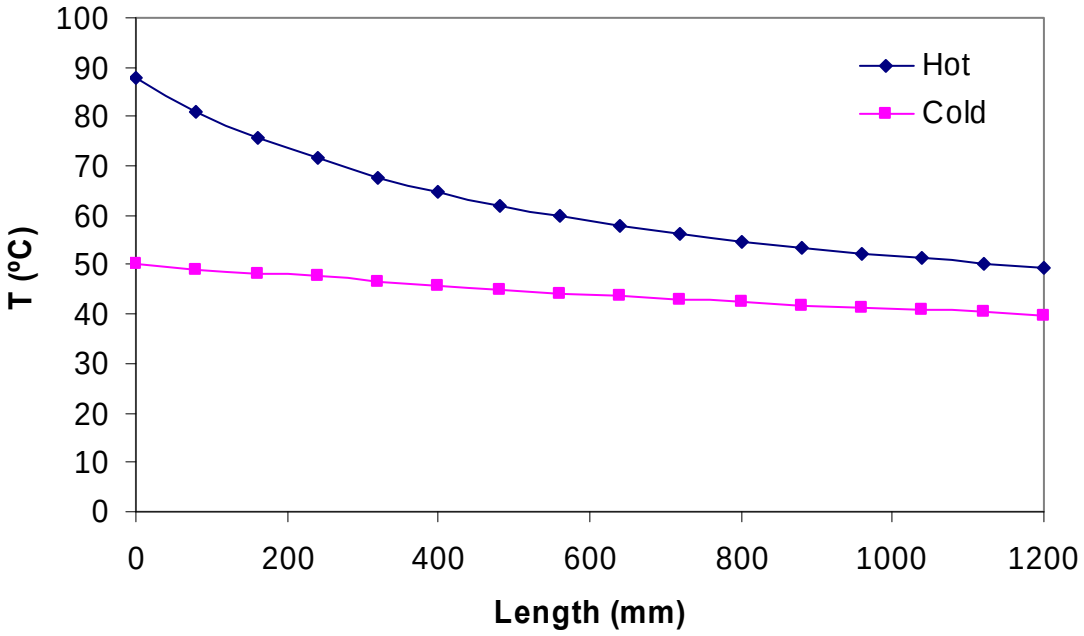

Figure E.15: Temperature Distribution for Test C9

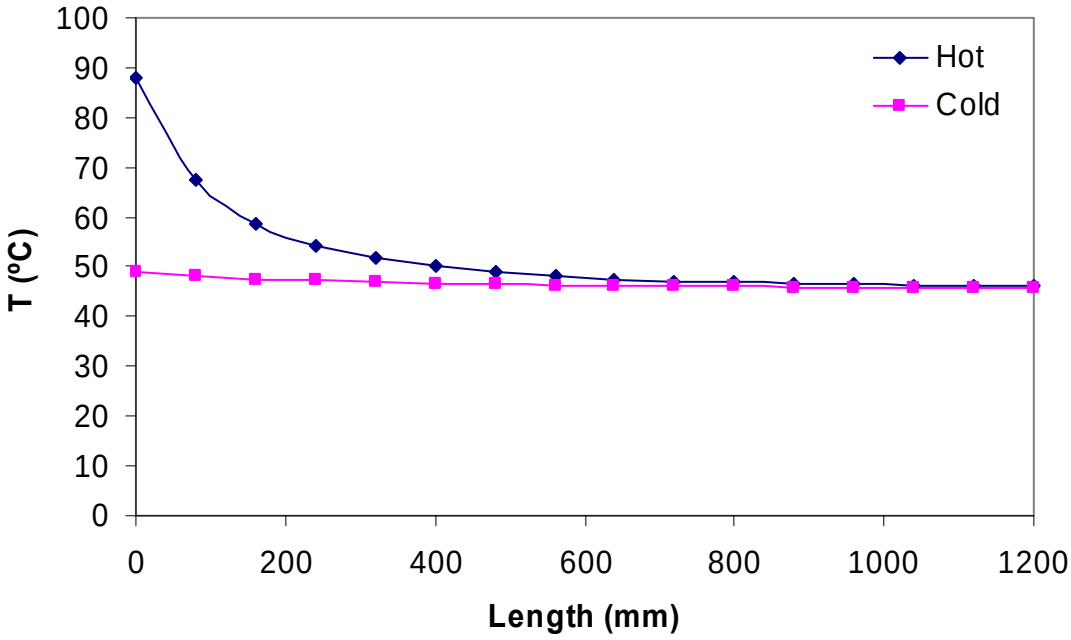

Figure E.16: Temperature Distribution for Test C10

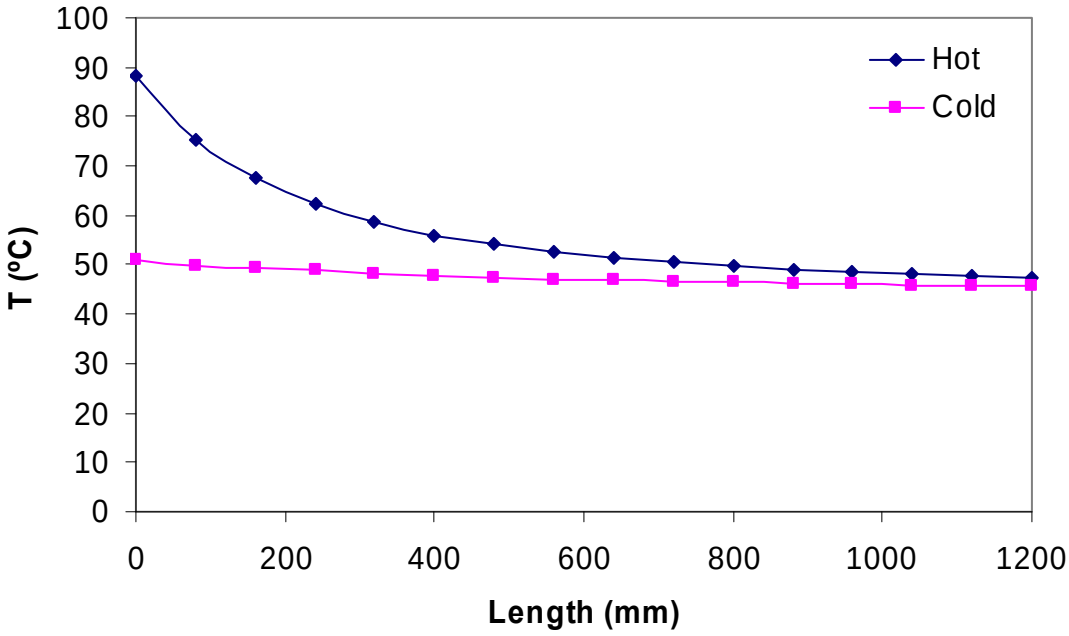

Figure E.17: Temperature Distribution for Test C11

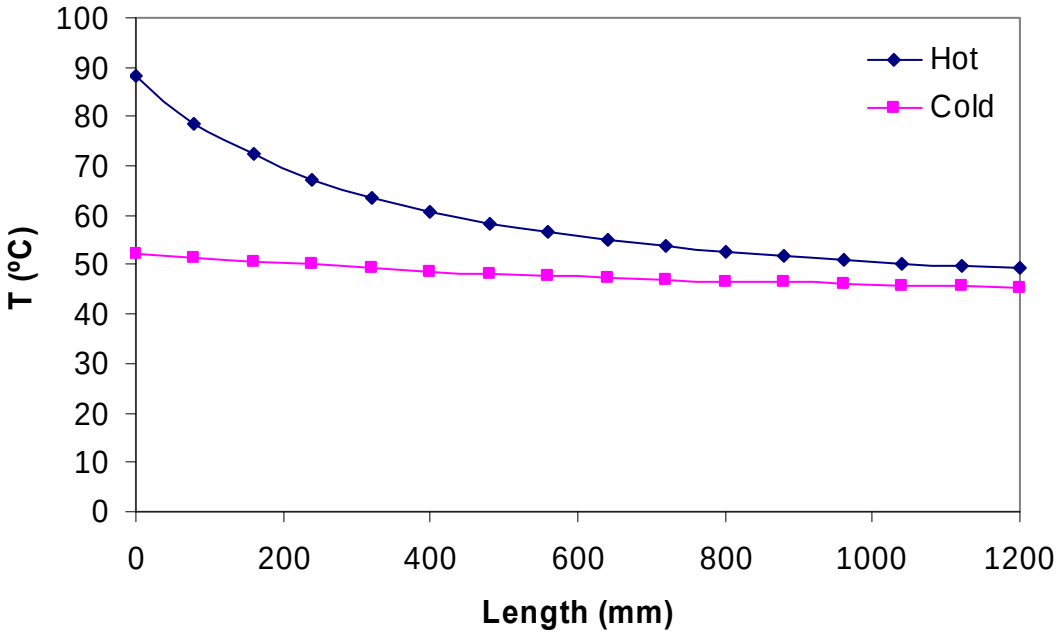

Figure E.18: Temperature Distribution for Test C12

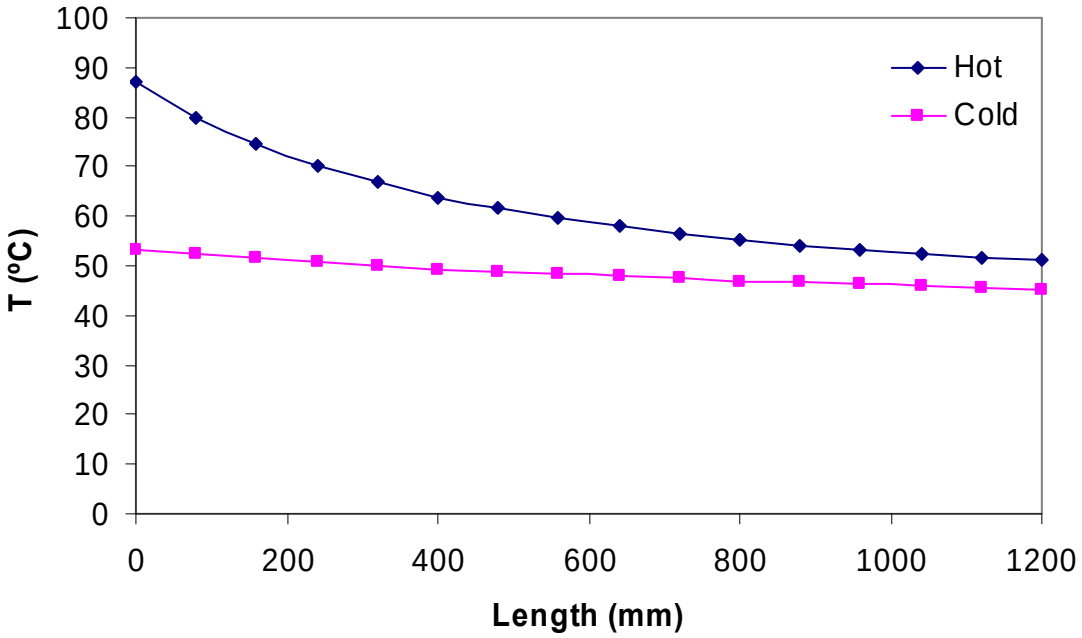

Figure E.19: Temperature Distribution for Test C13

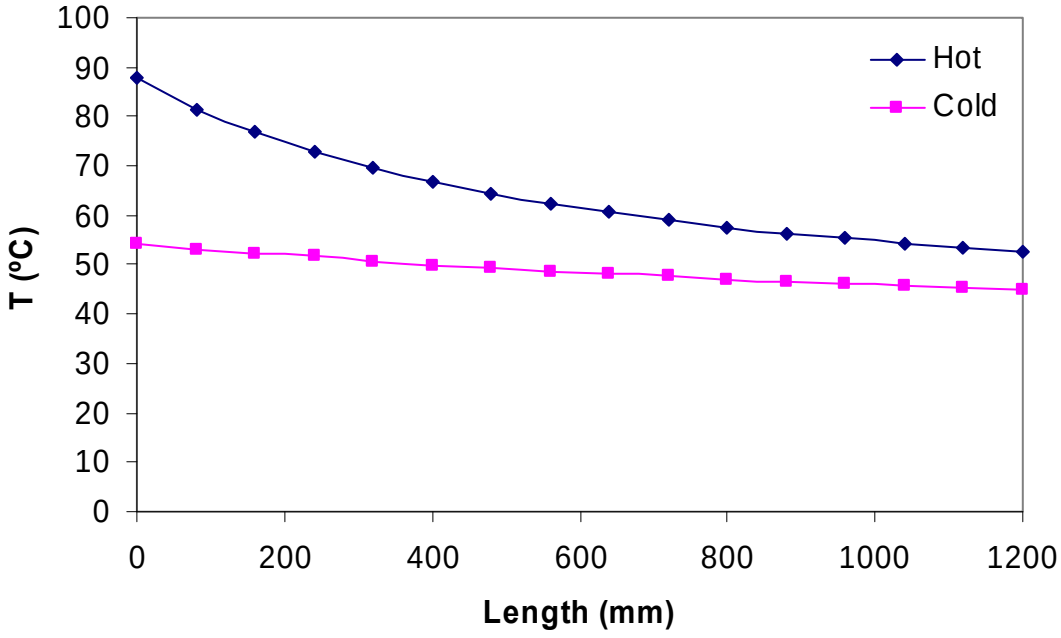

Figure E.20: Temperature Distribution for Test C14